Maintenance of cell wall remodeling and vesicle production are connected in *Mycobacterium tuberculosis*

Vivian Salgueiro[1]*, Jorge Bertol[2]*, Claude Gutierrez[3], Jose L. Serrano-Mestre[1], Noelia Ferrer-Luzon[2], Ainhoa Palacios[4], Laia Pasquina-Lemonche[5], Akbar Espalliat[6], Laura Lerma[1], Brian Weinrick[7], Jose L. Lavin[8], Felix Elortza[4], Mikel Azkalgorta[4], Alicia Prieto[9], Pilar Buendía-Nacarino[10], José L. Luque-García[10], Olivier Neyrolles[3], Felipe Cava[6], Jamie K. Hobbs[5], Joaquín Sanz[2#] and Rafael Prados-Rosales[1#]

[1]Department of Preventive Medicine and Public Health and Microbiology, Universidad Autónoma de Madrid, Madrid, Spain;[2]Institute for Bio-computation and Physics of Complex Systems BIFI, Department of Theoretical Physics, University of Zaragoza, Zaragoza, Spain; [3]Institut de Pharmacologie et de Biologie Structurale, IPBS, Université de Toulouse, CNRS, UPS, Toulouse, France; [4]CIC bioGUNE, , Basque Research and Technology Alliance (BRTA), Bizkaia Science and Technology Park, Derio, Spain; [5]Department of Physics and Astronomy, University of Sheffield, Sheffield, UK; [6]Department of Molecular Biology and Laboratory for Molecular Infection Medicine Sweden, Umeå Centre for Microbial Research, SciLifeLab, Umeå University, Umeå, Sweden; [7]Trudeau Institute, Saranac Lake, NY, USA; [8]Bioinformatics Unit, Neiker-Tecnalia, Derio, Spain; [9]Department of Microbial & Plan Biotechnology, Centro de Investigaciones Biológicas Margarita Salas, Spanish National Research Council (CSIC),Madrid, Spain; [10]Department of Analytical Chemistry, Universidad Complutense de Madrid, Madrid, Spain.

Key words: extracellular vesicles, *Mycobacterium tuberculosis*, vesiculogenesis, peptidoglycan, membrane, permeability.

#To whom correspondence should be addressed:

Dr. Rafael Prados-Rosales– rafael.prados@uam.es

Dr. Joaquín Sanz- jsanz@bifi.es

*Equal contribution

Running title: *Mycobacterium* vesicle biogenesis mechanism.

Abstract

Pathogenic and nonpathogenic mycobacteria secrete extracellular vesicles (EVs) under various conditions. EVs produced by *Mycobacterium tuberculosis* (*Mtb*) have raised significant interest for their potential in cell communication, nutrient acquisition, and immune evasion. However, the relevance of vesicle secretion during tuberculosis infection remains unknown due to the limited understanding of mycobacterial vesicle biogenesis. We have previously shown that a transposon mutant in the LCP-related gene *virR* (*virR*^{mut}) manifested a strong attenuated phenotype during experimental macrophage and murine infections, concomitant to enhanced vesicle release. In this study, we aimed to understand the role of VirR in the vesicle production process in *Mtb*. We employ genetic, transcriptional, proteomics, ultrastructural and biochemical methods to investigate the underlying processes explaining the enhanced vesiculogenesis phenomenon observed in the *virR*^{mut}. Our results establish that VirR is critical to sustain proper cell permeability via regulation of cell envelope remodeling possibly through the interaction with similar cell envelope proteins, which control the link between peptidoglycan and arabinogalactan. These findings advance our understanding of mycobacterial extracellular vesicle biogenesis and suggest that these set of proteins could be attractive targets for therapeutic intervention.

Introduction

Mycobacterium tuberculosis (*Mtb*) is one of the most successful human pathogens with the capacity to persist within the host establishing long-lasting infections. *Mtb* possesses multiple highly evolved mechanisms to manipulate host cellular machinery and evade the host immune system. Similar to other intracellular pathogens, *Mtb* releases proteins and lipids, that interfere with host cellular processes, via canonical or specialized secretion systems (Majlessi et al., 2015). How mycobacteria confined within phagosomes delivers virulence factors to other cellular compartments and/or into the extracellular milieu to affect the physiology of neighboring cells is currently a matter of investigation. Understanding the physiology of this phenomenon during the infection process might be critical to develop alternative therapies against tuberculosis (TB).

Like most forms of life, *Mtb* uses an alternative antigen release process based on extracellular vesicles (EVs) (Prados-Rosales et al., 2011). Mycobacterial EVs (MEVs) are membrane walled spheres of 60-300 nm in diameter, released by live bacteria *in vitro* and *in vivo*. MEVs contain iron scavenging molecules, immunologically active complex lipids and lipoproteins, and classical virulence factors such as the *Mycobacterium ulcerans* toxin mycolactone (Lee et al., 2015; Marsollier et al., 2007; Prados-Rosales et al., 2011, 2014b). Several studies have clearly established a role of MEVs in immunomodulation and shown that MEVs deliver factors that impair macrophage effector functions, inhibit T cell activation, and modify the response of host cells to infection (Athman et al., 2015, 2017; Prados-Rosales et al., 2011, 2014b, 2014a; Rath et al., 2013). MEVs have also shown potential as biomarkers of *Mtb* infection (Schirmer et al., 2022; Ziegenbalg et al., 2013). Although the importance of MEVs has been recognized, hardly anything is known regarding both how such vesicles are exported across the mycobacterial cell wall and the molecular mechanisms underlying vesicle formation in mycobacteria. To date, several modulators of MEVs have been described. Our group identified two conditions leading to stimulation of vesicle production, namely: iron starvation (Prados-Rosales et al., 2014b) and the deletion of *virR* (Rv0431, vesiculogenesis and immune response Regulator) (Rath et al., 2013). In addition, it was shown that the Pst/SenX3-RegX3 signal transduction system regulates MEVs production independent from VirR (White et al., 2018), suggesting an alternative mechanism of vesicle production. We have recently demonstrated that both iron starvation and deletion of VirR in *Mtb*, two hypervesiculating conditions, trigger the induction of the isoniazid-induced gene operon *iniBAC* (Gupta et al., 2023). We determined that both IniA and IniC are dynamin-like proteins (DLP) presumably assisting MEV release through the fusion of the cell membrane (Gupta et al., 2023; Wang et al., 2019). Understanding how defects

126 in VirR lead to hypervesiculation through DLPs is important to provide mechanistic
127 explanation for the vesiculation process in mycobacteria.
128 Several lines of evidence support the notion that VirR might be involved in
129 maintaining cell wall integrity: (i) First, sequence analysis of the VirR protein indicates
130 that it contains a conserved LytR_C domain (**Fig S1**), which is usually found in
131 combination with another domain named LytR-Cps2A-Psr (LCP), and proteins carrying
132 both domains have been associated with the remodeling of the cell wall in Gram-positive
133 bacteria (Hubscher et al., 2008). *Mtb* has six genes encoding for LCP proteins, three with
134 both LCP and LytR_C domains (Rv3267, Rv3484 and Rv0822), two with a solo LytR_C
135 domain (VirR and Rv2700) and one protein with a solo LCP domain (Rv3840) (**Fig S1**).
136 The LCP family includes enzymes that transfer glycopolymers from membrane-linked
137 precursors to peptidoglycan (PG) or cell envelope proteins and are central to cell
138 envelope integrity (Kawai et al., 2011). In mycobacteria its was demonstrated that some
139 members of the (LCP) family of proteins are responsible for the linkage between
140 arabinogalactan (AG) and PG (Grzegorzewicz et al., 2016; Harrison et al., 2016).
141 Rv3267, Rv3484 and Rv0822 appear to have overlapping functions in cell wall assembly,
142 Rv3267 being the primary ligase (Grzegorzewicz et al., 2016). Interestingly, while
143 knocking down the gene encoding for the main AG-PG ligase (cg0847, *lcpA*) in
144 *Corynebacterium glutamicum* leads to the release of outer membrane material to the
145 extracellular medium (Baumgart et al., 2016), this phenotype is not observed in any
146 knockout strain in the *Mtb* orthologs (Grzegorzewicz et al., 2016), probably reflecting the
147 ability of the mutants to negatively regulate the biosynthesis of cell wall constituents in
148 response to a decrease in ligase activity; (ii) Second, we and others have determined
149 the increased susceptibility of the transposon *virR* mutant (*virR*^{mut}) with respect to the
150 WT (Ballister et al., 2019; Rath et al., 2013), and the mutant in the *virR* ortholog, Rv2700
151 (cell envelope integrity, *cei*) to cell wall targeting drugs such as meropenem (Ballister et
152 al., 2019). Based on these results, we hypothesize that LytR_C solo domain proteins
153 including VirR and Cei Rv2700 have critical roles in the maintenance of cell wall
154 homeostasis and their absence provokes cell wall alterations leading to enhanced
155 vesiculation.
156 In this work we show that the absence of VirR leads to ultrastructural changes in
157 the cell envelope as observed by cryo-electron microscopy (cryo-EM). These changes
158 are compatible with enhanced permeability and an enlargement of the PG layer, as
159 measured by high resolution atomic force microscopy (AFM). We demonstrate that VirR
160 interacts with canonical LCP proteins and propose a model for such interaction. These
161 results indicate that VirR is a central scaffold at the cell envelope remodeling process

assisting the PG-AG linking process and that this function is important for vesicle production in *Mtb*.

Results

High EV production linked to the lack of VirR is associated with an altered cell envelope in *Mtb* in the absence of cell lysis. While Gram-negative bacteria can release outer membrane vesicles directly into the extracellular environment from their outermost compartment, Gram-positive bacteria and mycobacteria have thick cell envelopes surrounding the cytoplasmic membrane that acts as a permeability barrier. The mycobacterial cell envelope is composed of PG covalently linked to AG, which in turn is decorated with exceptionally long-chain mycolic acids (MA). These MA, together with intercalating glycolipids, form the unique mycobacterial outer membrane (OM) (Kalscheuer et al., 2019). Previous analysis of mycobacterial vesicle associated lipids showed predominantly polar lipids, consistent with the cytoplasmic membrane being the likely origin of the vesicles (Prados-Rosales et al., 2011). This is also true in EV produced by Fe-limited *Mtb* whose lipid content consists mainly of polar lipids and the lipidic siderophore, mycobactin (Prados-Rosales et al., 2014b). Given that these vesicles must traffic from their point of origin in the plasma membrane through the cell envelope, we hypothesized that local remodeling of the cell envelope is necessary for EV release, and that this process may be exacerbated in a *virR* mutant (*virR*^{mut}). To test this, we examined the cell envelope structure of *virR*^{mut} grown in minimal medium (MM), as well as wild type (WT) and *virR*^{mut} complemented (*virR*^{mut}-C) strains (Rath et al., 2013) (**Fig 1**). Using cryo-electron microscopy (cryo-EM) on whole cells, which allows the study of mycobacterial cell surface-associated compartments in a close-to-native state (Sani et al., 2010), we could easily discern three layers comprising the mycobacterial cell envelope: i) the outer membrane (OM); ii) an intermediate layer composed of two sublayers (L1 and L2, previously assigned to the mycolate-PG-AG (mAGP) network (Sani et al., 2010)); and iii) the cytoplasmic membrane (CM) (**Fig 1**). We observed a significant increase in the thickness of the overall cell envelope (OM-CM) in the *virR*^{mut} strain compared to the WT. This difference was largely explained by the expansion of the CM-L1 layer, which appeared also more granulated, suggesting cell wall alterations closer to the cell membrane and indicating aberrant production of either AG, PG or both. Complementation of *virR* restored normal cell envelope structure (**Fig 1A-C**).

In Gram-negative bacteria increased vesiculation has been observed in conditions associated with either loss or maintenance of periplasm integrity (McMillan

199 and Kuehn, 2021). Moreover, a novel mechanism of vesicle production common to both
200 Gram-negative and Gram-positive bacteria has recently been described, in which a cell
201 explosion phenomenon driven by bacteriophages leads to the formation of EVs in culture
202 when bacteria are under genotoxic stress (Nagakubo et al., 2021). Consequently, we
203 tested whether the enhanced vesiculation described in *virR*^{mut} (Rath et al., 2013) could
204 be linked to cell lysis events. To do this, we analyzed the presence of cytoplasmic IdeR,
205 a transcription factor which is not present in EVs and is not detected in secreted proteins
206 preparations, in culture supernatants of *Mtb* strains, assuming that its detection could be
207 linked to a loss of envelope integrity (Gupta et al., 2023). We first confirmed that the
208 *virR*^{mut} strain manifested an enhanced vesiculation by measuring EVs using nanoparticle
209 tracking analysis (NTA) (**Fig S2A**). We did not detect differences in size distribution of
210 isolated EVs between strains. The same supernatants and cell lysates were used to
211 detect the presence of IdeR by immunoblot using a specific polyclonal antibody (Pandey
212 and Rodriguez, 2014). As a control for normal release of an extracellular protein, we
213 used a monoclonal antibody against Ag85b (Prados-Rosales et al., 2017). We could not
214 detect IdeR in the supernatant of WT and *virR*^{mut} strain, but a faint band corresponding
215 to IdeR could be observed in the SN of the *virR* complemented strain (*virR*^{mut}-Comp).
216 These results suggest that the absence of *virR* does not lead to cell lysis but its
217 overexpression may compromise cell envelope integrity (**Fig S2B**). We validated this
218 approach by serially diluting WT, *virR*^{mut} and *virR*^{mut}-Comp strains on 7H10 solid media.
219 As shown in **Fig S2D**, we did not observe differences in the number of cells across the
220 diluted spots between strains. Taken together, the observed changes in the cell envelope
221 of high EV producing bacteria suggest that cell envelope alterations in response to lack
222 of VirR and increased membrane vesicle biogenesis may be connected in *Mtb*.
223
224 **The absence of LytR_C solo domain proteins in *Mtb* leads to enhanced cell**
225 **envelope permeability concomitant to hypervesiculation.** The collective cryoEM
226 observations that indicated an enlargement of the compartment next to the cell
227 membrane may be linked to a more permeable cell envelope. Supporting this notion is
228 the recent finding that *virR*^{mut} or the mutant in the *virR* ortholog *cei* (Rv2700) manifest
229 an enhanced uptake of ethidium bromide (EtBr) relative to WT strain (Ballister et al.,
230 2019). We could reproduce these results and add that *virR*^{mut}-Comp strain restores the
231 permeability levels of the WT strain (**Fig 2A**). This enhanced permeability was
232 concomitant to an increased sensitivity to different antitubercular drugs, including
233 meropenem and vancomycin (Ballister et al., 2019). In agreement with these results, we
234 could measure a significantly enhanced sensitivity of *virR*^{mut} to the PG-targeting drug
235 vancomycin relative to WT and *virR*^{mut}-Comp strains (**Fig 2B**). Interestingly, the

236 magnitude of the sensitivity to cell wall targeting drugs was either moderate (ethambutol)
237 or absent (isoniazid) in *virR*^{mut} (Ballister et al., 2019).
238 Furthermore, we observed enhanced incorporation of fluorescent D-amino acids
239 (FDAAs) in *virR*^{mut} relative to the WT and complemented strains (**Fig 2C**). These probes
240 can freely enter cells and may be incorporated into PG by at least three different
241 mechanisms, depending on the species: through the cytoplasmic steps of PG
242 biosynthesis and via two distinct transpeptidation reactions taking place in the periplasm
243 (Kuru et al., 2019). Consequently, the differential labeling observed in *virR*^{mut} relative to
244 WT strain may be a consequence of altered PG turnover in the mutant.
245 We then tested whether the enhanced permeability and vesiculation of *virR*^{mut} are also
246 connected in an *Mtb* mutant lacking *cei* (Ballister et al., 2019). To do this, we generated
247 *cei* conditional mutants using the CRISPR interference (CRISPRi) technology (Rock et
248 al., 2017). Further, we also generated *virR* CRISPRi conditional mutants to properly
249 compare both strains (**Fig 2D**). When these strains were cultured in the presence of
250 anhydrotetracycline (ATc) to induce the transcriptional silencing of target genes, we
251 could measure enhanced vesiculation by analyzing vesicle concentration in the
252 supernatant by NTA (**Fig 2E**), relative to strains cultured in the absence of ATc. Overall,
253 these results validate the enhanced permeability phenotype of *Mtb* mutants in the
254 LytR_C solo domain proteins VirR and Cei and establish that this subfamily of proteins
255 participates in the regulation of vesicle production in *Mtb*. Moreover, the higher
256 susceptibility to PG-cross-linking inhibitors in both mutants and the enhanced
257 incorporation of FDAAs in the *virR* mutant strain suggests defects in PG remodeling.
258
259 **Transcriptional profiling of *virR*^{mut} showcases systemic alterations in cell wall**
260 **architecture and metabolism.** To identify *virR*-dependent mediators of vesicle
261 production, we carried out a transcriptional profiling of *virR*^{mut} and compared it to those
262 from a WT and *virR*^{mut}-Comp strains. Previous efforts to define the transcriptional profile
263 of *virR*^{mut} showed no significant differences compared to WT (Rath et al., 2013).
264 However, those experiments were carried out with bacteria grown in rich 7H9 medium,
265 while here we use a defined high-Fe minimal medium (MM), which is typically used for
266 vesiculation experiments (Prados-Rosales et al., 2011). We extracted RNA from four
267 independent cultures (average optical densities (OD) of 0.40, 0.38 and 0.42 for WT,
268 *virR*^{mut}, and *virR*^{mut} -Comp, respectively) one day before vesicle isolation, and conducted
269 RNA-seq (**Fig 3A**). Principal component analysis (PCA) was then performed on the
270 transcriptomic data, after filtering out lowly expressed genes, as well as genes containing
271 outlier observations (N=3985 genes tested, see Methods), and revealed significant
272 differences between strains. The first principal component, explaining 49% of the

273 variance, separated *virR*^{mut} strain samples from strains bearing functional copies of *virR*
274 (**Fig 3B**, WT and *virR*^{mut}-Comp vs *virR*^{mut}, one-tailed Mann-Whitney test p=2.02E-2).
275 Furthermore, the second principal component (28.3% variance) captured *virR*-
276 independent effects of mutagenesis on transcriptional profiles, as it separated WT
277 samples from *virR*^{mut}-Comp and *virR*^{mut} (one-tailed Mann-Whitney test p=2.02E-2).
278 After PCA, we conducted differential expression analysis between strains to find 1808,
279 and 2230 genes differentially expressed in *virR*^{mut} compared to either WT, or *virR*^{mut}-
280 Comp strains, respectively (**Supplementary file S1**, **Fig 3C**, Benjamini-Hochberg
281 FDR<0.05), representing 45.4% and 56.0% of all genes tested. Although transcriptional
282 profiles of the WT and *virR*^{mut}-Comp strains are also significantly diverse, with up to 2184
283 differentially expressed genes between them, the differences in expression between
284 *virR*^{mut} when compared to either WT or *virR*^{mut} -Comp are significantly correlated (r=0.63,
285 p<2.2e-16), and the sets of both upregulated and downregulated genes in *virR*^{mut} vs any
286 of the other strains are mutually, directionally enriched (**Fig 3D**). Finally, we defined a
287 set of N=399 genes that are simultaneously upregulated in *virR*^{mut} with respect to any of
288 the two strains containing functional copies of *virR* (logFC>0 and FDR<0.05 for both
289 *virR*^{mut} vs WT and *virR*^{mut} vs *virR*^{mut}-Comp), as well as a set of N=502 genes
290 downregulated in *virR*^{mut} vs both *virR*-containing strains. This way, the differential
291 expression signature found for these genes in the *virR*^{mut} strain is most likely VirR-
292 dependent and not-induced by non-specific consequences of the mutagenesis
293 procedures.
294 Next, we looked for gene ontologies (GO) enriched among these *virR*-dependent genes,
295 stratified by the direction of the effects (399 up-regulated, and 502 down-regulated in
296 *virR*^{mut} relative to WT and *virR*^{mut}-Comp alike). A total of 51 GO terms related with
297 biological processes and cell compartment appeared significantly enriched among genes
298 upregulated in the *virR*^{mut} strain (FDR=10%), while 85 terms were enriched among
299 downregulated genes (FDR=10%, see Methods, and **supplementary file S2**). When
300 focusing on the most prominent of these enrichments (OR>2), the analyses highlighted
301 several groups of biological processes and cell compartment ontologies that appeared
302 altered in *virR*^{mut} with respect to both WT and *virR*^{mut}-Comp strains (**Fig 3E**).
303 First, among genes that were expressed at lower levels in *virR*^{mut}, we found terms related
304 to several stresses associated with the intra-phagosomal environment (Schnappinger et
305 al., 2003), such as response to hypoxia (FDR=1.7E-5), heat (FDR = 2.2E-2) or response
306 to metal ions (FDR=3.4E-2), suggesting that responses to host-induced stress are
307 compromised in the mutant, as it is also suggested by the weaker, albeit significant
308 enrichments of responses to host immune response (OR=1.88, FDR=7.47e-02, not
309 highlighted in **Fig 3E**). Furthermore, the mutant strain showed a reduction in transcripts

310 related with secretion (FDR=7.6e-03), and, specifically, protein secretion by the type VII
311 secretion system (FDR=5.2 e-03). Contributing to this enrichment, we found that the key
312 antigen ESAT-6 was significantly down-regulated in *virR*^{mut} with respect to both WT
313 (log2FC=-0.17, FDR=4.1E-3) and *virR*^{mut}-Comp strains (log2FC=-0.19, FDR=2.6E-3),
314 while *cfp10* (Rv3874), was similarly less expressed in *virR*^{mut} than in WT (log2FC=-0.24,
315 FDR=2.6E-3).
316 Second, we found enriched terms related with lipid metabolism and transport both among
317 the sets of genes up and downregulated in the *virR*^{mut} strain. On the one hand, genes
318 downregulated in *virR*^{mut} appeared enriched in fatty acid biosynthetic processes
319 (FDR=6.7E-2), suggesting that the regulation of both anabolic and catabolic pathways
320 of lipids, key for bacterial survival and pathogenesis upon infection (Ghazaei, 2018), are,
321 at least in part, VirR-dependent. Furthermore, the mutant strain also shows a significant
322 induction of a number of GO terms related with cell wall composition (e.g. cell wall
323 organization: FDR=3.9e-2), including terms associated with the biosynthesis key
324 components of the mycobacterial cell wall such as PDIMs (DIM/DIP cell wall layer
325 assembly enrichment FDR=9.5e-03) and importantly peptidoglycan (peptidoglycan-
326 based cell wall biogenesis FDR=2.2e-2) (**Fig 3F**).
327 Third, we found a series of enrichments related with global regulation of gene expression
328 (positive: FDR=4.4e-2, negative: FDR=5.4e-2), and RNA biosynthesis (positive:
329 FDR=5.4e-2, negative: FDR=5.8e-2), among genes downregulated in *virR*^{mut}, suggesting
330 a global alteration of the transcriptional landscape in the mutant.
331 Fourth, we found that metabolic reprogramming in the *virR*^{mut} strain is not restricted to
332 lipids but also involves amino acids (cellular amino acid metabolic processes FDR=2.1e-
333 3), and carbohydrates (cellular carbohydrate biosynthetic process FDR=6.8e-3),
334 enriched among genes upregulated in the mutant. Similarly, energy production also
335 appears altered in *virR*^{mut}, with related GO terms enriched among downregulated genes,
336 such as electron transfer activity, (FDR=4.2e-2), as well as terms enriched among
337 upregulated genes in the mutant such as NADH dehydrogenase activity, (FDR=3.3e-3).
338 All together, these results combined with the differences concerning lipid metabolism
339 discussed above, suggest a global remodeling of metabolic networks in *virR*^{mut}.
340
341 ***virR*-dependent genes intersect the regulons of key transcriptional regulators of**
342 **responses to stress, dormancy, and cell wall remodeling.** To shed light on the
343 specific transcriptional circuits whose disruption in the *virR*^{mut} strain may lead to the
344 differential gene expression patterns described, we resorted to the regulon annotations
345 previously reported (Minch et al., 2015). In this work, authors collected ChIP-seq data on
346 binding events between a panel of transcription factors (TFs) and DNA to annotate

347 interactions between 143 regulators and the promoters of 7248 target genes (peaks
348 between -150 and +70 nucleotides from transcription staring sites). Capitalizing on these
349 data, we interrogated whether the sets of genes up- (N=399) and downregulated in the
350 *virR*^{mut} strain (N=502) were significantly enriched among each of the regulons reported
351 by Minch et al. A total number of 10 regulons appeared enriched among either down (9)
352 or upregulated genes (1) in *virR*^{mut} (**Supplementary file S3** and **Fig 4A**, highlighted TFs
353 at OR>2 FDR<0.1). Furthermore, the expression of 7 out of 10 of the TFs controlling
354 these regulons was itself found to be *virR*-dependent in our transcriptional data (**Fig 4B**).
355 Genes more highly expressed in the *virR*^{mut} strain appeared significantly enriched among
356 Rv0339 targets (OR=9.1, FDR=7.5E-2, **Fig 4A**), named IniR because of its role as key
357 regulator of the isoniazid-induced operon *iniBAC*, a key element of the response to cell
358 wall biosynthesis inhibition induced by isoniazid (Boot et al., 2017) and linked to vesicle
359 biogenesis in *Mtb* (Gupta et al., 2023). Several additional transcription factors known to
360 regulate cell wall biosynthesis and homeostasis were also enriched among genes
361 downregulated in the *virR*^{mut} strain. These include SigF (OR=5.8, FDR=8.1E-2), a sigma
362 factor controlling cell envelope organization (Williams et al., 2007), *mtrA* (OR=2.2,
363 FDR=6.0E-2), a TF controlling peptidoglycan cleavage and alterations in the context of
364 regulation of cell growth and division, whose disruption has recently been shown to lead
365 to increased permeability (Peterson et al., 2023); as well as Rv0472c (OR=11.7,
366 FDR=3.5E-2), a transcription factor involved in the regulation of mycolate remodeling
367 pathways (Peterson et al., 2019), a process used by the pathogen upon phagocytosis to
368 evade macrophage-induced stress and enter dormancy. Interestingly, two genes under
369 the control of Rv0472c, that are key to enable this process, are the mycolate desaturases
370 *desA1* and *desA2* (Peterson et al., 2019), which appear downregulated in the *virR*^{mut}
371 strain with respect to WT (logFC=-0.4, -0.1; FDR=2.3E-11, 3.2E-2, for *desA1*, and
372 *desA2*, respectively), as well as with respect to *virR*^{mut}-Comp (logFC=-0.4, -0.4;
373 FDR=7.2E-12, 5.3E-21). Furthermore, Rv0472c has also been linked with the regulation
374 of key proteins in the response to several sources of stress in *Mtb*, such as the putative
375 nitroreductase Rv3131 (response to oxidative/nitrosative stress), as well as the
376 triacylglycerol synthase *tgs1*, responsible for the synthesis and accumulation of
377 triacylglycerol, a major energy source for the bacterium during dormancy (Chauhan and
378 Tyagi, 2009), both of which are strongly downregulated in the *virR*^{mut} strain vs both WT:
379 (logFC=-1.2, -1.7; FDR=3.1E-19, 3.2E-14) and *virR*^{mut}-Comp (logFC=-0.4, -1.9;
380 FDR=3.9E-5, 1.4E-17).
381 The adjacent genes Rv3131 and *tgs1* (Rv3030c) appear under the control of other key
382 regulators of the response to intracellular stress in *Mtb* and the transition to dormancy,
383 whose regulons appear as well enriched among genes downregulated in *virR*^{mut} (**Fig**

384 **4C**). These include *devR* (OR=2.7, FDR=1.9E-5), the canonical regulator of the response
385 to hypoxia and transition to dormancy in *Mtb* (Park et al., 2003), as well as Rv1985c
386 (OR=4.1, FDR=4.5E-11), a key regulator of the homeostasis of the threonine
387 biosynthesis pathway, a metabolic route needed by the bacterium for persistence *in vivo*
388 (Hasenoehrl et al., 2019). Three of the four remaining TFs whose regulons we found
389 enriched among *virR*^{mut} downregulated genes have been similarly linked to the response
390 to assorted sources of stress that are cardinal features of the phagosome environment,
391 such as oxidative stress, response to toxic metals, and low pH (Schnappinger et al.,
392 2003). These include the regulator *lsr2* (OR=2.3, FDR=5.1E-4), a global histone-like
393 protein responsible from protecting the DNA physically from oxidative stress (Bartek et
394 al., 2014), the zinc-uptake regulator Zur (*furB*) (Maciąg et al., 2007) (OR=8.8, FDR=4.5E-
395 2), and *tcrX* (OR=2.6, FDR=5.0E-2), part of the recently characterized acid-sensing two-
396 component system tcrXY (Stupar et al., 2024). Notably, we observed that removing
397 catalase from culture medium prior to submitting *virR*^{mut} to a source of oxidative stress
398 like H202 for 8 h, significantly affected its growth relative to WT and *virR*^{mut}-C strains (**Fig**
399 **S3**). This result validates the transcriptomics data reflecting a defect in regulating
400 oxidative stress in *virR*^{mut} and encourage to investigate its connection with vesicle
401 production.
402
403 **Cell envelope permeability is a major driver of MEV release**. If enhanced cell
404 permeability is a global consequence of *virR* disruption that leads to enhanced
405 vesiculation, we hypothesized that other conditions either inducing or decreasing cell
406 envelope permeability could lead to alterations in vesicle production in *Mtb*. To test this,
407 we treated *Mtb* with sublethal concentrations of thioridazine (TRZ), a known enhancer of
408 cell permeability (De Keijzer et al., 2016); and, alternatively, we cultured the bacillus with
409 cholesterol as a sole carbon source, a condition which reduces mycobacterial cell
410 permeability (Brzostek et al., 2009) (**Fig 5A**). The enrichment of the DevR regulon among
411 the genes that are downregulated in *virR*^{mut} is also suggestive of the existence of a
412 convergent regulatory route controlling both cell permeability and vesiculation under
413 control of this transcription factor, whose activation has been described as a key part of
414 the pathogen's transcriptomic response to cholesterol (Soto-Ramirez et al., 2017),
415 concomitant to a reduction in cellular permeability (Brzostek et al., 2009). Importantly,
416 neither cholesterol nor TRZ altered bacterial viability as measured by the absence of the
417 release of the transcription factor IdeR, as an indication of cell lysis or by spotting serially
418 diluted cultures on solid medium from the corresponding conditions (**Fig S2C,D**). We
419 then measured vesicle levels in culture supernatants and found that *Mtb* significantly
420 releases more EVs upon treatment with TRZ, and significantly reduces vesicle release

421 in the presence of cholesterol as a sole carbon source (**Fig 5B**), as measured by dot blot
422 after normalization to colony forming units (CFUs). These results strongly suggest that
423 cell envelope permeability determines the magnitude of the vesiculation phenomenon in
424 *Mtb*. We next investigated whether common transcriptional features underpin the
425 regulation of cell envelope permeability in the tested conditions. To do that, we compared
426 the transcriptional response of *virR*^{mut} with that of available datasets including *Mtb*
427 cultured in the presence of 0.01% of cholesterol as a sole carbon source (Pawełczyk et
428 al., 2021), and *Mtb* treated with 6 µg ml-1 of TRZ (Dutta et al., 2010). Experimentally, we
429 retrieved the set of genes up and downregulated in *Mtb* grown in cholesterol vs glucose-
430 rich culture media (Brzostek et al., 2009), and interrogated whether those genes were
431 enriched among the sets of differentially expressed genes in *virR*^{mut} vs WT, and *virR*^{mut}
432 vs *virR*^{mut}-Comp reported in this study (**Fig 5C**). Interestingly, we found that those genes
433 whose expression changed in the same direction in conditions associated with low, or
434 high permeability, in both studies were mutually enriched, while the cross-comparisons
435 between sets with opposite responses to low-permeability-associated treatments in both
436 studies led to significant depletion statistics. These results validate the initial hypothesis
437 according to which changes in permeability induced by these two treatments are linked
438 to the activation of a common transcriptional program. The inspection of genes that are
439 simultaneously upregulated in treatments associated with low permeability in both
440 studies identified DevR as a putative regulator associated with the orchestration of this
441 transcriptional footprint of low cell permeability. The two-component system DevS-DevR
442 (also known as DosS-DosR) has a well-known role as a global regulator of the transition
443 to dormancy, and its regulon is consistently upregulated in non-permeable dormant
444 bacteria (Honaker et al., 2009).
445 Interestingly, authors found that low-permeability bacteria cultured in a cholesterol
446 medium, albeit featuring a regular growing phenotype, activated the DosR regulon,
447 suggesting that cell wall remodeling leading to a decrease in permeability linked with the
448 induction of DosR can be triggered independently to the transcriptional regulatory
449 programs leading to growth arrest and dormancy in *Mtb* (Pawełczyk et al., 2021).
450 Importantly, the integration of the genes that are downregulated in *virR*^{mut} validates this
451 hypothesis (**Fig 5D and FigS4**), since not only the intersection between the DevR
452 regulon and the set of genes downregulated in *virR*^{mut} are significantly larger than
453 expected by chance (see **Fig 4A**, OR=2.67, p=2.7E-7), but also the intersection between
454 DevR regulon and the genes that are activated by cholesterol in Brzostek et al. data
455 (OR=1.89, p=3.5e-5). 30 out of the 173 genes annotated in the DosR regulon described
456 in (Minch et al., 2015) are simultaneously upregulated in conditions linked to low
457 permeability in both studies.

458 A similar analytic approach for the comparison of the response of *virR*^{mut} and the
459 response to the drug TRZ, a treatment well-known for inducing an increase in
460 permeability in *Mtb*-treated cells (Dutta et al., 2010) (GSE16626), led to conceptually
461 similar results, with genes simultaneously downregulated in both TRZ and *virR*^{mut}
462 (OR=1.96, p=9.1E-4) being enriched. Interestingly, among the 22 genes showing the
463 largest, and most significant repression effects by both treatments (log2FC>0.25 &
464 FDR<0.05 simultaneously, for TRZ effects, *virR*^{mut} vs WT), we found 4 genes whose
465 functions are related with metal nutrients uptake and homeostasis, such as genes
466 encoding the bacterioferritin BrfB, the metal exporter CtpJ, the cupper regulator CsoR
467 and Moew, involved in Molibdenum-cofactors biosynthesis (**Fig 5E**). Taken together,
468 these analyses highlight the transcriptional parallels between *virR*^{mut} and both TRZ and
469 cholesterol conditions, which strongly suggests the existence of a common
470 transcriptional signature associated with the control of cell permeability.
471
472 **Modulation of EV levels and permeability in *virR*^{mut} by cholesterol and TRZ**. We
473 next wondered about the effect of culturing *virR*^{mut} on both cholesterol or TRZ could have
474 on cell growth, permeability and EV production. In the case of cholesterol, it has also
475 been shown to affect other aspects of physiology (redox, respiration, ATP), which can
476 directly affect permeability (Lu et al., 2017). We monitored *virR*^{mut} growth in MM
477 supplemented with either glycerol, cholesterol as a sole carbon source, or TRZ at 3 ug
478 ml^{-1} for 20 days. While cholesterol significantly enhanced the growth *virR*^{mut} after 5 days
479 relative to glycerol medium, supplementation of glycerol medium with TRZ restricted
480 growth during the whole time-course (**Fig S5A**). The study of cell permeability in the
481 same conditions indicated that the enhanced cell permeability observed in glycerol MM
482 was reduced when *virR*^{mut} when cultured with cholesterol as sole carbon source.
483 Conversely, the presence of TRZ increased cell permeability relative to the medium
484 containing solely glycerol (**Fig S5C**). As we have previously observed for the WT strain,
485 either condition (Chol or TRZ) also modified vesiculation levels in the mutant accordingly
486 (**Fig S5B**). These results strongly indicates that other aspects of mycobacterial
487 physiology besides permeability are also affected in the absence of VirR and may
488 contribute to the observed enhanced vesiculation.
489
490 ***virR* regulates the protein content of EVs in *Mtb***. To capture the impact of
491 transcriptional adaptation to the proteome, and the degree of divergence between
492 transcriptional shifts and proteins changes observed in the absence of *virR*, we next
493 performed label-free peptide mass spectrometry (LF-MS) of whole cell lysates (WCLs)
494 of *virR*^{mut}, WT, and *virR*^{mut}-Comp strains. Additionally, we isolated EVs from axenic

495 cultures and obtained their proteomic composition to examine for potential VirR-
496 dependent differences in protein cargo that may alter the functionality of EVs (**Fig 6A**).
497 As a result, we obtained proteomic profiles across strains and cell compartments for a
498 total of N=935 proteins. Upon PCA analysis of the proteomic data (**Fig 6B**), we found
499 that the first principal component (PC1), explaining 36.9% of total variance, separated
500 samples from WCLs and EVs in all strains (PC1 differs across cell compartments: one-
501 tailed Mann Whitney test p=2.1e-05), while the second PC (PC2) (13.6% of total variance
502 explained) captured strain effects on the proteomic footprint only among EVs (one tailed
503 Mann Whitney t test for PC2 differences between *virR*^{mut} EVs and those from either WT
504 or *virR*^{mut} -Comp strains (one-tailed Mann Whitney p=1.2 e-02). These results suggest
505 that differences in protein abundances between EVs and WCLs are larger than
506 differences found between strains, and that, concerning the differences across strains,
507 these are more important among EVs. To verify this, we conducted differential protein
508 expression analyses to find barely 27 proteins differentially expressed between *virR*^{mut}
509 and any of the two *virR*-expressing strains, which represents 2.9% of the total of proteins
510 under analyses (**supplementary file S4**). Despite the scarcity of significant differences
511 in expression across strains in WCLs, some of the features most differentially expressed
512 in *virR*^{mut} are, besides VirR itself (**Fig 6C**), proteins involved in key processes for bacterial
513 survival and virulence, including key metabolic enzymes such as the Acetyl-coenzyme
514 A synthetase Acs (logFC = -3.92 (FDR=4.5e-3) and -2.96 (FDR=5.2E-2) for the
515 differences between *virR*^{mut} and WT, and between *virR*^{mut} and *virR*^{mut}-Comp,
516 respectively), as well as FprA, (logFC= -3.12, FDR=4.5e-3 e-02 for *virR*^{mut}-WT and
517 logFC= -2.16, FDR=5.9 e-02 for *virR*^{mut}- *virR*^{mut}-Comp), involved in the reduction of
518 NADP+ into NADPH, both downregulated in *virR*^{mut}.
519 Conversely to the WCL dataset, we did find more frequent differences in protein
520 expression across strains in EVs, with as many as 361, and 382 proteins differentially
521 expressed in *virR*^{mut} EVs when compared to those from WT and *virR*^{mut}-Comp strains,
522 respectively (**supplementary file S4**, **Fig 6D**). This represents 38.6 and 40.9% of all
523 proteins tested, respectively. Similarly to what was observed at the level of RNA
524 expression, differences in expression for the contrasts (*virR*^{mut}-WT) and (*virR*^{mut}- *virR*^{mut}-
525 Comp) were directionally enriched (**Fig 6E**), thus motivating the definition of two sets of
526 proteins that 1) were observed at higher levels in the EVs isolated from *virR*^{mut} than in
527 those from both WT and *virR*^{mut} -Comp strains (N=117 *virR*^{mut} -upregulated proteins); or
528 2) were observed at lower levels in the EVs from *virR*^{mut} than in those from any of the
529 other two strains (N=108 *virR*^{mut}-downregulated proteins). Interestingly, as many as 21
530 out of the 117 proteins that appeared enriched in *VirR*^{mut} EVs were also upregulated in
531 *virR*^{mut} at the transcriptional level (One-sided Fisher exact test of enrichment OR=2.02,

532 p=7.0e-3) suggesting that at least a part of these differences in EVs' protein cargo are a
533 consequence of differences in gene expression already observed at a transcriptional
534 level. Notwithstanding that, proteins appearing at lower concentrations in *virR*^{mut} EVs
535 were not enriched among genes bearing significant transcriptional effects in the mutant.
536 Regarding downregulated EV proteins in *virR*^{mut} we observed robust enrichments in GO
537 terms related with protein biosynthesis, including translation (FDR=9.8 e-22), ribosome
538 (FDR=5.3 e-29), and ribosome biogenesis (FDR=4.1 e-27, **Fig 6F** and **supplementary**
539 **file S5**). Consistent with these results, 44 ribosomal proteins (out of 49 detected) were
540 found to be significantly less expressed in the *virR*^{mut} strain relative to either WT or
541 *virR*^{mut}-Comp strains (FDR<0.05 for at least one comparison), while no ribosomal protein
542 appeared significantly upregulated in *virR*^{mut}. Furthermore, 30 of these proteins were
543 simultaneously downregulated in *virR*^{mut} when compared to both VirR-containing strains
544 (**Fig S6**) implying a stark ribosomal depletion in the EVs in the absence of VirR.
545 Furthermore, we found that the two bacterioferritin proteins BfrA and BfrB were
546 simultaneously less abundant in *virR*^{mut} than in both WT and *virR*^{mut}-Comp strains
547 (logFC<-1.5 and FDR<7.3E-4, for differences *virR*^{mut} vs WT and *virR*^{mut} vs *virR*^{mut}-Comp
548 in both genes, **Fig 6G**, and **supplementary file S4**), together contributing to the
549 enrichment of the GO term ferroxidase activity (FDR=6.4 e-02, **Fig 6F**). This result is
550 suggestive of a possible defect of *virR*^{mut} EVs in iron sequestration (Mohammadzadeh et
551 al., 2021; Prados-Rosales et al., 2014b). We also found a series of metabolic pathways
552 enriched among proteins upregulated in the EVs of the *virR*^{mut} strain, including enzymes
553 involved in metabolism of nucleotides (e.g. purine nucleotide biosynthetic process
554 FDR=2.0e-02, amino acids (alpha amino acids FDR=8.3e-04), as well as carbohydrates
555 (hexose metabolic process FDR=6.3e-2), whose catabolism appears also enriched
556 among proteins downregulated in the mutant (e.g. glycolytic process FDR=2.2e-2 and
557 carbohydrate catabolic process FDR=4.7E-2). The simultaneous enrichments of these
558 metabolic pathways observed both among upregulated and downregulated vesicular
559 proteins (**Fig S7**), indicates a complex, VirR-dependent, rewiring of metabolic routes in
560 the vesicles from the mutant strain.
561 Further, proteins upregulated in *virR*^{mut} EVs (N=117) were enriched in terms related to
562 mycolic acids metabolic processes (FDR=2.1E-2), and peptidoglycan-based cell-wall
563 biogenesis (FDR=9.0 e-02). Proteins such as InhA (logFC=3.71, 2.26 FDR=2.20 e-05,
564 and 1.4E-3 for comparisons *virR*^{mut} vs WT and *virR*^{mut} vs *virR*^{mut}-Comp, respectively),
565 and KasB (logFC=1.83; 2.49 FDR=2.23 e-02; 4.4e-3), involved in mycolic acid
566 metabolism were also upregulated in *virR*^{mut} (**Fig 6H**).
567 The upregulation of these proteins, along with the enrichments at the transcriptional level
568 of DIM/DIP biosynthetic pathways (upregulated in *virR*^{mut}), suggests a shift in the control

569 of the pool of propionyl-CoA, both at the level of its production, -as a byproduct of the
570 catabolism of methyl-branched lipids, odd-chain-length fatty acids as well as cholesterol-
571 and its detoxification by the bacterium through different routes, such as the
572 methylmalonyl pathway, the glyoxylate cycle and the methylcitrate cycles (Lee et al.,
573 2013). To shed light on these changes at the metabolic level, we conducted a metabolic
574 profiling to quantify the concentration of metabolites that are central in these different
575 detoxification routes including propionyl-CoA: acetyl-CoA, pyruvate, methylcitrate, and
576 methylmalonyl-CoA (**Fig 6I**). Only methylmalonyl-CoA was found to be significantly
577 repressed in *virR*^{mut} (p=0.028). We also observed differences between *virR*^{mut} and *virR*^{mut}
578 -Comp strains in methylcitrate. This result, along with the trend towards increased
579 protein, and especially gene expression that is observed for genes involved in the
580 biosynthesis of PDIMs from methylmalonyl (including phenolpthiocerol synthesis type-I
581 polyketide synthases A-E, (ppsA-E, **Fig 6I**), among others), suggests that the
582 methylmalonyl pool is depleted in the mutant strain because of an increased activity of
583 the PDIM biosynthetic pathway. Furthermore, most of the subunits of the
584 acetyl/propionyl-CoA carboxylase Acc (AccA1, AccA2, AccA3, AccD1, AccD5 appear
585 repressed in *virR*^{mut} EVs (**Fig 6I**), suggesting that the production of methylmalonyl Co-A
586 from the degradation of propionyl CoA is inhibited within EVs of the mutant strain.
587 Taken together, the omics analyses align with the structural and functional differences
588 observed in *virR*^{mut}. We reasoned that the increased expression of PDIMs biosynthetic
589 genes and the reduced expression of genes related to protein synthesis may be triggered
590 to compensate the enhanced permeability measured in *virR*^{mut}. In addition, this enhanced
591 permeability leads to an increase in the release of EV, which seems to be depleted in
592 ribosomes and iron storage proteins.
593
594 **The absence of VirR leads to an aberrant enlargement of PG in *Mtb***. To elucidate
595 the specific molecular defects that explain the periplasm enlargement, the enhanced
596 permeability, and the antibiotic sensitivity phenotypes, we performed a biochemical
597 analysis of WT and *virR*^{mut} cell envelopes. First, we analyzed the total lipid profile by
598 liquid chromatography-mass spectrometry (LC-MS) and observed significant differences
599 in prevalent polar lipids linked to the cell membrane including, lysophosphatidic and
600 phosphatidic acid, species of monoacylated and diacylated glycerol,
601 phosphatidylethanolamines and phosphatidyl-myo-inositol mannoside (PIM) species,
602 being more abundant in *virR*^{mut} relative to WT and complementing strain. (**Fig 7A**). To
603 validate these results, we ran thin layer chromatography (TLC) experiments on the same
604 lipid extracts and found that the mutant carries more phospholipids in the membrane
605 including more $AcPIM_2$ and PE (**Fig 7B**). Moreover, we could not measure major

606 differences in the level of mycolic acid species (**Fig 7C**), while significantly more PDIMs
607 were detected in the mutant relative to the other strains (**Fig 7D**). This later result partially
608 validates proteomics and metabolomic data and suggest that the methylmalonyl pool is
609 depleted in the mutant strain because of an increased activity of the PDIM biosynthetic
610 pathway. However, other lipids including SL1 or PAT/DAT that share a common
611 precursor (propionyl- CoA) with PDIM may also explain the depletion of methylmalonyl.
612 Notably, we observed a reduction in the level of these lipids (SL1 or PAT/DAT) in *virR*^{mut}
613 cultured in glycerol relative to WT and complemented strains, suggesting that the excess
614 of PDIM synthesis can take away methyl malonyl CoA from the biosynthesis of SL-1 and
615 PAT/DAT in the absence of VirR (**Fig S8**).
616 When analyzing apolar lipids, we also observed increased levels of free mycolic acids
617 (FMA) and free fatty acids (FFA) upon *virR* deletion (**Fig 7E**). The enhanced release of
618 these apolar lipids has also been documented in a *C. glutamicum* mutant in Cg0847
619 (Baumgart et al., 2016), a canonical LCP protein. Importantly, we could not detect any
620 of these lipids in EVs from *virR*^{mut} (**Fig 7F**), while major polar phospholipids could be
621 resolved in EVs from all strains (**Fig 7G**), as previously reported (Prados-Rosales et al.,
622 2011). This result indicates that *Mtb* releases free apolar lipids independently from
623 membrane associated EVs.
624 Next, we performed a glycosyl composition analysis of isolated cell walls (including
625 mycolyl-arabinogalactan-peptidoglycan complex) and determined that there were no
626 significant differences between strains in AG content as well as in the ratio between
627 arabinose and galactose (A/G) (**Fig 8A**). Similarly, no changes were observed in the
628 galactan length as measured by the ratio between galactose (G) and rhamnose (R) G/R)
629 (Justen et al., 2020). We noticed that the ratio between N-acetylglucosamine (NAGc)
630 and rhamnose (R) (NAGc/R) was significantly higher in *virR*^{mut} relative to WT, suggesting
631 an increase in PG content in this strain (**Fig 8A**). The validation of these results was
632 performed independently by measuring the amount of diaminopimelic acid (DAP) in
633 isolated cell walls, as a surrogate of PG content, and determined that *virR*^{mut} carries two
634 times more PG than WT or complemented strains (**Fig 8B**).
635 We next obtained pure PG preparations of each strain and performed an analysis by
636 atomic force microscopy (AFM) (**Fig 8C and Fig S9**). This technique has been recently
637 used to investigate the nanometric features of isolated Gram-positive bacterial cell walls
638 (Pasquina-Lemonche et al., 2020). Semi-automated analysis of liquid AFM images from
639 mycobacterial isolated PG samples revealed that: (i) the absence of VirR leads to a
640 significant reduction in PG pore diameter (down to 9.2 ± 0.6 nm) relative to WT (16 ±
641 3.3 nm) and complemented strains (10 ± 0.8 nm) (**Fig 8C, D and Fig S9**); (ii) the number
642 of pores is significantly higher in *virR*^{mut} compared to WT and complemented strain (**Fig**

643 **8E and Fig S9**); (iii) manual analysis of AFM images in ambient conditions revealed that
644 *virR*^{mut} PG is significantly thicker than that of the other strains of the study (**Fig 8F**). These
645 results show for the first time the nanometric architecture of isolated PG in mycobacteria
646 by AFM and suggest a role for VirR in regulating PG thickness and porosity. Strikingly,
647 we found that the PG enlargement observed in the *virR*^{mut} correlated with increased
648 susceptibility to the muramidase lysozyme (**Fig S10**), indicating modifications in PG
649 remodeling in *virR*^{mut}. In fact, a deeper MS analysis of PG showed a significant increase
650 in the abundance of deacetylated muropeptides in *virR*^{mut} relative WT and *virR*^{mut}-Comp
651 strain (**Fig 8G, H**). This PG feature has been linked to variability in lysozyme susceptibility
652 in other Gram positive bacterial species (Bera et al., 2005). Collectively, although the
653 structural changes at nanoscopic level of the peripheral areas of the cell observed by
654 AFM leads to a more dense and thick structure harder to penetrate, the chemical
655 changes in the peptidoglycan structure observed and biochemical assays suggest that
656 changes associated with alterations in VirR-regulated PG remodeling makes the wall
657 more permeable and support increased release of EV in *Mtb*.
658
659 **VirR interacts with canonical LCP proteins**. As mentioned above VirR is a LytR_C
660 solo domain protein with no catalytic LCP domain. Other members of the LCP protein
661 family like Rv3267 and Rv3287 are the main PG-AG ligases (Grzegorzewicz et al., 2016;
662 Harrison et al., 2016) and also carry a LytR_C domain. We have previously shown that
663 VirR interacts with itself (Rath et al., 2013). Consequently, we reasoned that if VirR
664 contributed to PG-AG ligation it could do it via interaction with canonical LCP proteins
665 through the LytR_C domain. Although VirR is one of the most abundant proteins found
666 in tuberculin preparations (Prasad et al., 2013), we determined that it localizes at sites
667 of nascent cell wall by fluorescence microscopy (**Fig S11**). Therefore, its location could
668 initially allow for interactions with other cell surface proteins like LCP. Both recombinant
669 VirR and the main AG-PG ligase Lcp1 (Rv3267) oligomerize in a blue-native PAGE gel
670 (**Fig 9A**). This observation suggests that they interact with proteins sharing similar
671 domain features. We next performed a flotation assay where we examined the behavior
672 of VirR on an iodixanol gradient in the presence or absence of Lcp1. Using a specific
673 antibody raised against VirR, we observed that the presence of Lcp1 displaces the
674 relative location of VirR toward upper fractions of the gradient, indicating a potential
675 interaction of both proteins and the formation of higher molecular weight complexes (**Fig
676 9B**). To investigate the interaction of virR and Lcp1, along with other Lcp proteins, in a
677 more physiological environment we used the bipartite splitGFP approach (Cabantous et
678 al., 2013) (**Fig 9C and Fig S12**), which has been recently utilized to demonstrate the co-
679 localization and interaction of the membrane-bound metal ATPase CtpC with the

680 chaperon PacL1 (Boudehen et al., 2022). We first recapitulated the VirR self-interaction
681 and added that such interaction implicates the LytR_C domain since no differences in
682 fluorescence were measured between full and truncated versions of VirR (VirRsol)
683 lacking the first 41 amino acids. As negative controls, we included interactions between
684 VirR and the cell surface associated metal ATPase CtpC (**Fig 9C**). When testing
685 interactions between VirR and other Lcp proteins (Rv0822c, Lcp1 (Rv3267) and Rv3284)
686 we could not measure any GFP signal when full Lcp proteins were used in the assay.
687 Conversely, a significant increase in fluorescence was measured for all combinations
688 when truncated Lcp proteins including either the C-terminal domain or specifically the
689 LytR_C domain were tested (**Fig 9C**). These results strongly suggest that VirR interacts
690 with Lcp proteins and that these interactions occur via LytR_C terminal domains.
691

692 **DISCUSSION**

693 We reported *virR* as the first gene implicated in the biogenesis of EVs in *Mtb* ten years
694 back (Rath et al., 2013). A transposon mutant in *virR* (*virR*^{mut}) overproduces MEVs and
695 this provokes augmentation of cytokine responses in mouse and human macrophages.
696 This mutant manifested an attenuated phenotype in experimental infections on
697 macrophages and mice (Beaulieu et al., 2010; Rath et al., 2013). Such studies
698 established that VirR has a role in virulence by negatively modulating the release of
699 MEVs. These studies provided evidence that vesiculogenesis in *Mtb* is genetically
700 regulated. Since then, conditions such as iron starvation (Prados-Rosales et al., 2014b)
701 and other genes, including the bacterial dynamin-like *iniAC* (Gupta et al., 2023), and the
702 Pst/SenX3-RegX3 signal transduction system (White et al., 2018) have been shown to
703 contribute to the biogenesis of MEVs. Interestingly, VirR, a LytR_C solo domain protein
704 (**Fig S1**), shares homology with Lcp proteins, which in *Mtb* are known to participate in
705 the enzymatic connection between AG and PG (Grzegorzewicz et al., 2016; Harrison et
706 al., 2016). This suggests VirR function might be linked to cell wall remodeling.

707 In this study, we investigated how VirR can control the magnitude of MEV release
708 in *Mtb*. We did this by studying the underlying enhanced vesiculogenesis phenomenon
709 observed in *virR*^{mut} using genetic, transcriptiomics, proteomics and ultrastructural and
710 biochemical methods. It was clear from our cryo-EM studies that *virR*^{mut} has an aberrant
711 cell wall as the layer above the cell membrane was significantly larger than that of WT
712 and complemented strains. The enlarged compartment showed higher granular texture,
713 a feature that has been previously associated to PG precursors in unrelated Gram-
714 positive bacteria (Zuber et al., 2006). This observation and previous studies showing the
715 increased sensitivity of *VirR*^{mut} to vancomycin (Ballister et al., 2019) strongly suggested
716 that the cell wall defect is connected to PG remodeling. The use of AFM on isolated PG

717 confirmed this and showed for the first time the nanostructure of PG in *Mtb*, providing
718 information on PG thickness, pore size and number of pores. AFM indicated that *virR*^{mut}
719 PG is thicker, has significantly more pores of small size. Considering the pore sizes
720 measured across strains (ranging from 9-16 nm), we initially ruled out the notion that
721 EVs (which are spheres of 50-300 nm in diameter) are released through the peripheral
722 cell wall. Therefore, *Mtb* must have an alternative mechanism to release EVs, possible
723 during the division process where the PG is most fragile, presumably due to defects in
724 crosslinking, something that awaits further experimental verification. These events were
725 not possible to visualize in AFM given that PG fragments from all the strains were lacking
726 the poles or clearly defined division sites but could be the subject of further studies in the
727 future. However, we cannot exclude that MEV plasticity could allow for crossing the cell
728 wall via PG pores.

729 A recent study showed that *Corynebacterium glutamicum* can produce and
730 release different types of MVs through different routes, including mycomembrane
731 blebbing or bubbling cell death, depending on the stress at which *C. glutamicum* is
732 exposed (Nagakubo et al., 2021). In the present study, we have shown that *virR*^{mut}
733 overproduces EVs under normal growing conditions in the absence of cell lysis,
734 according to our assay which measured cytoplasmic leaking of the transcription factor
735 IdeR or serially diluted spots on solid medium. Overall, we show that EV production in
736 *Mtb* under our growing conditions, is not linked to cell death. This fact largely excludes
737 the bubbling cell death mechanism. Moreover, our lipidomic analysis now and before
738 (Prados-Rosales et al., 2011) indicates the absence of mycomembrane lipids in isolated
739 MEVs from all strains, ruling out that MEVs originate at the mycomembrane. These
740 apparent disagreements with the *C. glutamicum* study (Nagakubo et al., 2021) might
741 indicate that *Mtb* EV biogenesis may differ from that of *C glutamicum*, and other mycolic
742 acid-containing bacteria with shorter fatty acids. Additional variables that may explain
743 differences between studies is the growth media and the time at which vesicles are
744 isolated (Gupta et al., 2023). Of note, *M. smegmatis* EVs were isolated at day 6
745 (Nagakubo et al., 2021), a time at which this fast-growing mycobacteria is already in
746 stationary phase.

747 The transcriptional profile of *virR*^{mut} can provide a partial explanation for the
748 attenuated phenotype of the mutant due to a downregulation of genes activated upon
749 stresses associated to the intraphagosomal environment. It is particularly interesting to
750 observe the specific reduction in transcript levels of the two most important effectors of
751 the esx-1 secretion system. On the other hand, genes involved in PDIM synthesis were
752 upregulated. It is possible that the specific upregulation of PDIM synthesis in absence of
753 *virR* is part of compensatory response to a reduced permeability. We were surprised to

754 find no differences between protein profiles in whole cells between WT and *virR*^{mut}
755 strains, despite difference in transcriptomics. A biological interpretation of these results
756 would point to the existence of global compensatory mechanisms of post-transcriptional
757 regulation used by the bacteria to partially recover comparable proteomic profiles in
758 *virR*^{mut} to those observed in the WT.

759 Contrary to whole cell lysates, EV protein profiles between *virR*^{mut} and WT were
760 largely different. In this context, it is accepted that certain proteins and lipids are enriched
761 in bacterial EVs and that preferential inclusion of such antigens in MVs supports a
762 specific vesicle biogenesis mechanism. In Gram positive bacteria and mycobacteria both
763 membrane and cytosolic proteins are included in EVs since the origin of these structures
764 is linked to the cell membrane (Prados-Rosales et al., 2011) and, presumably, the
765 incorporation of intracellular proteins may occur during the process of vesicle formation.
766 We found a higher abundance of proteins related to PG and MA synthesis in *virR*^{mut} EVs
767 relative to WT. Therefore, these two processes seem to contribute to EV biogenesis in
768 *Mtb*. Additional data presented in this study, which includes ultrastructural and chemical
769 analyses confirm this. Both PG and MA synthesis are complex processes, including a
770 diverse set of genes. What parts of the biogenesis of these molecules are important for
771 the formation of EVs is a matter of future investigations.

772 Another finding of the study is the connection between permeability and the
773 magnitude of the vesiculation process in *Mtb*. We linked these two phenomena first, by
774 measuring enhanced vesiculation and permeability in the same strain (*virR*^{mut}) and
775 second, by modifying the permeability using chemical (via sublethal exposure to TRZ)
776 and nutritional supplements (via providing cholesterol as sole carbon source) in WT *Mtb*.
777 TRZ, a repurposed drug that belongs to the class of phenothiazines, is known to affect
778 respiration in *Mtb* (Amaral et al., 1996). It is also assumed that TRZ can inhibit efflux
779 pumps leading to an increased susceptibility to first line antitubercular drugs when tested
780 in combination (De Knegt et al., 2014). This provides an explanation for the synergistic
781 effects of such combinations. An independent explanation of such synergy may also
782 come from the increased permeability, as it has been recently shown by a quantitative
783 proteomics analysis of *Mtb* cells exposed to sublethal concentration of TRZ (De Keijzer
784 et al., 2016). When we grew *Mtb* with cholesterol as a sole carbon source, a condition
785 that slows mycobacterial growth but also reduces cell permeability via cholesterol
786 accumulation in the cell wall (Brzostek et al., 2009), we observed the opposite trend on
787 MEV biogenesis. We consider this finding of high relevance since *Mtb* permeability is
788 one the major concerns when developing potential antimycobacterial drugs.
789 Nevertheless, bacterial cell permeability is a complex property that it is controlled by
790 physiochemical, biological, and chemical processes such as stereochemistry,

791 lipophilicity, saturation and unsaturation, flexibility, viscosity, fluidity, pressure,
792 temperature and physiological conditions (Nagamani and Sastry, 2021). How these
793 variables change to allow the release of MEVs is not known.
794 This study also proposes a model VirR function whereby VirR may work as a
795 scaffold for canonical Lcp proteins, which in *Mtb* links PG to AG. Based on the
796 demonstration that VirR interacts with canonical Lcp proteins, we believe that the
797 absence of VirR deregulates the localization of canonical Lcp proteins. Although we
798 cannot rule out the contribution of other phenomena including alteration of the PG
799 molecule, VirR is a central scaffold in the cell wall remodeling process. Taking into
800 consideration the fact that *VirR*^{mut} is attenuated in virulence on preclinical models of
801 infections and manifests an enhanced vesiculogenesis and permeability, VirR may
802 represent a novel and interesting drug target. We envision that targeting VirR may not
803 only make *Mtb* weaker and more permeable to other antitubercular drugs, but to
804 stimulate the immune system, via MEVs, to fight infection.
805
806 **MATERIALS AND METHODS**
807
808 **Bacterial Strains, media and growth conditions.** *Mtb* H37Rv (ATCC) and derivative
809 strains *virR*^{mut} and *virR*^{mut}*-C* (complemented strain) (Rath et al., 2013) were used in this
810 study. Bacteria were initially grown in Middlebrook 7H9 medium (7H9) supplemented
811 with 10% (v/v) oleic acid-albumin-dextrose-catalase (OADC) enrichment (Becton
812 Dickinson Microbiology Systems, Spark, MD, United States), 0.5% (v/v) glycerol and with
813 Tyloxapol 0.05% (v/v; Sigma-Aldrich, Burlington, MA, United States) prior to inoculation
814 in a minimal medium (MM) consisting of KH_2PO_4 1 g/l, Na_2HPO_4 2.5 g/l, asparagine
815 0.5 g/l, ferric ammonium citrate 50 mg/l, $CaCl_2$ 0.5 mg/l, $ZnSO_4$ 0.1 mg/l, without
816 Tyloxapol 0.05% (v/v), containing 0.7% (v/v) glycerol, pH 7.0.
817 *Mtb* was also cultured in MM in the presence of sublethal concentrations of
818 thirodazine (TRZ) of 6 μgml^{-1} as previously described. We determined that this
819 concentration does not affect cell growth. *Mtb* was also cultured in MM with cholesterol
820 as a sole carbon source as previously described (Brzostek et al., 2009).
821 *Mtb* expressing fluorescent VirR was generated by cloning VirR into pMV261-
822 Venus using fast cloning approach (Li et al., 2011).
823 *M. smegmatis* mc^{2}155 (ATCC 700084) and recombinants derived from this strain
824 were grown at 37°C in 7H9 medium (Difco) supplemented with 10% albumin-dextrose-
825 catalase (ADC, Difco) and 0.05% Tween-80 (Sigma-Aldrich), or on complete 7H11 solid
826 medium (Difco) supplemented with 10% OADC(Difco). When needed, streptomycin (25
827 μg ml^{-1}) was added to the culture media. *Escherichia coli* strains StellarTM (Takara bio,

828 San Jose, CA, United States) were grown at 37°C in LB broth (Difco) or on L-agar plates
829 (Difco) supplemented with streptomycin (25 μg ml^{-1}) when required.
830
831 ***M. smegmatis* expression vectors for split GFP experiment.** Plasmids used for split
832 GFP experiments were constructed by modifying the plasmid pGMCS-PpacL1-pacL1-
833 Lk2-GFP11-ctpC(1-85)-Lk15-GFP(1-10) (Boudehen et al., 2022) (**Table S1**). Plasmids
834 pGMCS, conferring resistance to streptomycin, are shuttle vectors, episomal in *E. coli*
835 and integrative in mycobacteria through insertion at the attL5 mycobacteriophage
836 insertion site in the glyV tRNA gene. Lk2 (LEGSGGGGSGGGS) and Lk15
837 (GPGLSGLGGGGGSLG) are flexible linkers separating the protein domains of interest
838 from the last 11th b-sheet or the first ten b-sheets of GFP, respectively. First, the Zinc-
839 inducible PpacL1 promoter was replaced by P1, a strong constitutive promoter from *M.*
840 *smegmatis* (Ariyachaokun et al., 2020), resulting in pGMCS-P1-pacL1-Lk2-GFP11-
841 ctpC(1-85)-Lk15-GFP(1-10). Second, the pacL1 (Rv3269) sequence was replaced by
842 that of virR (encoding amino-acids 1 to 164) or virRsol (encoding amino-acids 42 to 164)
843 by In-Fusion HD cloning (Takara). PCR fragments were amplified using appropriate
844 primer pairs (**Table S1**) and Phusion High-Fidelity PCR Master Mix with GC Buffer
845 (Thermo Scientific, Walthman, MA, United States). Linear fragments were purified on
846 agarose gels and inserted into pGMCS backbone linearized by PCR amplification with
847 appropriate primers, using the In-Fusion HD Cloning Kit (Takara), following the
848 manufacturer's instructions. Finally, the ctpC sequence was replaced on the resulting
849 plasmids by the virR or virRsol sequences, or that encoding either the C-terminal part or
850 only the LytR_C domains of the Rv0822c, Rv3267 or Rv3484 proteins from *M.*
851 *tuberculosis* H37Rv. Plasmids were constructed by transformation into *E. coli* Stellar
852 recipient cells. All plasmids were verified by sequencing before introduction by
853 electroporation into *M. smegmatis* mc^2155 strain.
854
855 **H_20_2 sensitivity assays**. Bacterial strains were initially cultured in 7H9+ADN until they
856 reached an OD600nm of 0.5. Cells were washed in PBS and transferred to roller bottles
857 including the same medium and 13 mM H_20_2. After 8 h, bacterial cultures were serially
858 diluted and spotted onto 7H10 solid medium.
859
860 **Generation of the CRISPR mutants.** To generate the conditional CRISPR mutants we
861 took advantage of the CRISPR interference (CRISPRi) technology (Rock et al., 2017).
862 Briefly, we designed sgRNA oligonucleotides containing the target Rv0431 (*virR*) and
863 Rv2700 (*cei*) genes sequences (**Table S1**) located immediately upstream of the PAM
864 sequence. The strengths of the PAM sequence were chosen following authors

865 recommendation to get high and intermediate gene repression, 158.1 or 42.2-fold
866 repression for *virR* and 145.2 and 47.3 for *cei*, respectively. The primers were annealed
867 and ligated into the gel purified BsmBI-digested CRISPRi vector (pIJR965 plasmid)
868 followed by transformation of competent *Mtb* cells via electroporation. Transcriptional
869 knockdown of genes were quantified by qRT-PCR; and protein levels were examined by
870 immunoblot using specific antibodies raised against VirR (Rath et al., 2013) and Cei
871 (Ballister et al., 2019) **.**
872
873 **EV isolation and purification.** *Mtb*-EV were prepared and purified as previously
874 described. Briefly, the culture filtrate of 1 L cultures of *Mtb* grown in low iron MM without
875 detergent for 14 days was processed for vesicle isolation by differential centrifugation. In
876 parallel a 2 ml culture in MM supplemented with 0.05% Tyloxapol to disperse bacterial
877 clumps was used to determine viability by plating culture dilutions onto 7H10 agar plates
878 and enumerating colony forming unit (CFU) at the time of culture filtrate collection.
879 The membranous pellet containing vesicles obtained after ultracentrifugation of the
880 culture filtrate at 100,000 × g for 2 h at 4°C, was resuspended in 1 ml sterile phosphate-
881 buffered saline (PBS) and overlaid with a series of Optiprep (Sigma-Aldrich) gradient
882 layers with concentrations ranging from 30% to 5% (w/v). The gradients were centrifuged
883 at 100,000 × g for 16 h. At the end 1 ml fractions were removed from the top, diluted to
884 20 ml with PBS and purified vesicles recovered by sedimentation at 100,000 × g for 1 h.
885 Vesicle pellets were suspended in PBS before analysis. Protein concentration was
886 measured by Bradford assay (Bio Rad, Hercules, CA, United States) according to
887 manufacturer instructions. For all conditions test from which EVs were isolated,
888 normalization was performed by referring EVs concentration to colony forming units
889 (CFUs).
890
891 **Nano particle tracking analysis (NTA).** NTA was conducted using ZetaView (Particle
892 Metrix, Winning am Ammersee, Germany). Instrument calibration was performed prior
893 to EV analysis using 102 nm polystyrene beads (Thermo Fisher Scientific), according to
894 manufacturer instructions. Measurements were performed using a 405 nm 68 mW laser
895 and CMOS camera by scanning 11 cell positions and capturing 60 frames per position
896 at 25 C with camera sensitivity 85, shutter speed 100, autofocus and automatic
897 scattering intensity. Samples were diluted in pre-filtered PBS to approximately 106-107
898 particles·ml^{-1} in Millipore DI water. Analysis was performed using ZetaView Software
899 version 8.05.12 SP1 with a minimum brightness of 30, maximum brightness of 255,
900 minimum area of 5, maximum area of 1000, and s minimum trace length 15. Triplicate
901 videos of each sample were taken in light scatter mode. Particle size and concentration

902 were analyzed using the built-in EMV protocol and plotted using Prism software, version
903 8.0.1 (GraphPad Inc., San Diego, CA, United States).
904
905 **Electron-Microscopy.** Cells were fixed with 2% glutaraldehyde in 0.1 M cacodylate at
906 room temperature for 24 h, and then incubated overnight in 4% formaldehyde, 1%
907 glutaraldehyde, and 0.1% PBS. For scanning microscopy, samples were then
908 dehydrated through a graded series of ethanol solutions before critical-point drying using
909 liquid carbon dioxide in a Toumisis Samdri 795 device and sputter-coating with gold-
910 palladium in a Denton Vacuum Desk-2 device. Samples were examined in a Zeiss Supra
911 Field Emission Scanning Electron Microscope (Carl Zeiss Microscopy, LLC, North
912 America), using an accelerating voltage of 5 KV.
913 For Cryo-EM, grids were prepared following standard procedures and observed
914 at liquid nitrogen temperatures in a JEM-2200FS/CR transmission electron microscope
915 (JEOL Europe, Croissy-sur-Seine, France) operated at 200 kV. An in-column omega
916 energy filter helped to record images with improved signal/noise ratio by zero-loss
917 filtering. The energy selecting slit width was set at 9 eV. Digital images were recorded on
918 an UltraScan4000 CCD camera under low-dose conditions at a magnification of 55,058
919 obtaining a final pixel size of 2.7 Å/pixel.
920 Density profiles were calculated along rectangular selections with the ImageJ
921 software (NIH, Bethesda, MD, United States). The number of cells analyzed varied from
922 n = 20 (WT), n = 15 (*virR*^{mut}) and n = 23 (*virR*^{mut}-C). The comparisons extracted from this
923 data is statistically relevant with t test with Welch's correction performed. For each cell
924 three representative measurements were obtained. Mean and standard error was then
925 calculated for measurements pooled for each strain.
926
927 **Western Dot blot.** Two µl of EV isolates and two-fold serial dilutions were spotted onto
928 a nitrocellulose membrane (Abcam, Cambridge, United Kingdom) and process for dot
929 blot using anti-EV polyclonal murine serum (Prados-Rosales et al., 2014a) as primary
930 antibody and goat anti-mouse-HRP conjugated as secondary antibody and ECL prime
931 Western Blotting Detection chemiluminescent substrate (GE Healthcare, Chicago, IL,
932 United States). The signal was visualized in a Chemidoc MP imaging system (Bio Rad)s).
933
934 **RNA sequencing.** *Mtb* strains were grown in MM supplemented with 0.05% Tyloxapol
935 at 37ºC until they reached an OD595nm of 0.3 and harvested by centrifugation. The cell
936 pellets were resuspended in 1 ml Qiagen RNA protect reagent (Qiagen, Venlo,
937 Netherlands) and incubated for 24 h at room temperature. Cells were disrupted by
938 mechanical lysis in a FastPrep-24 instrument (MP Biomedicals, Santa Ana, CA, United

939 States) in Lysing Matrix B tubes and RNA was purified with the Direct-zol RNA miniprep
940 kit (Zymo Research, Irvine, CA, United States). The quantity and quality of the RNAs
941 were evaluated using Qubit RNA HS Assay Kit (Thermo Fisher Scientific) and Agilent
942 RNA 6000 Nano Chips (Agilent Technologies, Santa Clara, CA, United States),
943 respectively. Sequencing libraries were prepared using the Ribo-Zero rRNA Removal Kit
944 (Gram-positive Bacteria) (Illumina Inc., San Diego, CA, United Stated) and the
945 TruSeqStranded mRNA library prep kit (Illumina Inc), following the Ribo-Zero rRNA
946 Removal kit Reference guide and the "TruSeqStranded mRNA Sample Preparation
947 Guide. Briefly, starting from 1 µg of total RNA, bacterial rRNA was removed and the
948 remaining RNA was cleaned up using AgencourtRNAClean XP beads (Beckman
949 Coulter). Purified RNA was fragmented and primed for cDNA synthesis. cDNA first strand
950 was synthesized with SuperScript-II Reverse Transcriptase (Thermo Fisher Scientific)
951 for 10 min at 25°C, 15 min at 42°C, 15 min at 70°C and pause at 4°C. cDNA second strand
952 was synthesized with Illumina reagents at 16°C for 1 hr. Then, A-tailing and adaptor
953 ligation were performed. Libraries enrichment was achieved by PCR (30 sec at 98°C; 15
954 cycles of 10 sec at 98°C, 30 sec at 60°C, 30 sec at 72°C; 5 min at 72°C and pause at 4°C).
955 Afterwards, libraries were visualized on an Agilent 2100 Bioanalyzer using Agilent High
956 Sensitivity DNA kit (Agilent Technologies) and quantified using Qubit dsDNA HS DNA
957 Kit (Thermo Fisher Scientific). Library sequencing was carried out on an Illumina
958 HiSeq2500 sequencer with 50 nucleotides single end reads and at least 20 million reads
959 per individual library were obtained.
960
961 **RNA-sequencing data analysis.** Quality Control of sequenced samples was performed
962 by FASTQC software (http://www.bioinformatics.babraham.ac.uk/projects/fastqc/).
963 Reads were mapped against the *M. tuberculosis* H37Rv strain
964 (GCF_000195955.2_ASM19595v2) reference genome using Tophat (Trapnell et al.,
965 2009) with --bowtie1 option, to align 50 bp reads. The resulting BAM alignment files for
966 the samples were the input to Rsubread's (Liao et al., 2019) featureCounts function to
967 generate a table of raw counts required for the Differential Expression (DE) analysis.
968 Data preprocessing and differential expression analysis of the transcriptomic data was
969 performed using DeSeq2 (Love et al., 2014). Genes with a median of expression lower
970 than 1 CPM, and genes containing outlier observations were filtered before statistical
971 modeling, and the remaining N=4004 genes were used for differential expression
972 analysis. P-values were corrected for multiple testing using the R package, implementing
973 the Storey-Tibshirani FDR correction method (Storey et al., 2023). Genes with an
974 FDR<0.05 were deemed as differentially expressed. Data were deposited at Gene
975 expression Omnibus (GEO); GSE143996.

976

977 **Label-free mass spectrometry analysis**. Total cell proteins and MEV-associated
978 proteins were submitted to LC-MS label-free analysis using a Synapt G2Si ESI Q-
979 Mobility-TOF spectrometer (Waters) coupled online to a NanoAcquity nano-HPLC
980 (Waters), equipped with a Waters BEH C18 nano-column (200mm x 75 um ID, 1.8um).
981 Samples were incubated and digested following the filter-aided sample preparation
982 (FASP) protocol (Wiśniewski et al., 2009) Trypsin was added to a trypsin:protein ratio of
983 1:50, and the mixture was incubated overnight at 37°C ,dried out in a RVC2 25 speedvac
984 concentrator (Christ), and resuspended in 0.1% FA. Peptides were desalted and
985 resuspended in 0.1% FA using C18 stage tips (Millipore). Digested samples (500 ng)
986 were loaded onto the LC system and resolved using a 60 min gradient (5 to 60% ACN).
987 Data was acquired in HDDA mode that enhances signal intensities using the ion mobility
988 separation step. Protein identification and quantification were carried out using
989 Progenesis LC-MS (version 2.0.5556.29015, Nonlinear Dynamics). One of the runs was
990 used as the reference to which the precursor masses in all other samples were aligned
991 to. Only features comprising charges of 2+ and 3+ were selected. The raw abundances
992 of each feature were automatically normalized and logarithmized against the reference
993 run. Samples were grouped in accordance with the comparison being performed, and an
994 ANOVA analysis was performed. A peak list containing the information of all the features
995 was generated and exported to the Mascot search engine (Matrix Science Ltd.). This file
996 was searched against a Uniprot/Swissprot database, and the list of identified peptides
997 was imported back to Progenesis LC-MS. Protein quantitation was performed based on
998 the three most intense non-conflicting peptides (peptides occurring in only one protein),
999 except for proteins with only two non-conflicting peptides.
1000

1001 **Proteomics data analysis**. Normalization and imputation of the proteomics data was
1002 done using the DEP package for R (Zhang et al., 2018). Normalization was done using
1003 the vsn method (Huber et al., 2002), which transforms data tackling heteroskedasticity.
1004 Imputation of missing values was performed using the bpca method (Oba et al., 2003),
1005 which leans on principal component analysis to impute missing values.
1006 Data was analyzed according to a design where differences between strains (*virR*^{mut} vs
1007 -WT, as well as *virR*^{mut} vs *virR*^{mut}-Comp) were estimated independently within each cell
1008 compartment, (whole cell lysates or EVs). according to a nested design: Expression
1009 ~ Compartment + Strain:Compartment.
1010 Differential expression analysis of the proteomics data was performed using limma
1011 (Ritchie et al., 2015) and p-values were corrected for multiple testing according to the

1012 Storey-Tibshirani method using the R package qvalue (Storey et al., 2003). Proteins with
1013 an FDR<0.05 were selected as differentially expressed.
1014
1015 **Gene ontology (GO) enrichments.** Enrichment analyses of the sets of differentially
1016 expressed genes and proteins were performed in R using the terms of the Gene
1017 Ontology database for testing, version 11.02.2020. Gene sets corresponding to the
1018 biological process and cellular component ontologies between levels 4 to 6 (N=2245)
1019 were selected and filtered according to their size (minimum size =10 in the RNAseq
1020 analyses; and =3 in the proteomics analyses). The selected sets were tested for
1021 enrichment using Fisher's exact test among genes, or proteins consistently up, or down
1022 regulated in *virR*^{mut} with respect to both *virR*-expressing strains in each case. Multiple
1023 testing correction was performed using the qvalue R package (Storey et al., 2023).
1024 Terms with an FDR < 0.1 and an odds ratio > 2 were selected for visualization in figures
1025 3E, and 6F, where node sizes was proportional to the significance of the enrichments. In
1026 these visualizations, two terms were connected depending on the amount of sharing
1027 between the groups of genes contributing to the enrichments in each of them, drawing a
1028 link whenever the intersection between the groups of genes was larger than 50% of the
1029 smallest of the two gene sets involved. Ontology term clusters, represented by colors,
1030 were then assigned using the Louvain's algorithm for modularity optimization (Blondel et
1031 al., 2008), as implemented in the R package igraph (Csardi and Nepusz, 2006).
1032 Visualization of the resulting networks was done using the open-source software Gephi
1033 (Bastian et al., 2009).
1034
1035 **Targeted metabolomics.** LC-MS analysis was carried out on a Schimazdu LC/MS-8030
1036 coupled with a triple quadrupole mass analyser (QqQ) provided with an electrospray
1037 source in a negative ionization mode. Extracted metabolites were quantified in Multiple
1038 Reaction Monitoring (MRM) mode. A stock standard solution prepared in 17% (v/v)
1039 methanol in water and containing all metabolites: acetyl-CoA, methyl citrate,
1040 methylmalonyl-CoA, pyruvate, was used as external standard. Metabolites were
1041 identified by ion pairing liquid chromatography. Acetyl-CoA, methyl citrate and
1042 methylmalonyl-CoA were separated by reverse phase with a poroshell 120 Phenyl-Hexyl
1043 analytical column (2.1 x 50mm, 2.7 µm, Agilent) and a binary gradient (**Table S2**)
1044 consisting of a mobile phase A with water-methanol 97:3 (v/v), 10 mM tributylamine and
1045 3 mM acetic acid, and mobile phase B composed of pure methanol. Pyruvate was
1046 separated by normal phase using a Kinetex HILIC analytical column (2.1 x 150 mm, 2.6
1047 µm, Phenomenex) and a binary gradient (**Table S3**) consisting of pure water as mobile
1048 phase A and pure methanol as mobile phase B.

1049 The flow rate was maintained at 0.4 ml/min and the injection volume was 20 µl.
1050 Nitrogen was used as nebulizing and drying gas at a flow rate of 1.5 and 15 ml/min,
1051 respectively. The desolvation line (DL) temperature was set at 250°C and the ionization
1052 voltage was fixed at 4.5 kV. Argon was used as collision gas to perform collision-induced
1053 dissociation at a pressure of 230 kPa. The dwell time was set at 100 ms and the detection
1054 was performed in MRM mode (detector voltage of 1.8 Kv), monitoring three transitions
1055 for each compound. The transition with higher intensity was selected as quantitative
1056 purposes (**Table S4**), while the other two were used for confirmation of the identity.
1057
1058 **Lipidomic analysis by UPLC-MS**. The effect of virR on relative abundance of different
1059 cell wall lipids was characterized as had been done previously for MEVs (Prados-
1060 Rosales et al., 2014b). Briefly, cell wall lipids were extracted from triplicate 10 ml cultures
1061 of wild type, *virR*^{mut}, and *virR*^{mut} complemented (*virR*^{mut}-C) strains overnight into 3 ml 2:1
1062 chloroform:methanol at room temperature, extracts were dried under nitrogen before
1063 being dissolved in 0.75 ml LC-MS grade 2:1:1 isopropanol:acetonitrile:water. Extracts
1064 were separated on a Waters ACQUITY BEH C18 column UPLC heated to 55ºC and
1065 eluted at a flow rate of 0.4 ml/minute with 60:40 acetonitrile:water as mobile phase A and
1066 90:10 isopropanol:acetonitrile as mobile phase B, both containing 10 mM ammonium
1067 formate and 0.1% formic acid. Initial condition was 40%, B which increased to 43% at 2
1068 minutes, 50% at 2.1 minutes, 54% at 12 minutes, 70% at 12.1 minutes, 90% at 18
1069 minutes before returning to initial condition at 18.1 minutes to complete the run at 20
1070 minutes. The coupled Waters Synapt G2 q-TOF MS was operated in positive ion
1071 resolution mode with the following conditions: capillary voltage 2kV, cone voltage 30V,
1072 desolvation gas temperature 550°C , gas flow 900L/hour, source temperature 120°C.
1073 Mass spectra were acquired in centroid mode from 100-3000 m/z with scan times of 0.5
1074 second. Leucine enkephaline was used as reference. Relative abundances of Mass-
1075 retention time pairs were normalized to total ion current and lipid species were identified
1076 using Mycomass (Layre et al., 2011) and Mtb LipidDB databases (Sartain et al., 2011).
1077
1078 **Lipidomic analysis by thin layer chromatography (TLC)**. Lipidomic analysis of both
1079 whole cells and EVs by TLC was performed as previously described (Boldrin et al.,
1080 2021). *Mtb* strains were grown at 37°C in standing Middlebrook 7H9 and when they
1081 reached an OD595 of 0.2, cells were washed and transferred to MM. Cells were grown
1082 until they reached an OD595 of 0.5. Further, cells were harvested by centrifugation at
1083 3,500 rpm for 5 min, and pellets were heat-inactivated at 100°C for 1 h and used for lipid
1084 extraction. Five milliliters 2:1 (vol/vol) chloroform-methanol was added to the cell pellet
1085 and incubated at room temperature (RT) for 12 h with constant stirring. The organic

1086 extract was separated by centrifugation (1,000 × g, 5 min, RT) and decantation. The
1087 obtained pellet was extracted with 5 ml 2:1 (vol/vol) chloroform-methanol for 1 h at RT
1088 with constant stirring and separated under the same conditions. The combined two
1089 organic extracts (total lipids) were dried under a stream of nitrogen gas at RT and saved
1090 for lipid analysis.

1091 Polar lipids were separated by 2D-TLC by spotting 200 μg of total lipids on 60
1092 F254 silica gel plates (Merck) using chloroform, methanol, water (50:30:6) as a mobile
1093 phase 1 (first dimension), and chloroform, acetic acid, methanol, and water (40:25:3:6)
1094 as mobile phase 2 (second dimension). Analysis of PDIMs and TAGs was performed in
1095 a 1D-TLC format. Two hundred μg of total lipids were spotted on the silica plates and
1096 separated using 9:1 petroleum ether-diethyl ether as mobile phase. Free mycolates were
1097 separated by 1D-TLC using chloroform/methanol/ammonium hydroxide (80:20:2) as
1098 mobile phase. Mycolic acids were extracted and separated from cells as previously
1099 described (Vilchèze and Jacobs, 2007). Sulfolipids and diacyltrehaloses were separated
1100 using 60:12:1 chloroform/methanol/water as mobile phase. EV-associated lipids were
1101 separated and visualized following the same procedures as for WCLs. Development of
1102 TLC plates was performed by repeating the process of pulverizing the staining solution
1103 and heating the plate at 100°C 4 times. The staining solution contained 10.5 ml 15%
1104 ethanolic solution of 1-naphthol, 6.5 ml 97% sulfuric acid, 40.5 ml ethanol, and 4 ml
1105 water.

1106

1107 **PG isolation.** To obtain mycobacterial cell walls, whole cell pellets were resuspended in
1108 PBS and boiled for 15 min. Boiled cells were transferred to 2 ml Lysing matrix tubes with
1109 0.1 mm silica beads (M.P. Biomedical, Santa Ana, CA, United States). And mechanically
1110 disrupted in a FastPrep-24TM (M.P. Biomedical) giving 12 cycles at predetermined
1111 speed of 6 during 30 sec. Samples were allowed to chill on ice for 3 min between cycles.
1112 Cell breakage was monitored by optical microscopy (using Methylene blue as stain), if
1113 95% of the cells had not broken perform additional FastPrep-24TM cycles were
1114 performed. Lysed cells were centrifuged at 170 × g for 30 sec to separate them from
1115 beads and the supernatant were transferred to a clean 1.5 ml tube. The suspensions
1116 were further digested with 10 µg of DNase and RNase/ml for 1 h at 4˚C to obtain a cell
1117 wall-enriched fraction after centrifugation at 27,000 × g for 10 min. Cell walls were
1118 resuspended in PBS containing 2% sodium dodecyl sulfate (SDS) and the suspension
1119 was incubated for 1 h at 90˚C with constant stirring and recentrifuged at 27,000 × g for
1120 30 min, and the supernatant was discarded. This process was repeated twice. The
1121 resulting pellet was washed trice in distilled water, 80% acetone and acetone and
1122 lyophilized. Pellets were resuspended in 0.9 ml Tris-HCL (50 mM, pH 7) buffer, plus 0.1

1123 ml of protease K stock solution. The mixture was incubated at 60 ˚C for 90 min, to digest
1124 any remaining surface proteins attached to the CW and centrifuged again for 3 min at
1125 20,000 × g and resuspend pellet in distilled water. The mixture was then heated at 90˚C
1126 for 1 h before centrifugation at 27,000 × g for 30 min. The supernatant was discarded
1127 and washed twice with PBS and four times with deionized water to remove SDS. Pure
1128 PG was obtained from isolated cell walls. Briefly, pure cell walls were resuspended in
1129 0.5% KOH in methanol and stirred at 37˚C for 4 days to hydrolyze mycolic acids (MA).
1130 The mixture was centrifuged (27,000 × g 20 min) and the pellet was washed twice with
1131 methanol. MA were separated from cell walls using diethyl ether and recentrifuged at
1132 27,000 × gfor 20 min. The supernatant contained MAMEs. The extraction process with
1133 diethyl ether was repeated twice and let dry. The resulting arabinogalactan (AG)-PG was
1134 digested with 0.2 N H_2SO_4 at 85˚C for 30 min and neutralized with $BaCO_3$ to remove the
1135 arabinogalactan. Treated AG-PG was centrifuged at 27,000 × g for 20 min. Supernatant
1136 contained soluble AG. The resulting insoluble PG was washed four times by
1137 centrifugation in deionized water and stored at 4˚C or room temperature.
1138
1139 **Analysis of diaminopimelic acid.** For DAP quantification (Tsuruoka et al., 1985),
1140 samples were hydrolyzed overnight in 6N HCl at 100°C in 1 ml capacity-crystal ampoules
1141 (Wheaton). Samples were dried and resuspended in water and mixed in a 1:1:1 ratio
1142 with pure acetic acid and ninhydrin reagent (250 mg ninhydrin, 4 ml phosphoric acid 0.6
1143 M, and 6 ml pure acetic acid). Samples were measured at OD 434nm, and the amounts
1144 of DAP were calculated based on a standard curve with pure DAP. The data displays
1145 the average ± standard deviations n=3.
1146
1147 **Glycosyl composition of isolated cell walls**. 500 µg of purified cell walls were mixed
1148 with 10 µg of inositol and hydrolyzed with 0.1 M trifluoroacetic acid (TFA) for 2 h at 121°C.
1149 The monosaccharides released were then converted into alditol acetates by reduction
1150 with $NaBH_4$ and acetylation with acetic anhydride in pyridine. The products were
1151 analyzed by gas chromatography-mass spectrometry in a 7890A/5975C system from
1152 Agilent, using a DB-5ht (30 m x 0.25 mm x 0.1 µm) fused silica capillary column. The
1153 compounds were identified by comparing the retention times of the peaks with those
1154 recorded for standards analyzed under identical conditions. Quantification was carried
1155 out considering the area of the peaks and the response factors of each compound with
1156 respect to inositol.
1157
1158 **Atomic force microscopy and data analysis**. The dry pellets of purified peptidoglycan
1159 from the three strains were dissolved in pure water and further broken by tip sonication

1160 at 2 mA for 30 sec, three cycles. Then 10 µl of the PG suspension was added to standard
1161 AFM substrate made of mica coated with 0.01 % Poly-L-lysine by incubating the sample
1162 during 90 min to achieve good coverage. The sample was further rinsed with water and
1163 dried with Nitrogen flow. The AFM in ambient conditions (i.e. air) was performed using
1164 Tapping mode in a Bruker FastScan Bio machine (Santa Barbara, CA, United States)
1165 with Nunano SCOUT 350 - Silicon AFM probes (spring constant: 42 N/m, Resonance
1166 frequency: 350 kHz). The images were taken using a free amplitude of 10 nm with set
1167 point of 70-80 % of free amplitude (e.g. 7 nm). For AFM high resolution imaging in liquid
1168 the images were acquired in Peak force Tapping mode in imaging buffer made of 10 mM
1169 Tris and 150 mM KCl, pH: 8, with the FastScan Bio machine using Bruker Fastscan-D
1170 AFM probes (spring constant: 0.1 N/m, Resonance frequency: 70 kHz) at the force range
1171 of 1-3 nN peak force set point. The imaging parameters used are as follows; Scan rate:
1172 1 Hz; Scan angle: 0 °; Peak force amplitude: 80-100 nm and with high pixel resolution
1173 (512-880).
1174 The thickness measurements were performed with standard Gwyddion 1D height
1175 distribution tool (selecting an area containing background and a single leaflet of
1176 peptidoglycan). The number of cells analysed varied from n = 23 (for Mtb WT), n = 36
1177 (for *virR*^{mut}) and n = 25 (for *virR*^{mut}-C). The comparisons extracted from this data is
1178 statistically relevant with t test with Welch's correction performed. The analysis of the
1179 high-resolution images obtained in liquid was performed using the semi-automated
1180 custom-made routine from (Pasquina-Lemonche, et al. "Pore AFM", 2024) where the
1181 pore area, later converted in diameter, and the pore number were measured from the 2D
1182 slice of each image containing the maximum number of pores (see **Fig. S8**). The number
1183 of images similar to images shown in **Fig. 5** were n = 8 for all strains, analyzing both pore
1184 size and pore number, the statistical comparisons were also performed using a t test with
1185 Welch's correction.
1186
1187 **Blue native PAGE.** Oligomerization of VirR and Lcp1 was analyzed by Blue native
1188 PAGE (Invitrogen, Waltham, MA, United States). Recombinant VirR and Lcp1 proteins
1189 were prepared in 1xLB Native PAGE including DDM at 0.5% final concentration. After
1190 incubation at 4ºC for 30 min, samples were centrifuged at 20,000 × g for 30 min at 4˚C.
1191 The supernatant was recovered and mixed with G-250 additive following manufacturer
1192 instructions (Invitrogen) and loaded onto a Novex® Bist-Tris 4-16% gradient gel and run
1193 following manufacturer instructions. Gel was first fixed and then stained with Coomassie.
1194
1195 **Liposome flotation assay**. Individual or combined VirR and Lcp1 were prepared at 2
1196 µM in buffer A in a final volume of 50 µl and incubated for 30 min at 37˚C. This volume

1197 was mixed with 100 µl of 60% optiprep (Sigma-Aldrich) to a final concentration of 40%
1198 and overlaid with 100 µl of subsequent optiprep solutions at 35%, 30%, 20% and 10%
1199 (optiprep solutions were prepared in Buffer A). The samples were centrifugated at 70000
1200 rpm for 2 h at 4˚C in an Optima TLX Ultracentrifuge (Beckman Coulter, Indianapolis, IN
1201 United States). Eleven fractions of 50 µl were recovered and examined by dot blot
1202 (performed as previously described). Polyclonal antibodies raised against VirR and Lcp1
1203 were used as primary antibodies. Quantification of dotblots was performed in ImageJ as
1204 previously described (Schirmer et al., 2022). Briefly, integrated densities were calculated
1205 after background subtraction, and referred to wild type values to obtain the relative
1206 integrated intensities.
1207
1208 **Lysozyme and PG and AG susceptibility assays.** *Mtb* WT and *virR*^{mut} strains were
1209 grown in 7H9 media supplemented with ADC and Tween 80 to an OD 540 of 0.2 and
1210 then diluted to an OD540 of 0.1 with 7H9 containing 0 or 50 µgml^{-1} lysozyme (Sigma).
1211 The cultures were incubated with agitation at 37˚C and OD540 was monitored daily.
1212
1213 **Fluorescence microscopy**. The *Mtb* strain bearing the plasmid VirR-pMV261-Venus
1214 was grown in MM to an OD595nm of 0.4. At this stage, cells were harvested, washed
1215 three times in 1 × PBS (pH 7.4), resuspended in 1/3 – 1/6 volume of 4%
1216 paraformaldehyde (PFA) and incubated for 2 h at 37 ˚C. Finally, the cells were washed
1217 twice in 1 × PBS and resuspended in 100–200 µl of PBS. Microscope slides were
1218 covered with 5 µl poly-L-lysine (Sigma) and excess poly-L-lysine was removed away with
1219 distillated water. A 20 – 40 µl aliquot was applied to pre-treated slides, allowed to air dry
1220 and covered with antifade solution (Prolong Gold, Invitrogen) and visualized under the
1221 fluorescence microscope using a 100x oil immersion objective on an Orca 12-ERG digital
1222 CCD camera (Hamamatsu Photonics) mounted on a Nikon E600 microscope.
1223
1224 **FACS analysis for split-GFP experiments.** *M. smegmatis* mc²155 transformed with the
1225 pGMCS derivatives were inoculated in complete 7H9 medium. After overnight incubation
1226 at 37°C, bacteria were collected and analyzed by fluorescence activated cell sorting
1227 using a BD FACS LSRFortessa X20 flow cytometer. Flow cytometry data analysis was
1228 performed using FlowJo software (Version 10; Becton, Dickinson and Company,
1229 Ashland, OR, United States). The gating strategy is displayed in supplementary figure
1230 10 (**Fig. S10**).
1231
1232 **Statistical analysis.** The statistical significance of the difference between experimental
1233 groups was determined by the two-tailed Student's test using PRISM 5.0. P values ≤

than 0.05 were considered significant. Statistical analysis of RNAseq is detailed in the corresponding section of Materials and Methods.

Data Availability. The Datasets produced in this study are available in the following database: RNA-seq data: Gene expression Omnibus, GSE143996 (https://www.ncbi.nlm.nih.gov/geo/query/acc.cgi?acc=GSE143996).

Funding Information. R.P.-R. acknowledges support by MINECO/FEDER EU contracts SAF2016–77433-R, PID2019-110240RB-I00, PID2022-136611OB-I00; and NIH-R01AI162821. CICbioGUNE thanks MINECO for the Severo Ochoa Excellence Accreditation (SEV-2016–0644). L.P-L and J.K.H acknowledges support by the Wellcome Trust (212197/Z/19/Z) which funded part of this research. For the purpose of open access, the authors have applied and will apply a CC BY public copyright license to any Author Accepted Manuscript version arising from this submission. J.S. acknowledges support from the Spanish Ministry of Science and Innovation (MICINN) through grant PID2019-106859GA-I00 and Ramón y Cajal research grant RYC-2017-23560, as well as to the Government of Aragón, Spain, through grant B49-23R (NeuroBioSys). FC lab research is supported by the Swedish Research Council (VR2018-02823 and VR2018-05882), the Laboratory for Molecular Infection Medicine Sweden (MIMS), Umeå University, the Knut and Alice Wallenberg Foundation (KAW) grant KAW2012.0184 and the Kempe Foundation.

Acknowledgments. We are very grateful to Carl Nathan for sharing mutant *Mtb* strains. We thank G. Marcela Rodriguez for sharing the a-IdeR antibody. We thank Heran Darwin for sharing a-cei polyclonal antibody. We thank Emmanuelle Näser (Génotoul TRI-IPBS platform, Toulouse) for helping with flow cytometry. We thank Dr. Luke Alderwick (University of Birmingham) for the donation of the plasmid to recombinantly express Lcp1 protein. We thank M. Gutiérrez for assistance with figures. The authors have no conflict of interest to declare.

References

Amaral L, Kristiansen JE, Abebe LS, Millett W. 1996. Inhibition of the respiration of multi-drug resistant clinical isolates of Mycobacterium tuberculosis by thioridazine: Potential use for initial therapy of freshly diagnosed tuberculosis. *J Antimicrob Chemother* **38**. doi:10.1093/jac/38.6.1049

Ariyachaokun K, Grabowska AD, Gutierrez C, Neyrolles O. 2020. Multi-stress induction of the Mycobacterium tuberculosis MbcTA bactericidal toxin-antitoxin system.

1271 *Toxins (Basel)* **12**. doi:10.3390/toxins12050329
1272 Athman JJ, Sande OJ, Groft SG, Reba SM, Nagy N, Wearsch PA, Richardson ET,
1273 Rojas R, Boom WH, Shukla S, Harding C V. 2017. Mycobacterium tuberculosis
1274 Membrane Vesicles Inhibit T Cell Activation. *J Immunol* **198**:2028–2037.
1275 doi:10.4049/jimmunol.1601199
1276 Athman JJ, Wang Y, McDonald DJ, Boom WH, Harding C V, Wearsch PA. 2015.
1277 Bacterial Membrane Vesicles Mediate the Release of Mycobacterium tuberculosis
1278 Lipoglycans and Lipoproteins from Infected Macrophages. *J Immunol* **195**:1044–
1279 1053. doi:10.4049/jimmunol.1402894
1280 Ballister ER, Samanovic MI, Darwin KH. 2019. Mycobacterium tuberculosis rv2700
1281 contributes to cell envelope integrity and virulence. *J Bacteriol* **201**.
1282 doi:10.1128/JB.00228-19
1283 Bartek IL, Woolhiser LK, Baughn AD, Basaraba RJ, Jacobs WR, Lenaerts AJ, Voskuil
1284 MI. 2014. Mycobacterium tuberculosis Lsr2 is a global transcriptional regulator
1285 required for adaptation to changing oxygen levels and virulence. *MBio* **5**.
1286 doi:10.1128/mBio.01106-14
1287 Bastian M, Heymann S, Jacomy M. 2009. Gephi: An Open Source Software for
1288 Exploring and Manipulating Networks. *Proc Int AAAI Conf Web Soc Media* **3**.
1289 doi:10.1609/icwsm.v3i1.13937
1290 Baumgart M, Schubert K, Bramkamp M, Frunzke J. 2016. Impact of LytRCpsA-Psr
1291 proteins on cell wall biosynthesis in Corynebacterium glutamicum. *J Bacteriol* **198**.
1292 doi:10.1128/JB.00406-16
1293 Beaulieu AM, Rath P, Imhof M, Siddall ME, Roberts J, Schnappinger D, Nathan CF.
1294 2010. Genome-wide screen for Mycobacterium tuberculosis genes that regulate
1295 host immunity. *PLoS One* **5**:e15120. doi:10.1371/journal.pone.0015120
1296 Bera A, Herbert S, Jakob A, Vollmer W, Götz F. 2005. Why are pathogenic
1297 staphylococci so lysozyme resistant? The peptidoglycan O-acetyltransferase OatA
1298 is the major determinant for lysozyme resistance of Staphylococcus aureus. *Mol*
1299 *Microbiol* **55**. doi:10.1111/j.1365-2958.2004.04446.x
1300 Blondel VD, Guillaume J-L, Lambiotte R, Lefebre E. 2008. Fast unfolding of community
1301 hierarchies in large networks. *J Stat Mech Theory Exp* **10**.
1302 Boldrin F, Anso I, Alebouyeh S, Sevilla IA, Geijo M, Garrido JM, Marina A, Mazzabò
1303 LC, Segafreddo G, Guerin ME, Manganelli R, Prados-Rosales R. 2021. The
1304 phosphatidyl-myo-inositol dimannoside acyltransferase pata is essential for
1305 mycobacterium tuberculosis growth in vitro and in vivo. *J Bacteriol* **203**.
1306 doi:10.1128/JB.00439-20
1307 Boot M, van Winden VJC, Sparrius M, van de Weerd R, Speer A, Ummels R, Rustad T,

1308 Sherman DR, Bitter W. 2017. Cell envelope stress in mycobacteria is regulated by
1309 the novel signal transduction ATPase IniR in response to trehalose. *PLoS Genet*
1310 **13**:e1007131. doi:10.1371/journal.pgen.1007131
1311 Boudehen YM, Faucher M, Maréchal X, Miras R, Rech J, Rombouts Y, Sénèque O,
1312 Wallat M, Demange P, Bouet JY, Saurel O, Catty P, Gutierrez C, Neyrolles O.
1313 2022. Mycobacterial resistance to zinc poisoning requires assembly of P-ATPase-
1314 containing membrane metal efflux platforms. *Nat Commun* **13**.
1315 doi:10.1038/s41467-022-32085-7
1316 Brzostek A, Pawelczyk J, Rumijowska-Galewicz A, Dziadek B, Dziadek J. 2009.
1317 Mycobacterium tuberculosis is able to accumulate and utilize cholesterol. *J*
1318 *Bacteriol* **191**. doi:10.1128/JB.00488-09
1319 Cabantous S, Nguyen HB, Pedelacq JD, Koraïchi F, Chaudhary A, Ganguly K, Lockard
1320 MA, Favre G, Terwilliger TC, Waldo GS. 2013. A new protein-protein interaction
1321 sensor based on tripartite split-GFP association. *Sci Rep* **3**.
1322 doi:10.1038/srep02854
1323 Chauhan S, Tyagi JS. 2009. Powerful induction of divergent tgs1-Rv3131 genes in
1324 Mycobacterium tuberculosis is mediated by DevR interaction with a high-affinity
1325 site and an adjacent cryptic low-affinity site. *J Bacteriol* **191**.
1326 doi:10.1128/JB.00310-09
1327 Csardi G, Nepusz T. 2006. The igraph software package for complex network
1328 research. *InterJournal Complex Syst* **Complex Sy**.
1329 De Keijzer J, Mulder A, De Haas PEW, De Ru AH, Heerkens EM, Amaral L, Van
1330 Soolingen D, Van Veelen PA. 2016. Thioridazine alters the cell-envelope
1331 permeability of mycobacterium tuberculosis. *J Proteome Res* **15**.
1332 doi:10.1021/acs.jproteome.5b01037
1333 De Knegt GJ, Ten Kate MT, Van Soolingen D, Aarnoutse R, Boeree MJ, Bakker-
1334 Woudenberg IAJM, De Steenwinkel JEM. 2014. Enhancement of in vitro activity of
1335 tuberculosis drugs by addition of thioridazine is not reflected by improved in vivo
1336 therapeutic efficacy. *Tuberculosis* **94**. doi:10.1016/j.tube.2014.09.002
1337 Dutta NK, Mehra S, Kaushal D. 2010. A Mycobacterium tuberculosis sigma factor
1338 network responds to cell-envelope damage by the promising anti-mycobacterial
1339 thioridazine. *PLoS One* **5**. doi:10.1371/journal.pone.0010069
1340 Ghazaei C. 2018. Mycobacterium tuberculosis and lipids: Insights into molecular
1341 mechanisms from persistence to virulence. *J Res Med Sci*.
1342 doi:10.4103/jrms.JRMS_904_17
1343 Grzegorzewicz AE, de Sousa-d'Auria C, McNeil MR, Huc-Claustre E, Jones V, Petit C,
1344 Angala SK, Zemanova J, Wang Q, Belardinelli JM, Gao Q, Ishizaki Y, Mikusova K,

1345 Brennan PJ, Ronning DR, Chami M, Houssin C, Jackson M. 2016. Assembling of
1346 the Mycobacterium tuberculosis Cell Wall Core. *J Biol Chem* **291**:18867–18879.
1347 doi:10.1074/jbc.M116.739227
1348 Gupta S, Bhagavathula, M Sharma V, Sharma N, Sharma N, Biswas A, Palacios A,
1349 Salgueiro V, Lavín J, Dogra N, Salgame P, Prados-Rosales, R Rodríguez G.
1350 2023. Dynamin-like proteins mediate extracellular vesicle secretion in
1351 Mycobacterium tuberculosis. *EMBO Rep* **24**:e55593.
1352 Harrison J, Lloyd G, Joe M, Lowary TL, Reynolds E, Walters-Morgan H, Bhatt A,
1353 Lovering A, Besra GS, Alderwick LJ. 2016. Lcp1 is a phosphotransferase
1354 responsible for ligating arabinogalactan to peptidoglycan in mycobacterium
1355 tuberculosis. *MBio* **7**. doi:10.1128/mBio.00972-16
1356 Hasenoehrl EJ, Rae Sajorda D, Berney-Meyer L, Johnson S, Tufariello JAM, Fuhrer T,
1357 Cook GM, Jacobs WR, Berney M. 2019. Derailing the aspartate pathway of
1358 Mycobacterium tuberculosis to eradicate persistent infection. *Nat Commun* **10**.
1359 doi:10.1038/s41467-019-12224-3
1360 Honaker RW, Leistikow RL, Bartek IL, Voskui MI. 2009. Unique roles of DosT and
1361 DosS in DosR regulon induction and Mycobacterium tuberculosis dormancy. *Infect*
1362 *Immun* **77**. doi:10.1128/IAI.01449-08
1363 Huber W, Heydebreck A Von, Ultmann HS¨, Poustka A, Vingron M. 2002. Variance
1364 stabilization applied to microarray data calibration and to the quantification of
1365 differential expression. *BIOINFORMATICS*.
1366 Hubscher J, Luthy L, Berger-Bachi B, Stutzmann Meier P. 2008. Phylogenetic
1367 distribution and membrane topology of the LytR-CpsA-Psr protein family. *BMC*
1368 *Genomics* **9**:617. doi:10.1186/1471-2164-9-617
1369 Justen AM, Hodges HL, Kim LM, Sadecki PW, Porfirio S, Ultee E, Black I, Chung GS,
1370 Briegel A, Azadi P, Kiessling LL. 2020. Polysaccharide length affects
1371 mycobacterial cell shape and antibiotic susceptibility. *Sci Adv* **6**.
1372 doi:10.1126/sciadv.aba4015
1373 Kalscheuer R, Palacios A, Anso I, Cifuente J, Anguita J, Jacobs Jr. WR, Guerin ME,
1374 Prados-Rosales R. 2019. The Mycobacterium tuberculosis capsule: a cell
1375 structure with key implications in pathogenesis. *Biochem J* **476**:1995–2016.
1376 doi:10.1042/BCJ20190324
1377 Kawai Y, Marles-Wright J, Cleverley RM, Emmins R, Ishikawa S, Kuwano M, Heinz N,
1378 Bui NK, Hoyland CN, Ogasawara N, Lewis RJ, Vollmer W, Daniel RA, Errington J.
1379 2011. A widespread family of bacterial cell wall assembly proteins. *EMBO J*
1380 **30**:4931–4941. doi:10.1038/emboj.2011.358
1381 Kuru E, Radkov A, Meng X, Egan A, Alvarez L, Dowson A, Booher G, Breukink E,

1382 Roper DI, Cava F, Vollmer W, Brun Y, Vannieuwenhze MS. 2019. Mechanisms of
1383 Incorporation for D -Amino Acid Probes That Target Peptidoglycan Biosynthesis.
1384 *ACS Chem Biol* **14**. doi:10.1021/acschembio.9b00664
1385 Layre E, Sweet L, Hong S, Madigan CA, Desjardins D, Young DC, Cheng TY, Annand
1386 JW, Kim K, Shamputa IC, McConnell MJ, Debono CA, Behar SM, Minnaard AJ,
1387 Murray M, Barry CE, Matsunaga I, Moody DB. 2011. A comparative lipidomics
1388 platform for chemotaxonomic analysis of mycobacterium tuberculosis. *Chem Biol*
1389 **18**. doi:10.1016/j.chembiol.2011.10.013
1390 Lee JE, Moon PG, Lee IK, Baek MC. 2015. Proteomic Analysis of Extracellular
1391 Vesicles Released by Adipocytes of Otsuka Long-Evans Tokushima Fatty
1392 (OLETF) Rats. *Protein J* **34**:220–235. doi:10.1007/s10930-015-9616-z
1393 Lee W, VanderVen BC, Fahey RJ, Russell DG. 2013. Intracellular Mycobacterium
1394 tuberculosis exploits host-derived fatty acids to limit metabolic stress. *J Biol Chem*
1395 **288**:6788–6800. doi:10.1074/jbc.M112.445056
1396 Li C, Wen A, Shen B, Lu J, Huang Y, Chang Y. 2011. FastCloning: A highly simplified,
1397 purification-free, sequence- and ligation-independent PCR cloning method. *BMC*
1398 *Biotechnol* **11**. doi:10.1186/1472-6750-11-92
1399 Liao Y, Smyth GK, Shi W. 2019. The R package Rsubread is easier, faster, cheaper
1400 and better for alignment and quantification of RNA sequencing reads. *Nucleic*
1401 *Acids Res* **47**. doi:10.1093/nar/gkz114
1402 Love MI, Huber W, Anders S. 2014. Moderated estimation of fold change and
1403 dispersion for RNA-seq data with DESeq2. *Genome Biol* **15**. doi:10.1186/s13059-
1404 014-0550-8
1405 Lu R, Schaefer CM, Nesbitt NM, Kuper J, Kisker C, Sampson NS. 2017. Catabolism of
1406 the Cholesterol Side Chain in Mycobacterium tuberculosis Is Controlled by a
1407 Redox-Sensitive Thiol Switch. *ACS Infect Dis* **3**. doi:10.1021/acsinfecdis.7b00072
1408 Maciąg A, Dainese E, Rodriguez GM, Milano A, Provvedi R, Pasca MR, Smith I, Palù
1409 G, Riccardi G, Manganelli R. 2007. Global analysis of the Mycobacterium
1410 tuberculosis Zur (FurB) regulon. *J Bacteriol* **189**. doi:10.1128/JB.01190-06
1411 Majlessi L, Prados-Rosales R, Casadevall A, Brosch R. 2015. Release of
1412 mycobacterial antigens. *Immunol Rev* **264**:25–45. doi:10.1111/imr.12251
1413 Marsollier L, Brodin P, Jackson M, Kordulakova J, Tafelmeyer P, Carbonnelle E, Aubry
1414 J, Milon G, Legras P, Andre JP, Leroy C, Cottin J, Guillou MLJ, Reysset G, Cole
1415 ST, Korduláková J, Tafelmeyer P, Carbonnelle E, Aubry J, Milon G, Legras P,
1416 Saint André JP, Leroy C, Cottin J, Guillou MLJ, Reysset G, Cole ST. 2007. Impact
1417 of Mycobacterium ulcerans biofilm on transmissibility to ecological niches and
1418 Buruli ulcer pathogenesis. *PLoS Pathog* **3**:e62. doi:10.1371/journal.ppat.0030062

1419 McMillan HM, Kuehn MJ. 2021. The extracellular vesicle generation paradox: a
1420 bacterial point of view. *EMBO J* **40**. doi:10.15252/embj.2021108174
1421 Minch KJ, Rustad TR, Peterson EJR, Winkler J, Reiss DJ, Ma S, Hickey M, Brabant W,
1422 Morrison B, Turkarslan S, Mawhinney C, Galagan JE, Price ND, Baliga NS,
1423 Sherman DR. 2015. The DNA-binding network of Mycobacterium tuberculosis. *Nat*
1424 *Commun* **6**. doi:10.1038/ncomms6829
1425 Mohammadzadeh R, Ghazvini K, Farsiani H, Soleimanpour S. 2021. Mycobacterium
1426 tuberculosis extracellular vesicles: exploitation for vaccine technology and
1427 diagnostic methods. *Crit Rev Microbiol*. doi:10.1080/1040841X.2020.1830749
1428 Nagakubo T, Tahara YO, Miyata M, Nomura N, Toyofuku M. 2021. Mycolic acid-
1429 containing bacteria trigger distinct types of membrane vesicles through different
1430 routes. *iScience* **24**. doi:10.1016/j.isci.2020.102015
1431 Nagamani S, Sastry GN. 2021. Mycobacterium tuberculosis cell wall permeability
1432 model generation using chemoinformatics and machine learning approaches. *ACS*
1433 *Omega* **6**. doi:10.1021/acsomega.1c01865
1434 Nečas D, Klapetek P. 2012. Gwyddion: An open-source software for SPM data
1435 analysis. *Cent Eur J Phys*. doi:10.2478/s11534-011-0096-2
1436 Oba S, Sato MA, Takemasa I, Monden M, Matsubara KI, Ishii S. 2003. A Bayesian
1437 missing value estimation method for gene expression profile data. *Bioinformatics*
1438 **19**:2088–2096. doi:10.1093/bioinformatics/btg287
1439 Pandey R, Rodriguez GM. 2014. IdeR is required for iron homeostasis and virulence in
1440 Mycobacterium tuberculosis. *Mol Microbiol* **91**. doi:10.1111/mmi.12441
1441 Park HD, Guinn KM, Harrell MI, Liao R, Voskuil MI, Tompa M, Schoolnik GK, Sherman
1442 DR. 2003. Rv3133c/dosR is a transcription factor that mediates the hypoxic
1443 response of Mycobacterium tuberculosis. *Mol Microbiol* **48**. doi:10.1046/j.1365-
1444 2958.2003.03474.x
1445 Pasquina-Lemonche L, Burns J, Turner RD, Kumar S, Tank R, Mullin N, Wilson JS,
1446 Chakrabarti B, Bullough PA, Foster SJ, Hobbs JK. 2020. The architecture of the
1447 Gram-positive bacterial cell wall. *Nature* **582**. doi:10.1038/s41586-020-2236-6
1448 Pawełczyk J, Brzostek A, Minias A, Płociński P, Rumijowska-Galewicz A, Strapagiel D,
1449 Zakrzewska-Czerwińska J, Dziadek J. 2021. Cholesterol-dependent transcriptome
1450 remodeling reveals new insight into the contribution of cholesterol to
1451 Mycobacterium tuberculosis pathogenesis. *Sci Rep* **11**. doi:10.1038/s41598-021-
1452 91812-0
1453 Peterson EJ, Bailo R, Rothchild AC, Arrieta-Ortiz ML, Kaur A, Pan M, Mai D, Abidi AA,
1454 Cooper C, Aderem A, Bhatt A, Baliga NS. 2019. Path-seq identifies an essential
1455 mycolate remodeling program for mycobacterial host adaptation. *Mol Syst Biol* **15**.

1456 doi:10.15252/msb.20188584
1457 Peterson EJR, Brooks AN, Reiss DJ, Kaur A, Do J, Pan M, Wu WJ, Morrison R,
1458 Srinivas V, Carter W, Arrieta-Ortiz ML, Ruiz RA, Bhatt A, Baliga NS. 2023. MtrA
1459 modulates Mycobacterium tuberculosis cell division in host microenvironments to
1460 mediate intrinsic resistance and drug tolerance. *Cell Rep* **42**.
1461 doi:10.1016/j.celrep.2023.112875
1462 Prados-Rosales R, Baena A, Martinez LR, Luque-Garcia J, Kalscheuer R,
1463 Veeraraghavan U, Camara C, Nosanchuk JD, Besra GS, Chen B, Jimenez J,
1464 Glatman-Freedman A, Jacobs Jr. WR, Porcelli SA, Casadevall A, Jacobs WR,
1465 Porcelli SA, Casadevall A. 2011. Mycobacteria release active membrane vesicles
1466 that modulate immune responses in a TLR2-dependent manner in mice. *J Clin*
1467 *Invest* **121**:1471–1483. doi:10.1172/JCI44261
1468 Prados-Rosales R, Carreno L, Cheng T, Blanc C, Weinrick B, Malek A, Lowary TL,
1469 Baena A, Joe M, Bai Y, Kalscheuer R, Batista-Gonzalez A, Saavedra NA,
1470 Sampedro L, Tomas J, Anguita J, Hung SC, Tripathi A, Xu J, Glatman-Freedman
1471 A, Jacobs Jr. WR, Chan J, Porcelli SA, Achkar JM, Casadevall A. 2017.
1472 Enhanced control of Mycobacterium tuberculosis extrapulmonary dissemination in
1473 mice by an arabinomannan-protein conjugate vaccine. *PLoS Pathog*
1474 **13**:e1006250. doi:10.1371/journal.ppat.1006250
1475 Prados-Rosales R, Carreño LJ, Batista-Gonzalez A, Baena A, Venkataswamy MM, Xu
1476 J, Yu X, Wallstrom G, Mitchell Magee D, LaBaer J, Achkar JM, Jacobs WR, Chan
1477 J, Porcelli SA, Casadevall A. 2014a. Mycobacterial membrane vesicles
1478 administered systemically in mice induce a protective immune response to surface
1479 compartments of mycobacterium tuberculosis. *MBio* **5**:e01921-14.
1480 doi:10.1128/mBio.01921-14
1481 Prados-Rosales R, Weinrick BC, Pique DG, Jacobs Jr. WR, Casadevall A, Rodriguez
1482 GM, Piqué DG, Jacobs WR, Casadevall A, Rodriguez GM. 2014b. Role for
1483 Mycobacterium tuberculosis membrane vesicles in iron acquisition. *J Bacteriol*
1484 **196**:1250–1256. doi:10.1128/JB.01090-13
1485 Prasad TSK, Verma R, Kumar S, Nirujogi RS, Sathe GJ, Madugundu AK, Sharma J,
1486 Puttamallesh VN, Ganjiwale A, Myneedu VP, Chatterjee A, Pandey A, Harsha HC,
1487 Narayana J. 2013. Proteomic analysis of purified protein derivative of
1488 mycobacterium tuberculosis. *Clin Proteomics* **10**. doi:10.1186/1559-0275-10-8
1489 Rath P, Huang C, Wang T, Wang T, Li H, Prados-Rosales R, Elemento O, Casadevall
1490 A, Nathan CF. 2013. Genetic regulation of vesiculogenesis and
1491 immunomodulation in Mycobacterium tuberculosis. *Proc Natl Acad Sci U S A*
1492 **110**:E4790-7. doi:10.1073/pnas.1320118110

1493 Ritchie ME, Phipson B, Wu D, Hu Y, Law CW, Shi W, Smyth GK. 2015. Limma powers
1494 differential expression analyses for RNA-sequencing and microarray studies.
1495 *Nucleic Acids Res* **43**:e47. doi:10.1093/nar/gkv007
1496 Rock JM, Hopkins FF, Chavez A, Diallo M, Chase MR, Gerrick ER, Pritchard JR,
1497 Church GM, Rubin EJ, Sassetti CM, Schnappinger D, Fortune SM. 2017.
1498 Programmable transcriptional repression in mycobacteria using an orthogonal
1499 CRISPR interference platform. *Nat Microbiol* **2**:16274.
1500 doi:10.1038/nmicrobiol.2016.274
1501 Sani M, Houben ENG, Geurtsen J, Pierson J, De Punder K, Van Zon M, Wever B,
1502 Piersma SR, Jiménez CR, Daffé M, Appelmelk BJ, Bitter W, Van Wel N Der,
1503 Peters PJ. 2010. Direct visualization by Cryo-EM of the mycobacterial capsular
1504 layer: A labile structure containing ESX-1-secreted proteins. *PLoS Pathog* **6**.
1505 doi:10.1371/journal.ppat.1000794
1506 Sartain MJ, Dick DL, Rithner CD, Crick DC, Belisle JT. 2011. Lipidomic analyses of
1507 Mycobacterium tuberculosis based on accurate mass measurements and the
1508 novel “Mtb LipidDB.” *J Lipid Res* **52**. doi:10.1194/jlr.M010363
1509 Schirmer S, Rauh L, Alebouyeh S, Delgado-Velandia M, Salgueiro VC, Lerma L,
1510 Serrano-Mestre JL, Azkargorta M, Elortza F, Lavín JL, García MJ, Tórtola-
1511 Fernández MT, Gola S, Prados-Rosales R. 2022. Immunogenicity of
1512 Mycobacterial Extracellular Vesicles Isolated From Host-Related Conditions
1513 Informs About Tuberculosis Disease Status. *Front Microbiol* **13**:907296.
1514 doi:10.3389/fmicb.2022.907296
1515 Schnappinger D, Ehrt S, Voskuil MI, Liu Y, Mangan JA, Monahan IM, Dolganov G,
1516 Efron B, Butcher PD, Nathan C, Schoolnik GK. 2003. Transcriptional adaptation of
1517 Mycobacterium tuberculosis within macrophages: Insights into the phagosomal
1518 environment. *J Exp Med* **198**:693–704. doi:10.1084/jem.20030846
1519 Soto-Ramirez MD, Aguilar-Ayala DA, Garcia-Morales L, Rodriguez-Peredo SM,
1520 Badillo-Lopez C, Rios-Muñiz DE, Meza-Segura MA, Rivera-Morales GY, Leon-
1521 Solis L, Cerna-Cortes JF, Rivera-Gutierrez S, Helguera-Repetto AC, Gonzalez-y-
1522 Merchand JA. 2017. Cholesterol plays a larger role during Mycobacterium
1523 tuberculosis in vitro dormancy and reactivation than previously suspected.
1524 *Tuberculosis* **103**. doi:10.1016/j.tube.2016.12.004
1525 Storey JD, Bass AJ, Dabney A, Robinson D. 2023. qvalue: Q-value estimation for false
1526 discovery rate control.
1527 Stupar M, Tan L, Kerr ED, De Voss CJ, Forde BM, Schulz BL, West NP. 2024. TcrXY
1528 is an acid-sensing two-component transcriptional regulator of Mycobacterium
1529 tuberculosis required for persistent infection. *Nat Commun* **15**.

1530 doi:10.1038/s41467-024-45343-7
1531 Trapnell C, Pachter L, Salzberg SL. 2009. TopHat: Discovering splice junctions with
1532 RNA-Seq. *Bioinformatics* **25**. doi:10.1093/bioinformatics/btp120
1533 Tsuruoka T, Tamura A, Miyata A, Takei T, Inouye S, Matsuhashi M. 1985. Second
1534 Lytic Target of Beta-Lactam Compounds That Have A Terminal d-Amino Acid
1535 Residue. *Eur J Biochem* **151**. doi:10.1111/j.1432-1033.1985.tb09090.x
1536 Vilchèze C, Jacobs WR. 2007. Isolation and analysis of Mycobacterium tuberculosis
1537 mycolic acids. *Curr Protoc Microbiol* **Chapter 10**.
1538 doi:10.1002/9780471729259.mc10a03s05
1539 Wang M, Guo X, Yang X, Zhang B, Ren J, Liu A, Ran Y, Yan B, Chen F, Guddat LW,
1540 Hu J, Li J, Rao Z. 2019. Mycobacterial dynamin-like protein IniA mediates
1541 membrane fission. *Nat Commun* **10**. doi:10.1038/s41467-019-11860-z
1542 White DW, Elliott SR, Odean E, Bemis LT, Tischler AD. 2018. Mycobacterium
1543 tuberculosis Pst/SenX3-RegX3 Regulates Membrane Vesicle Production
1544 Independently of ESX-5 Activity. *MBio* **9**. doi:10.1128/mBio.00778-18
1545 Williams EP, Lee JH, Bishai WR, Colantuoni C, Karakousis PC. 2007. Mycobacterium
1546 tuberculosis SigF regulates genes encoding cell wall-associated proteins and
1547 directly regulates the transcriptional regulatory gene phoY1. *J Bacteriol* **189**.
1548 doi:10.1128/JB.00201-07
1549 Wiśniewski JR, Zougman A, Nagaraj N, Mann M. 2009. Universal sample preparation
1550 method for proteome analysis. *Nat Methods* **6**. doi:10.1038/nmeth.1322
1551 Zhang X, Smits AH, Tilburg GBA Van, Ovaa H, Huber W, Vermeulen M. 2018.
1552 Proteome-wide identification of ubiquitin interactions using UbIA-MS. *Nat Protoc*
1553 **13**:530–550. doi:10.1038/nprot.2017.147
1554 Ziegenbalg A, Prados-Rosales R, Jenny-Avital ER, Kim RS, Casadevall A, Achkar JM.
1555 2013. Immunogenicity of mycobacterial vesicles in humans: identification of a new
1556 tuberculosis antibody biomarker. *Tuberc* **93**:448–455.
1557 doi:10.1016/j.tube.2013.03.001
1558 Zuber B, Haenni M, Ribeiro T, Minnig K, Lopes F, Moreillon P, Dubochet J. 2006.
1559 Granular layer in the periplasmic space of gram-positive bacteria and fine
1560 structures of Enterococcus gallinarum and Streptococcus gordonii septa revealed
1561 by cryo-electron microscopy of vitreous sections. *J Bacteriol* **188**.
1562 doi:10.1128/JB.00391-06
1563
1564
1565
1566

1567 **Figure Legends**

1568

1569 **Figure 1. Ultrastructural changes in the cell envelope of *virR*-deficient mutant**
1570 **associated with increased vesiculation.** (**A**) Cryo-electron micrographs of indicated
1571 *Mtb* strains grown in high iron MM. Closed line rectangles were used to calculate grey
1572 value profiles of cell envelopes using ImageJ. The dashed line insets within the main
1573 micrograph were magnified to show a detailed view of the cell surface. Scale bars are
1574 100 nm in main micrographs and 50 nm in the insets. (**B**) Density profiles based on grey
1575 values of the cross sections marked by solid line rectangles in A. (**C**) Mean values and
1576 standard errors of distances in nm between main cell envelope layers measured in A
1577 and C. *P < 0.05 after applying a Tukey´s multiple comparison test. The number of cells
1578 analyzed varied from n = 20 (WT), n = 15 ($virR^{mut}$) and n = 23 ($virR^{mut}$-C). CM, cytoplasmic
1579 membrane; OM, outer membrane; L1, layer 1; L2, layer 2.

1580

1581 **Figure 2. Enhanced permeability and vesiculation are linked in the absence of**
1582 **LytR_C solo domain proteins in *Mtb*. (A)** Uptake of ethidium bromide (EthBr) in the
1583 indicated strains, as measured by fluorescence at 590 nm for 65 min. Data are mean and
1584 standard deviation of three biological replicates. **(B)** Sensitivity of the indicated strains to
1585 different concentrations of vancomycin as measured by monitoring optical density at 580
1586 nm (OD580) after 7 days. Data are mean and standard deviations of three biological
1587 replicated. Errors bars not shown are smaller than symbols. **(C)** Time course of the
1588 incorporation of FDAAs on the indicated strains in 7H9 as measured by fluorescence.
1589 Cells were labeled with HADA for 48 h, washed in 7H9 medium and labeled with FDL for
1590 5 h. Ten, cell were fixed and imaged under a fluorescence microscope. Representative
1591 images of WT, $virR^{mut}$ and $virR^{mut}$-Comp strains in 7H9. Data are mean and standard
1592 deviations of three biological replicates. *** means P<0.001 and **** means P<0.0001
1593 after applying a One-way ANOVA analysis. The arrow indicates the time at which images
1594 were taken. Errors bar not shown are smaller than symbols. **(D)** immunoblot analysis of
1595 cell lysates of two independent conditional mutants (c1 and c2) for *virR* and *cei* for the
1596 presence of VirR and Cei proteins in cultures incubated with and without
1597 anhydrotetracycline (ATc). **(E)** Nanoparticle tracking analysis (NTA) of EV preparations
1598 derived from *virR* and *cei* conditional mutants (c2 (*virR*) and c1 (*cei*)) obtained from
1599 cultures with and without ATc showing number of particles per cm^3 determined by Zeta
1600 View NTA in three independent EV preparations. Data are presented as mean ± SEM.

1601

1602 **Figure 3. Transcriptional profiling of $virR^{mut}$ showcases systemic alterations in cell**
1603 **wall architecture and metabolism. (A)** Experiment design for RNA-seq analyses. RNA

1604 was extracted from whole cell extracts from 4 replicate cultures of each strain (WT,
1605 *virR*^{mut}, and *virR*^{mut} -Comp), and sequenced. **(B)** PCA plot of the transcriptomics data.
1606 The loadings from the two first principal components are plotted. **(C)** Number of
1607 differentially expressed genes between *virR*^{mut} and either WT (left) or *virR*^{mut}-Comp
1608 (right). **(D)** Enrichment profiles between sets of genes found up and down-regulated for
1609 the contrasts *virR*^{mut} vs WT and *virR*^{mut} vs *virR*^{mut}-Comp. While genes that are
1610 differentially expressed in the same direction in both contrasts are mutually enriched,
1611 genes whose differential expression goes in different directions in both comparisons are
1612 mutually depleted (two-sided Fisher exact test $p<0.05$ in all four cases). **(E)** Gene
1613 Ontology (GO) enrichments of genes that are 1) simultaneously downregulated in *virR*^{mut}
1614 with respect to both WT and v *virR*^{mut}-Comp (left) and 2) simultaneously upregulated
1615 (right). GO terms selected for testing included biological process and cell compartment
1616 labels containing N > 10 genes, between levels 4-6 of the ontology tree. In this
1617 representation, each node in the networks represents a significantly enriched term (terms
1618 selected for visualization with FDR=10% and enrichment odds-ratio>2), nodes' size is
1619 proportional to the enrichment significance, and links between terms are added wherever
1620 the sets of genes contributing to the enrichments in a connected pair show an
1621 intersection larger than 50% of the smallest of the gene sets involved in the pair (see
1622 Methods for further details, and supplementary file S2 for an extended list of all the
1623 enrichments found).

1624 **Figure 4. VirR-dependent genes intersect the regulons of key transcriptional**
1625 **regulators of the responses to stress, dormancy, and cell wall remodeling. (A)**
1626 Transcription factors controlling regulons significantly enriched among genes that are 1)
1627 simultaneously downregulated in *virR*^{mut} with respect to both WT and *virR*^{mut} -Comp
1628 (bottom, 9 TFs) and 2) simultaneously upregulated (top, 1 TF). **(B)** Differential expression
1629 patterns for enriched TFs whose expression is VirR-dependent. **(C)** Regulatory
1630 subnetwork including the genes under transcriptional control of the enriched TFs
1631 highlighted in figure 4A that were found to be VirR-dependent. In this visualization, color
1632 captures the logFC for the contrast *virR*^{mut} -WT, and the size of its FDR.

1633

1634 **Figure 5. Cell permeability is a major driver of vesicle production in *Mtb*. (A)** Time
1635 course of the uptake of ethidium bromide (EthBr) by *Mtb* grown in the indicated
1636 conditions, as measured by fluorescence at 590=nm for 65 min. Data are mean and
1637 standard deviation of three biological replicates. **(B)** Dot-blot analysis of released EVs in
1638 supernatants from *Mtb* cultures submitted to the indicated conditions. The loading
1639 volume was normalized according to CFUs. The graph below represents the
1640 quantification of the dotblot using ImageJ. The integrated cell density was normalized to

1641 WT values. Data are mean and standard errors from the three biological replicates; ****
1642 denotes P<0.0001, *** denotes P=0.0028 after applying a Tuke's multiple comparison
1643 test. **(C)** Enrichment odds ratios for Fisher exact tests comparing sets of genes up, and
1644 down regulated, respectively, in 1) cholesterol-supplemented medium vs. glucose-
1645 supplemented medium (Pawełczyk et al., 2021), GEO accession GSE175812); and 2)
1646 *virR*^{mut} vs WT as well as *virR*^{mut} vs *virR*^{mut}-Comp. **(D)** Euler diagram showing the
1647 intersection between A) genes upregulated by cholesterol, B) genes down-regulated in
1648 *virR*^{mut}, and C) the DevR regulon. **(E)** Expression patterns in response to TRZ (1h) and
1649 in *virR*^{mut} for genes involved in metal signaling, metabolism and homeostasis.
1650
1651 **Figure 6. VrR regulates the protein content of EVs in Mtb. (A).** Experiment design for
1652 proteomics analyses. label-free mass spectrometry data was retrieved for replicates of
1653 H37RV (WT), *virR*^{mut} and *virR*^{mut}-Comp. For each strain, data corresponding to proteins
1654 extracted from either whole-cell extracts (WC) and EVs was produced, totaling 12
1655 samples (2 strains times 2 cell compartments times 3 replicates). **(B)** PCA plot of the
1656 proteomics data. The loadings from the two first principal components, adding up to
1657 50.5% of variance explained, are plotted. **(C)** Expression patterns of VirR in the
1658 proteomics dataset across cell compartments and strains. As expected, while *virR*^{mut}
1659 shows significantly lower levels of VirR protein, the complemented strain does not just
1660 restore WT levels of expression, but leads to a strong overexpression of VirR, both in
1661 the lysates and the EVs, **(D)** Bar plots of differentially expressed proteins found between
1662 strains in EVs (up: *virR*^{mut} vs WT; down *virR*^{mut} vs *virR*^{mut}-Comp at 5% FDR). **(E)**
1663 Enrichment profiles between sets of proteins found up and down-regulated for the
1664 contrasts *virR*^{mut} vs WT and *virR*^{mut} vs *virR*^{mut}-Comp. **(F)** Gene Ontology enrichments of
1665 the downregulated proteins in the VirR mutant strain (left) and the upregulated ones
1666 (Right), at the EV location. GO terms selected for testing included biological process and
1667 cell compartment labels containing N > 3 genes, between levels 4-6 of the ontology tree.
1668 As in **figure 3E**, terms selected for visualization with FDR=10% and enrichment odds-
1669 ratio>2, nodes' size is proportional to the enrichment significance, and links between
1670 terms are added wherever the sets of proteins contributing to the enrichments in a
1671 connected pair shows an intersection larger than 50% of the smallest of the gene sets
1672 involved in the pair (see Methods for further details, and supplementary file S5 for an
1673 extended list of all the enrichments found). **(G)** Expression patterns of bacterioferritin
1674 proteins in the EVs of WT and *virR*^{mut}. **(H)** Expression patterns of proteins contributing to
1675 enrichments of terms related to mycolic acids biosynthesis. **(I)** Bottom left:
1676 Concentrations of key metabolites in the propionyl-coA detoxification routes. Right:
1677 Metabolic pathway of the propionyl-coA detoxification route through the methyl-malonyl

1678 route, along with the differential expression statistics between the WT and *virR*^{mut} strains
1679 observed at transcriptomic and proteomic levels for the main enzymes involved. The
1680 framed plot represents the quantification of selected metabolites by mass spectrometry.
1681
1682 **Figure 7. Lipidomic analysis of cell envelope and EVs from *virR*^{mut}. (A)** Comparative
1683 total lipid analysis of the indicated strains by nano-LC-MS. Lipid species with an
1684 abundance higher than 0.5% are shown. Data indicates mean and standard error from
1685 three biological replicates. **(B)** Analysis of polar lipids of the indicated strains by
1686 bidimensional (2D)-layer chromatography (TLC) (2D-TLC). Phosphatidyl-myo-inositol
1687 dimannosides (Ac_1PIM_2 and Ac_2PIM_2, respectively); phosphatidyl-myo-inositol
1688 hexamannosides (Ac_xPIM_6); phosphatidylethanolamine (PE); diphosphatidylglycerol
1689 (DPG). Phospholipid (P). **(C)** Analysis of mycolic acid species in the indicated strains by
1690 TLC. **(D)** Analysis of PIDMs and TAGs by TLC. **(E)** Analysis of apolar lipids of the
1691 indicated strains by TLC. Diacylglycerol (DAG); free fatty acid (FF); free mycolic acid
1692 (FMA). **(F)** Analysis of apolar lipids of MEVs isolated from the indicated strains.
1693 Triacylglycerols (TAGs); phthiocerol dimycocerosates (PDIMs) **(G)** Analysis of polar
1694 lipids of MEVs isolated from the indicated strains. Phosphatidyl-myo-inositol
1695 dimannosides (Ac_1PIM_2 and Ac_2PIM_2, respectively); phosphatidyl-myo-inositol
1696 hexamannosides (Ac_xPIM_6); diphosphatidylglycerol (DPG).
1697
1698 **Figure 8. Chemical and nanometric analysis of isolated cell walls shows higher**
1699 **amounts of PG in the absence of VirR. (A)** Glycosyl composition analysis of isolated
1700 cell walls from the indicated strains. Acid hydrolysis prior to GC-MS analysis of isolated
1701 cell walls was performed to determine the total amounts of galactose (G), arabinose (A),
1702 rhamnose (R), and N-acetylglucosamine (NAGc). The ratio between different sugars is
1703 shown to indicate: (i) the relative levels of arabinogalactan (A/G); (ii) the length of the AG
1704 polysaccharide chain (G/R); (iii) the amount of PG (NAGc/Rham). Individual
1705 measurements are shown from three biological replicates. Data are mean and standard
1706 errors. **P < 0.01 after applying a Tukey´s multiple comparison test. **(B)** Quantification
1707 of diaminopimelic acid (DAP) on isolated cell walls from the indicated strains. Data are
1708 mean and standard errors from three biological replicates; **** denotes P<0.0001, *
1709 denotes P=0.0119 after applying a Tukey´s multiple comparison test. **(C)** Atomic force
1710 microscopy high resolution images taken in liquid from the external surface of purified
1711 peptidoglycan from different samples, left to right: WT, *virR*^{mut}, *virR*^{mut}*-C*, the structure of
1712 external peptidoglycan layer shows a mesh with pores of different sizes, **(D)** Graph
1713 showing the pore diameter from n = 8 AFM images similar to **(C)** (each point represent
1714 an image) of different samples; black triangles: WT, blue circles: *virR*^{mut}, red squares:

1715 *virR*^{mut}*-C*. The pore diameter was calculated from the binary slice from each image
1716 containing the greatest number of pores, according to (Pasquina-Lemonche, 2024). **(E)**
1717 The number of pores per surface area from different samples; white triangles: WT, red
1718 circles: *virR*^{mut}, blue squares: *virR*^{mut}-C, this was calculated from the slice containing the
1719 maximum number of pores where the pore size was analyzed, following the method from
1720 (Pasquina-Lemonche, 2024). **(F)** Graph showing the peptidoglycan thickness manually
1721 measured using the 1D statistic tools from the open-source program Gwyddion (Nečas
1722 and Klapetek, 2012) from AFM images in air containing several fragments of cell wall,
1723 each point represents a different peptidoglycan fragment from a different cell. There were
1724 three samples analyzed: black WT n=23 peptidoglycan fragments, blue *virR*^{mut} n=36 and
1725 red *virR*^{mut}-C n=25. Statistics: D) Using a two-tailed t test with Welch's correction the
1726 statistical comparison are: (***) pWT- *virR*^{mut} = 4.1 10^{-4} with t = 6.1, df = 7.5, (**) p *virR*^{mut}
1727 - *virR*^{mut}-C = 0.007 with t = 3.2, df = 13.2, E) Using a two-tailed t test with Welch's
1728 correction the statistical comparison are: (****) pWT- *virR*^{mut} = 6.6 10-10 with t = 16.3,
1729 df = 12.7, (**) p *virR*^{mut} - *virR*^{mut} -C = 0.01 with t = 3.0, df = 13.2., F) Using a two-tailed t
1730 test with Welch's correction the statistical comparison are: (****) pWT- *virR*^{mut} = 2.8 10-
1731 18 with t = 17.8, df = 32.3, (****) *virR*^{mut} - *virR*^{mut} -C = 3.9 10-17 with t = 16.4, df = 31.8.
1732 **(G)** List of muropeptides identified in the cell walls of Mtb. Features including retention
1733 time (RT), observed and expected mass as well as the best match for each peak are
1734 shown. Those deacetylated muropeptides are indicated in red. **(H)** Relative abundance
1735 of deacetylated muropeptides in the indicated strains.
1736
1737 **Figure 9. VirR interacts with Lcp1. (A)** Blue-native PAGE analysis of recombinant VirR
1738 and Lcp1. The molecular mass of markers in kDa are indicated on the left side of the gel.
1739 The size of the multimers of VirR and Lcp1 are indicated on the left side of the gel. **(B)**
1740 *Upper panel*. Representative image of a flotation assay of recombinant VirR alone or in
1741 combination with Lcp1 performed on an idioxanol density gradient. The presence of VirR
1742 was detected in each fraction by dot-blot using murine polyclonal antibodies raised
1743 against VirR. Numbers indicate collected fractions from top (1) to bottom (11). *Lower*
1744 *panel*. Quantification of the dot-blot by measuring the pixel intensity of the dots using
1745 ImageJ. Data are mean and standard error of three independent experiments. **(C)**
1746 Bipartite split-GFP experiment using *M. smegmatis* D2 expressing plasmids depicted in
1747 (**Fig S11A**), including $CtpC_{Nterm}$, VirR, VirRsol (Δ1-41), Rv3484, Rv3267 (Lcp1), Rv0822,
1748 $Rv3484_{LytR_C}$, $Rv3267_{LytR_C}$ and $Rv0822_{LytR_C}$. Bacteria were grown in complete 7H9 and
1749 fluorescence was recorded by FACS. Pooled data obtained from four to six independent
1750 cultures of each strain are shown. Statistical analysis was performed using non-

1751 parametric two-sided Mann-Whitney test. ns: not significant. * and ** refer to p-values
1752 <0.05 or 0.01, respectively.
1753
1754 **Supplementary Tables**
1755
1756 **Supplementary Table S1.** Plasmids and primers used in this study.

Construction / DNA fragment used	Template	Primers	Sequence 5'-3'
pGMCS-P1-*virR*-Lk2-GFP11-*ctpC*(1-85)-Lk15-GFP(1-10)			
P1	pGMCS-TetR-P1-*pacL1*$_{Flag}$- P$_{pacL1}$-*ctpC*$_{His}$ (Boudehen *et al*. 2022)	Inf-B2-P1-Fw	CAAAGTGGAGCGATACTCGACATCGGATCGTCGGCACCGTCAC
		Inf-P1-Left	GAAATGATGTATGCCGTGCTGGTC
pGMCS backbone	pGMCS-P$_{pacL}$-*pacL1*-Lk2-GFP11-*ctpC*(1-85)-Lk15-GFP(1-10) (Boudehen *et al*. 2022)	ctpC-B2-Left	GTCGAGTATCGCTCCACTTTG
		Rv3269-P1-Fus-Fw	CAGCACGGCATACATCATTTCGGAAGAAAGGTACAGGCAATGG
pGMCS-P1-*virR*-Lk2-GFP11-*ctpC*(1-85)-Lk15-GFP(1-10)			
virR	*M. tuberculosis* H37Rv chromosomal DNA	If-AmL1-VirR	AAGGTACAGGCAATGgtgctggttacagtgggctcg
		If-Lk2-VirR-Rv	ACCGGATCCTTCCAGgccggtcaccacgacgatg
pGMCS backbone	pGMCS-P1-*pacL1*-Lk2-GFP11-*ctpC*(1-85)-Lk15-GFP(1-10)	Lk2-Right	CTGGAAGGATCCGGTGGCGG
		pGMC 3269 Am Left	CATTGCCTGTACCTTTCTTCC
pGMCS-P1-*virRsol*-Lk2-GFP11-*ctpC*(1-85)-Lk15-GFP(1-10)			
virRsol	*M. tuberculosis* H37Rv chromosomal DNA	If-AmL1-VirRsol	AAGGTACAGGCAATGctgggttcgtctccgaactccg
		If-Lk2-VirR-Rv	ACCGGATCCTTCCAGgccggtcaccacgacgatg
pGMCS backbone	pGMCS-P1-*pacL1*-Lk2-GFP11-*ctpC*(1-85)-Lk15-GFP(1-10)	Lk2-Right	CTGGAAGGATCCGGTGGCGG
		pGMC 3269 Am Left	CATTGCCTGTACCTTTCTTCC
pGMCS-P1-*virR*-Lk2-GFP11-*virR*-Lk15-GFP(1-10)			
virR	*M. tuberculosis* H37Rv chromosomal DNA	If-AmMBD-VirR	GAGCGCCTCGCCATGgtgctggttacagtgggctcg
		If-L15-VirR-Rv	AGACAGCCCTGGACCgccggtcaccacgacgatg
pGMCS backbone	pGMCS-P1-*virR*-Lk2-GFP11-*ctpC*(1-85)-Lk15-GFP(1-10)	Flex15-Right	GGTCCAGGGCTGTCTGGCC
		ctpC-Am-left2	CATGGCGAGGCGCTCAAG
pGMCS-P1-*virRsol*-Lk2-GFP11-*virRsol*-Lk15-GFP(1-10)			
virRsol	*M. tuberculosis* H37Rv chromosomal DNA	If-AmMBD-VirRsol	GAGCGCCTCGCCATGctgggttcgtctccgaactccg
		If-L15-VirR-Rv	AGACAGCCCTGGACCgccggtcaccacgacgatg
pGMCS backbone	pGMCS-P1-*virRsol*-Lk2-GFP11-*ctpC*(1-85)-Lk15-GFP(1-10)	Flex15-Right	GGTCCAGGGCTGTCTGGCC
		ctpC-Am-left2	CATGGCGAGGCGCTCAAG
pGMCS-P1-*virRsol*-Lk2-GFP11-*rv0822c*(LytR_C)-Lk15-GFP(1-10)			
Rv0822c(LytR_C)	*M. tuberculosis* H37Rv chromosomal DNA	If-AmMBD-0822cD	GAGCGCCTCGCCATGgagattcagcaccagcaggttacgacg
		If-L15-0822cD-Rv	AGACAGCCCTGGACCgcggcttatctgcacgctgacg
pGMCS backbone	pGMCS-P1-*virRsol*-Lk2-GFP11-*ctpC*(1-85)-Lk15-GFP(1-10)	Flex15-Right	GGTCCAGGGCTGTCTGGCC
		ctpC-Am-left2	CATGGCGAGGCGCTCAAG
pGMCS-P1-*virRsol*-Lk2-GFP11-*rv3267*(LytR_C)-Lk15-GFP(1-10)			

Rv3267(LytR_C)	*M. tuberculosis* H37Rv chromosomal DNA	If-AmMBD-3267D	GAGCGCCTCGCCATGcccgccaagaccacggcc
		If-L15-3267D-Rv	AGACAGCCCTGGACCcagcccggagcccggac
pGMCS backbone	pGMCS-P1-*virRsol*-Lk2-GFP11-*ctpC*(1-85)-Lk15-GFP(1-10)	Flex15-Right	GGTCCAGGGCTGTCTGGCC
		ctpC-Am-left2	CATGGCGAGGCGCTCAAG
pGMCS-P1-*virRsol*-Lk2-GFP11-*rv3484*(LytR_C)-Lk15-GFP(1-10)			
Rv3484(LytR_C)	*M. tuberculosis* H37Rv chromosomal DNA	If-AmMBD-3484D	GAGCGCCTCGCCATGgcggccgccaaacctaacc
		If-L15-3484D-Rv	AGACAGCCCTGGACCggtatccaccgtcacacggatg
pGMCS backbone	pGMCS-P1-*virRsol*-Lk2-GFP11-*ctpC*(1-85)-Lk15-GFP(1-10)	Flex15-Right	GGTCCAGGGCTGTCTGGCC
		ctpC-Am-left2	CATGGCGAGGCGCTCAAG
pGMCS-P1-*virRsol*-Lk2-GFP11-*rv0822c*(Cterm)-Lk15-GFP(1-10)			
Rv0822c(Cterm)	*M. tuberculosis* H37Rv chromosomal DNA	If-AmMBD-0822cD	GAGCGCCTCGCCATGgagattcagcaccagcaggttacgacg
		If-L15-0822c-Rv2	AGACAGCCCTGGACCctcgcaggtggtgtcggcg
pGMCS backbone	pGMCS-P1-*virRsol*-Lk2-GFP11-*ctpC*(1-85)-Lk15-GFP(1-10)	Flex15-Right	GGTCCAGGGCTGTCTGGCC
		ctpC-Am-left2	CATGGCGAGGCGCTCAAG
pGMCS-P1-*virRsol*-Lk2-GFP11-*rv3267*(Cterm)-Lk15-GFP(1-10)			
Rv0822c(Cterm)	*M. tuberculosis* H37Rv chromosomal DNA	If-AmMBD-3267D	GAGCGCCTCGCCATGgagattcagcaccagcaggttacgacg
		If-L15-3267-Rv2	AGACAGCCCTGGACCgttgatgcactccggcgcgtc
pGMCS backbone	pGMCS-P1-*virRsol*-Lk2-GFP11-*ctpC*(1-85)-Lk15-GFP(1-10)	Flex15-Right	GGTCCAGGGCTGTCTGGCC
		ctpC-Am-left2	CATGGCGAGGCGCTCAAG
pGMCS-P1-*virRsol*-Lk2-GFP11-*rv3484*(Cterm)-Lk15-GFP(1-10)			
Rv0822c(Cterm)	*M. tuberculosis* H37Rv chromosomal DNA	If-AmMBD-3267D	GAGCGCCTCGCCATGgagattcagcaccagcaggttacgacg
		If-L15-3484-Rv2	AGACAGCCCTGGACCgttcacgcagggcacgccg
pGMCS backbone	pGMCS-P1-*virRsol*-Lk2-GFP11-*ctpC*(1-85)-Lk15-GFP(1-10)	Flex15-Right	GGTCCAGGGCTGTCTGGCC
		ctpC-Am-left2	CATGGCGAGGCGCTCAAG
pGMCS-P1-*virRsol*-Lk2-GFP11-*rv0822c*-Lk15-GFP(1-10)			
Rv0822c	*M. tuberculosis* H37Rv chromosomal DNA	If-AmMBD-0822c	GAGCGCCTCGCCATGagtgacggcgagagcg
		If-L15-0822c-Rv	AGACAGCCCTGGACCctactcgcaggtggtgtcgg
pGMCS backbone	pGMCS-P1-*virRsol*-Lk2-GFP11-*ctpC*(1-85)-Lk15-GFP(1-10)	Flex15-Right	GGTCCAGGGCTGTCTGGCC
		ctpC-Am-left2	CATGGCGAGGCGCTCAAG
pGMCS-P1-*virRsol*-Lk2-GFP11-*rv3267*-Lk15-GFP(1-10)			
Rv3267(Cterm)	*M. tuberculosis* H37Rv chromosomal DNA	If-AmMBD-3267	GAGCGCCTCGCCATGatgtctgcgcaacgtgtggttc
		If-L15-3267-Rv	AGACAGCCCTGGACCtcagttgatgcactccggcgc
pGMCS backbone	pGMCS-P1-*virRsol*-Lk2-GFP11-*ctpC*(1-85)-Lk15-GFP(1-10)	Flex15-Right	GGTCCAGGGCTGTCTGGCC
		ctpC-Am-left2	CATGGCGAGGCGCTCAAG
pGMCS-P1-*virRsol*-Lk2-GFP11-*rv3484*-Lk15-GFP(1-10)			
Rv3484(Cterm)	*M. tuberculosis* H37Rv chromosomal DNA	If-AmMBD-3484	GAGCGCCTCGCCATGgcgcgttctgagggc
		If-L15-3484-Rv	AGACAGCCCTGGACCctagttcacgcagggcacgc
		Flex15-Right	GGTCCAGGGCTGTCTGGCC

pGMCS backbone	pGMCS-P1-*virRsol*-Lk2-GFP11-*ctpC*(1-85)-Lk15-GFP(1-10)	ctpC-Am-left2	CATGGCGAGGCGCTCAAG
CRISPRi mutants			
virR (158.1) c2	Rv0431	Rv0431crispr 1 F	GGGAGAGCAGCAGGAAGACGACGC
		Rv0431crispr 1 R	AAACGCGTCGTCTTCCTGCTGCTC
virR (42.2) c1	Rv0431	Rv0431crispr 2 F	GGGAACGAACCCAGTGCCTGCCAGA
		Rv0431crispr 2 R	AAACTCTGGCAGGCACTGGGTTCGT
cei (145.2) c1	Rv2700	Rv2700crispr 1 F	GGGAATCACGCAAGTCACCACCAC
		Rv2700crispr 1 R	AAACGTGGTGGTGACTTGCGTGAT
cei (47.3) c2	Rv2700	Rv2700crispr 2 F	GGGAGTCGGTGCCGAGCGCAAGGTCG
		Rv2700crispr 2 R	AAACGACCTTGCGCTCGGCACCGAC
VirR-Venus primers			
VirR-F			TCACTGGGGTGCTGGTTACAGTGGGCTC
VirR-R			ATAGGATCGCCGGTCACCACGACGAT
pMV-F			TGACCGGCGATCCTATGGTGAGCAAGGGC
pMV-R			ACCAGCACCCCAGTGAAAAGTTCTTCTCCTTTACTC

1757

1758 **Supplementary Table 2**. Gradient mobile phase composition for ion-pairing LC-MS/MS
1759 for the quantification of acetyl-CoA, methyl citrate and methylmalonyl-CoA.

Time (min)	Mobile Phase (%)	
	A	B
1	100	0
2	55	45
7	50	50
7.5	5	95
8	5	95
8.5	100	0
10	End	

1760 A: water-methanol 07:3 (v/v) + 10mM tributylamine + 3mM acetic acid; B: pure methanol
1761

1762 **Supplementary Table 3**. Gradient mobile phase composition for ion-pairing LC-MS/MS
1763 for the quantification of pyruvate.

Time (min)	Mobile Phase (%)	
	A	B
1	5	95
6	95	5
7	95	5
8	5	95
10	End	

1764 A: pure water; B: pure methanol
1765

1766 **Supplementary Table 4**. Quantifier MRM transitions and collision energies used for
1767 acety-CoA, methyl citrate, methylmalonyl-CoA and pyruvate.

Metabolite	Precursor ion $[M-H]^-$ (m/z)	Product ion (m/z)	Collision energy (eV)

Acetyl-CoA	808.00	407.95	41
Methyl citrate	204.90	125.10	13
Methylmalonyl-CoA	432.60	410.50	10
Pyruvate	87.20	43.10	13

1768
1769
1770
1771
1772 **Supplementary figures**

1773 **Fig S1. Diversity of *Mtb* LCP proteins**. (**A**) Domain structure of LCP proteins in *Mtb*.
1774 Proteins are organized according to the presence of (i) both LCP (green) and LytR_C
1775 (slight orange) terminal domain (Rv3267, Rv3484 and Rv0822); (ii) the solo LytR_C
1776 domain (VirR and Rv2700); and the solo LCP domain (Rv3840). Additional information
1777 is provided for *Mtb* mutants in the indicated genes. (**B**) Phylogenetic analysis of LCP
1778 proteins in Mycobacteria (*M. tuberculosis, M. smegmatis, M. marinum and M. leprae*).
1779 The unrooted tree includes seven separate clusters for proteins with both LCP and
1780 LytR_C terminal domains (CpsA1, CpsA2 and CpsA3); with the solo LytR_C terminal
1781 domain (Solo_LytRC1 and Solo_LytRC2); with the solo LCP domain; and a separate
1782 cluster including the characterized LCP proteins from *S. pneumonia* and *S. aureus*. Note
1783 the clustering of one of the *M. smegmatis* LCP proteins with this group. VirR is highlighted
1784 in blue.

1785

1786 **Fig S2. The enhanced vesiculation phenotype of *virR^{mut}* occurs in the absence of**
1787 **cell lysis**. **(A)** Nanoparticle tracking analysis (NTA) of EV preparations derived from WT
1788 and the indicated strains showing number of particles per cm^3 determined by Zeta View
1789 NTA in three independent EV preparations. Data are presented as mean ± SEM.
1790 *$P \leq 0.05$ (One-way ANOVA with Tukey's multiple comparisons test). **(B)** Cell lysis
1791 control of *virR^{mut}*. Shown are immunoblots of cell lysates and culture supernatants (SN)
1792 for the indicated strains. The cytoplasmic protein IdeR was detected in cell lysates but
1793 not in culture supernatants confirming cell integrity, while the secreted protein Ag85b
1794 was readily detected in the culture supernatants. **(C)** Cell lysis control of *Mtb* submitted
1795 to conditions that alter permeability. Arrows indicate the size of the proteins of interest
1796 detected by immunoblot. **(D)** Alternatively, cell viability was tested by serial dilution and
1797 plating onto 7H10 medium. Cultures from B and C were submitted to serial dilutions (10^{-}
1798 ^{1} to 10^{-5}) and plated onto 7H10 after reaching an OD_{600nm} of 0.2.

1799

1800 **Fig S3. H2O2 sensitivity assay.** The indicated strains were initially grown on 7H9
1801 medium supplemented with AND to an OD of 0.5. Washed cells were then transferred to

1802 the same medium supplemented with and without 13mM H202. After 8 h, cells were
1803 diluted down as indicated and spotted onto 7H10 solid medium.
1804 **Fig S4. Expression patterns of permeability-dependent genes upregulated in**
1805 **cultures exposed to cholesterol and simultaneously downregulated in *virR*^{mut}.**
1806
1807 **Fig S5. Behaviour of *virR*^{mut} upon conditions that modulate permeability. (A)**
1808 Growth curves of *virR*^{mut} in MM supplemented with either glycerol, cholesterol or glycerol
1809 plus TRZ at the indicated concentrations. **(B)** Dotblot analysis of vesiculation levels of
1810 *virR*^{mut} on the indicated culture media. a, b and c denote biological replicates.
1811 Quantification of the dotblot was done by measuring the integrated density of each dot
1812 using ImageJ. Data are mean and standard deviations. * p=0.021 after applying a Tuke's
1813 multiple comparison test. **(C)** Time course of the uptake of ethidium bromide (EthBr) by
1814 *virR*^{mut} grown in the indicated conditions, as measured by fluorescence at 590=nm for 65
1815 min. Data are mean and standard deviation of three biological replicates.
1816
1817 **Fig S6. Expression patterns of ribosomal proteins in the EVs from WT, *virR*^{mut}**
1818 **and *virR*^{mut} -Comp strains. Proteins shown are downregulated in the vesicles of**
1819 ***virR*^{mut} with respect to both VirR expressing strains.**
1820
1821 **Fig S7. Expression patterns in the EVs from WT, *virR*^{mut} and *virR*^{mut} -Comp strains**
1822 **of proteins differentially expressed in *virR*^{mut} that contribute to enrichments of**
1823 **terms related to metabolism of: (A) nucleotides (B) amino-acids (C)**
1824 **oligosaccharides (D) glycogen.**
1825
1826 **Fig S8. TLC analysis of strains grown in the presence of cholesterol or TRZ.**
1827 Analysis of polar lipids, including SL1 and DATs lipids of the indicated strains by TLC.
1828 Sulfolipid 1 (SL1); diacylglytrehaloses (DATs); Trehalose dimycolate (TDM).
1829
1830 **Fig S9. Additional AFM data. (A-C) (i)** Atomic force microscopy images taken in liquid
1831 from a big area showing the sample heterogeneity overview with various peptidoglycan
1832 fragments of the following samples: **(A)** WT, **(B)** *virR*^{mut}, **(C)**, *virR*^{mut}-C. **(ii)** Atomic force
1833 microscopy images zoom in one individual peptidoglycan fragment corresponding to one
1834 cell from different samples: **(A)** WT, **(B)** *virR*^{mut} showing the background (Backg.), the
1835 external surface (Ext) the internal (Int), **(C)**, *virR*^{mut}-C, white square showing the size of
1836 the zoom images shown in Figure 5 from the external surface of the cells. **(D)** Curve of
1837 grey points showing 255 slices of one AFM image taken using a FIJI macro, in the x axis
1838 and the total number of pores in the y axis, the red line is a Gaussian fitted to the curve

1839 and the maximum of the Gaussian is marked with a dash red line showing slice 140 in
1840 this example corresponding to the slice of the image with the maximum number of pores.
1841 **(E)** Binary slice number 140 from the original AFM image showing the pores in white and
1842 the material represented in black. **(F)** The pores from 'E' were analyzed using the FIJI
1843 macros where each pore area was measured and plotted in the x axis against the
1844 cumulative fraction of total pore area in the y axis as shown in the curve by blue dots.
1845 The red dot marks the most likely pore area which corresponds to the half of the
1846 cumulative fraction of the total pore area, this area was then used to obtain the pore
1847 diameter of the image. The same was repeated with the n = 8 images for each sample
1848 to compose the graphs 'D' and 'E' from Figure 7.
1849
1850 **Fig S10**. **Sensitivity to lysozyme of *virR^{mut}*. (A)** Analysis of the minimum inhibitory
1851 concentration (MIC) of lysozyme of the indicated strains by the resazurin method. **(B)**
1852 Growth of WT and *virR^{mut}* treated with 0 or 50 µg/ml lysozyme (Lys). Data represents the
1853 mean ± SEM of three independent cultures.
1854
1855 **Fig S11. Localization of VirR by fluorescence microscopy**. Fluorescence images of
1856 a *Mtb* strain expressing Venus-tagged VirR.
1857
1858 **Fig S12. Split-GFP strategy. (A)** *Upper panel*. Scheme of the plasmid used to test VirR
1859 interactions in vivo. *Lower panel*. Scheme of the potential molecular interaction between
1860 VirR and Lcp1 using split-GFP. **(B)** Gating strategy to analyze split-GFP flow cytometry
1861 data. Bacteria were first sorted based on size (FSC) and structure (SSC) to exclude
1862 debris (1). Then, aggregates were excluded based on FSC and SSC width (W) and
1863 eighth (H) (2,3). GFP signal was then analyzed *vs*. SSC (4) or mCherry, when relevant
1864 (5).
1865
1866 **Supplementary file S1**: FileS1_RNA_differential_expression.xlsx: Results of the
1867 differential expression analyses for the RNA-seq dataset.
1868
1869 **Supplementary file S2**: FileS2_GOenrichments_RNA.xlsx: Gene ontology enrichment
1870 analyses conducted on sets of genes up (N=399), and down-regulated (N=502) in the
1871 *virR^{mut}* strain. Rows highlighted correspond to terms selected for graphical
1872 representation (figure 3E, OR>2 & FDR<0.1)
1873
1874 **Supplementary file S3**: FileS3_TRN_regulon_enrichments.xlsx: Enrichment analyses
1875 for the Transcription factor regulons reported in (Minch et al. 2015).

1876

1877 **Supplementary file S4**: FileS4_Proteins_differential_expression.xlsx: Results of the
1878 differential expression analyses for the LF-MS dataset.

1879

1880 **Supplementary file S5**: FileS5_GOenrichments_proteins.xlsx: Gene ontology
1881 enrichment analyses conducted on sets of protein up (N=117), and down-regulated
1882 (N=108) in the extracellular vesicles of the *virR*^{mut} strain. Rows highlighted correspond
1883 to terms selected for graphical representation (figure 5F, OR>2 & FDR<0.1).

1884

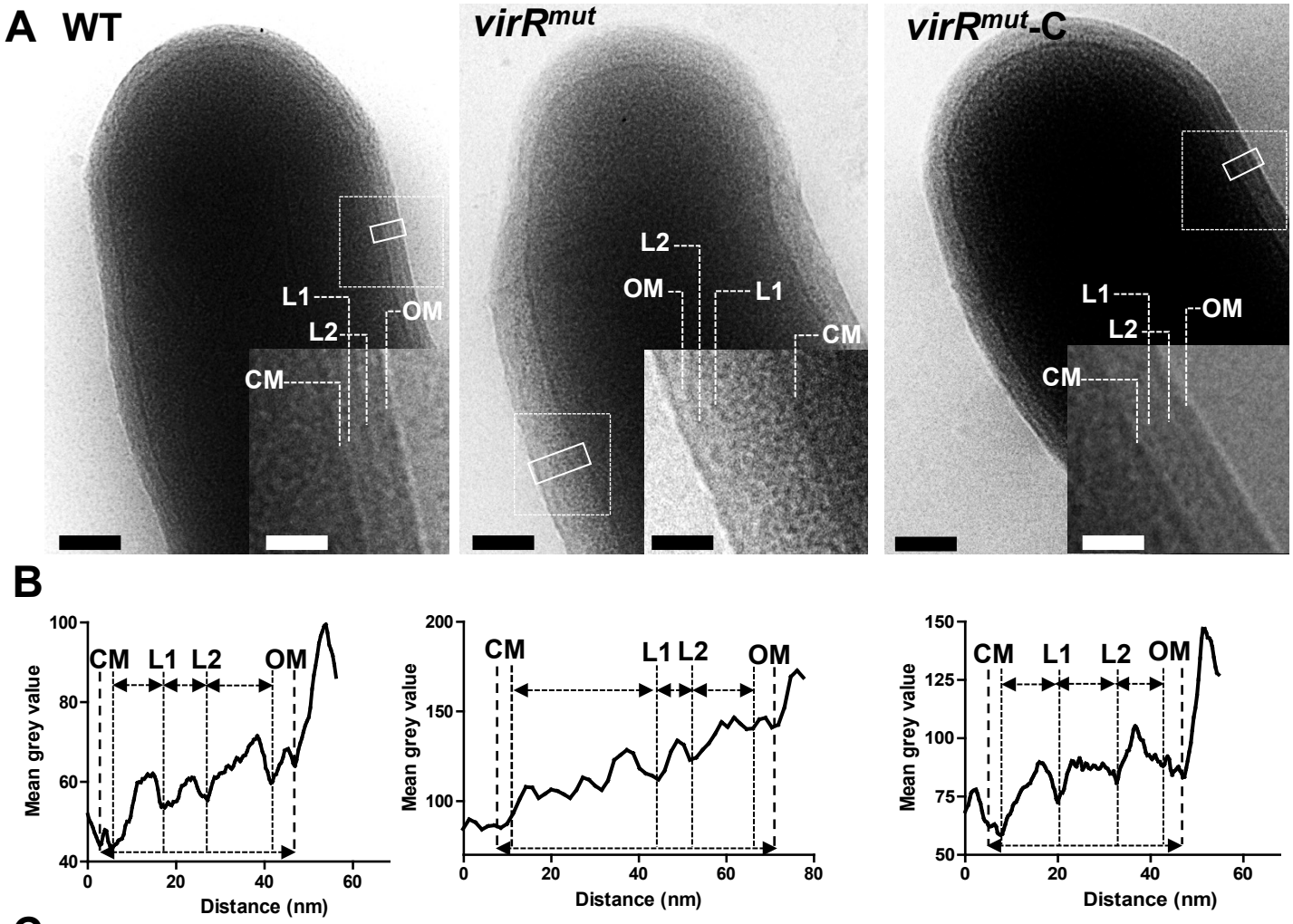

C

	CM	CM-OM	CM-L1	OM-L2	L1-L2	OM
WT	2.7±0.2	44.09±3.1	11.2±0.4	13.34±0.9	10.46±1.4	5.7±0.4
***virR*^{mut}**	5.4±0.7*	62.7±3.2*	31.36±3.2*	15.1±2.2	6.8±0.9*	6.1±0.3
***virR*^{mut}-C**	2.5±0.5	41.6±0.7	12.4±1.4	10.03±1.1	12.6±1.3	5±0.2

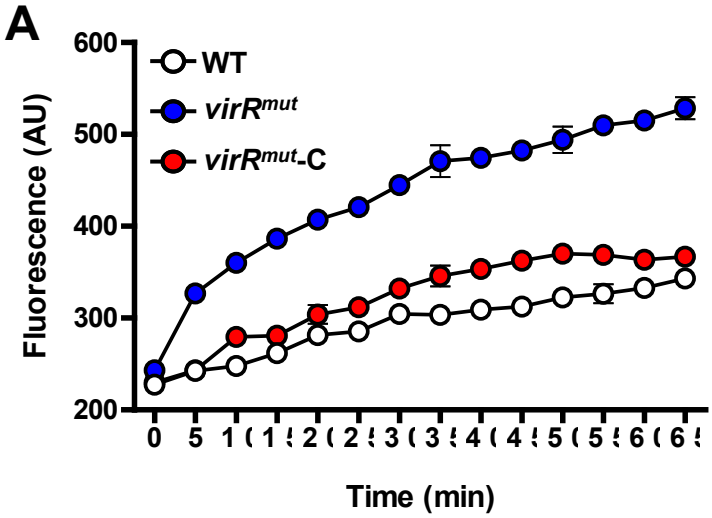
A
WT
virRmut
virRmut-C
Fluorescence (AU)
600
500
400
300
200
0
5
1 (
1 !
2 (
2 !
3 (
3 !
4 (
4 !
5 (
5 !
6 (
6 !
Time (min)

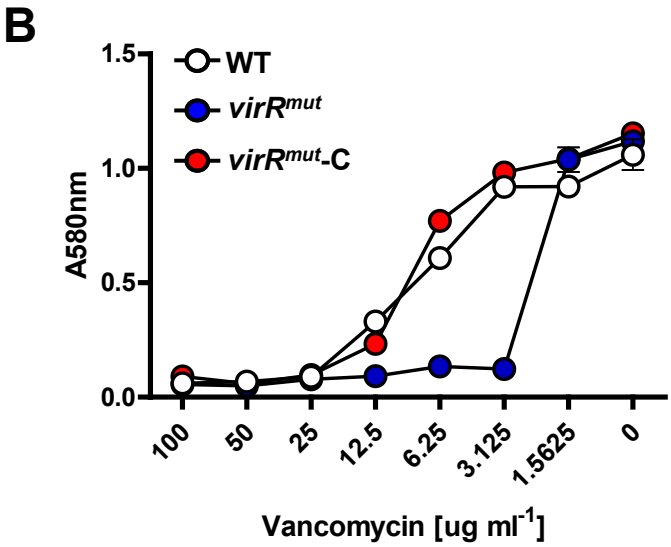
B
WT
virRmut
virRmut-C
A580nm
1.5
1.0
0.5
0.0
100
50
25
12.5
6.25
3.125
1.5625
0
Vancomycin [ug ml-1]

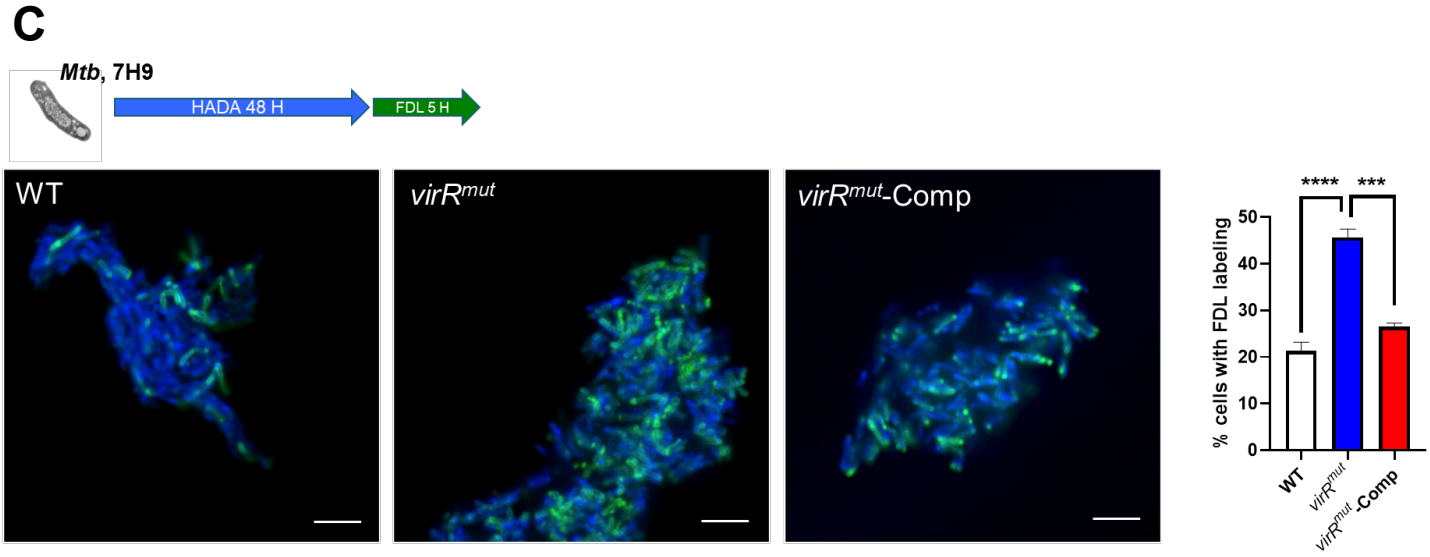
C
Mtb, 7H9
HADA 48 H
FDL 5 H
WT
virRmut
virRmut-Comp
****
***
% cells with FDL labeling
50
40
30
20
10
0
WT
virRmut
virRmut-Comp

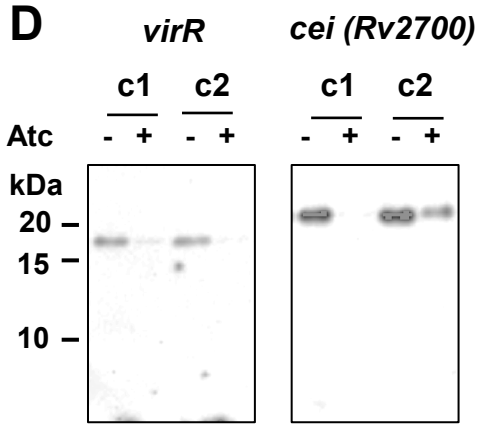
D
virR
cei (Rv2700)
c1
c2
c1
c2
Atc
-
+
-
+
-
+
-
+
kDa
20
15
10

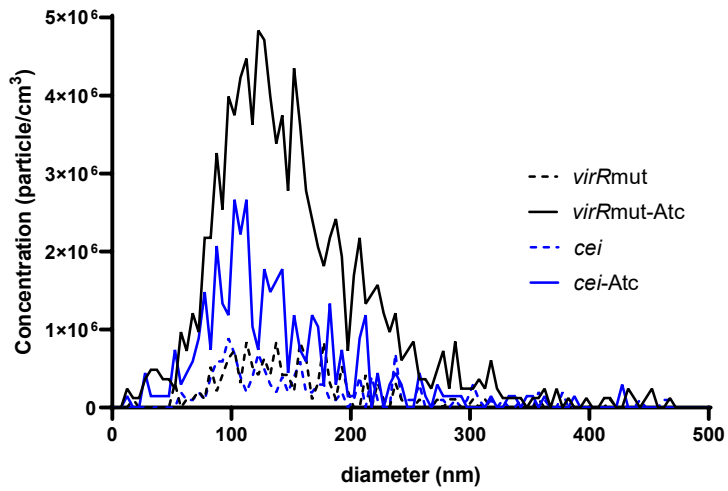
E
5×10⁶
4×10⁶
3×10⁶
2×10⁶
1×10⁶
0
Concentration (particle/cm3)
virRmut
virRmut-Atc
cei
cei-Atc
0
100
200
300
400
500
diameter (nm)

Figure 2

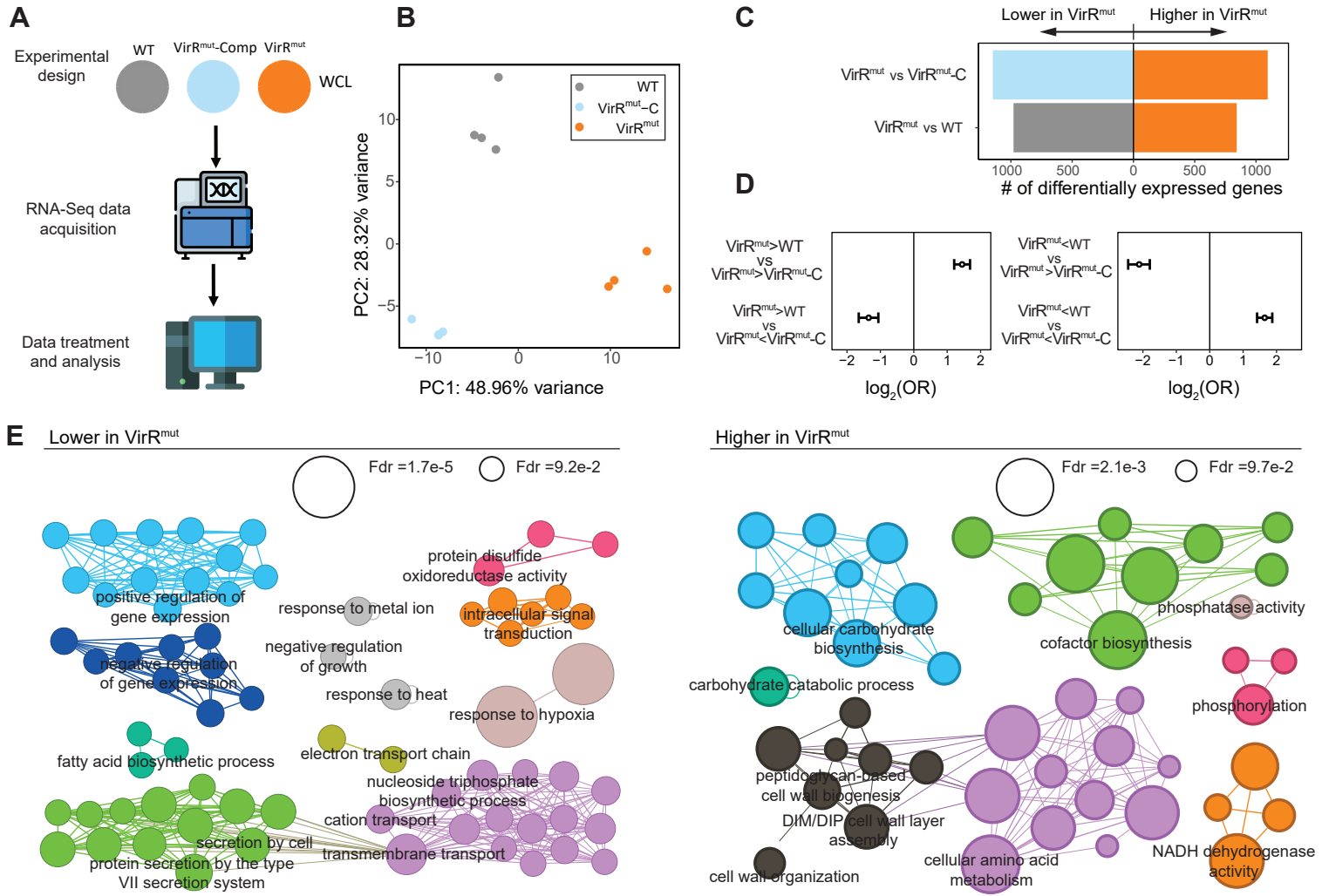
A
Experimental design
WT
VirRmut-Comp
VirRmut
WCL
RNA-Seq data acquisition
Data treatment and analysis
B
WT
VirRmut-C
VirRmut
PC2: 28.32% variance
PC1: 48.96% variance
C
Lower in VirRmut
Higher in VirRmut
VirRmut vs VirRmut-C
VirRmut vs WT
# of differentially expressed genes
D
VirRmut>WT vs VirRmut>VirRmut-C
VirRmut>WT vs VirRmut<VirRmut-C
VirRmut<WT vs VirRmut>VirRmut-C
VirRmut<WT vs VirRmut<VirRmut-C
log2(OR)
E
Lower in VirRmut
Fdr =1.7e-5
Fdr =9.2e-2
positive regulation of gene expression
negative regulation of gene expression
fatty acid biosynthetic process
secretion by cell
protein secretion by the type VII secretion system
response to metal ion
negative regulation of growth
response to heat
electron transport chain
cation transport
transmembrane transport
nucleoside triphosphate biosynthetic process
protein disulfide oxidoreductase activity
intracellular signal transduction
response to hypoxia
Higher in VirRmut
Fdr =2.1e-3
Fdr =9.7e-2
cellular carbohydrate biosynthesis
carbohydrate catabolic process
peptidoglycan-based cell wall biogenesis
DIM/DIP cell wall layer assembly
cell wall organization
cellular amino acid metabolism
cofactor biosynthesis
phosphatase activity
phosphorylation
NADH dehydrogenase activity

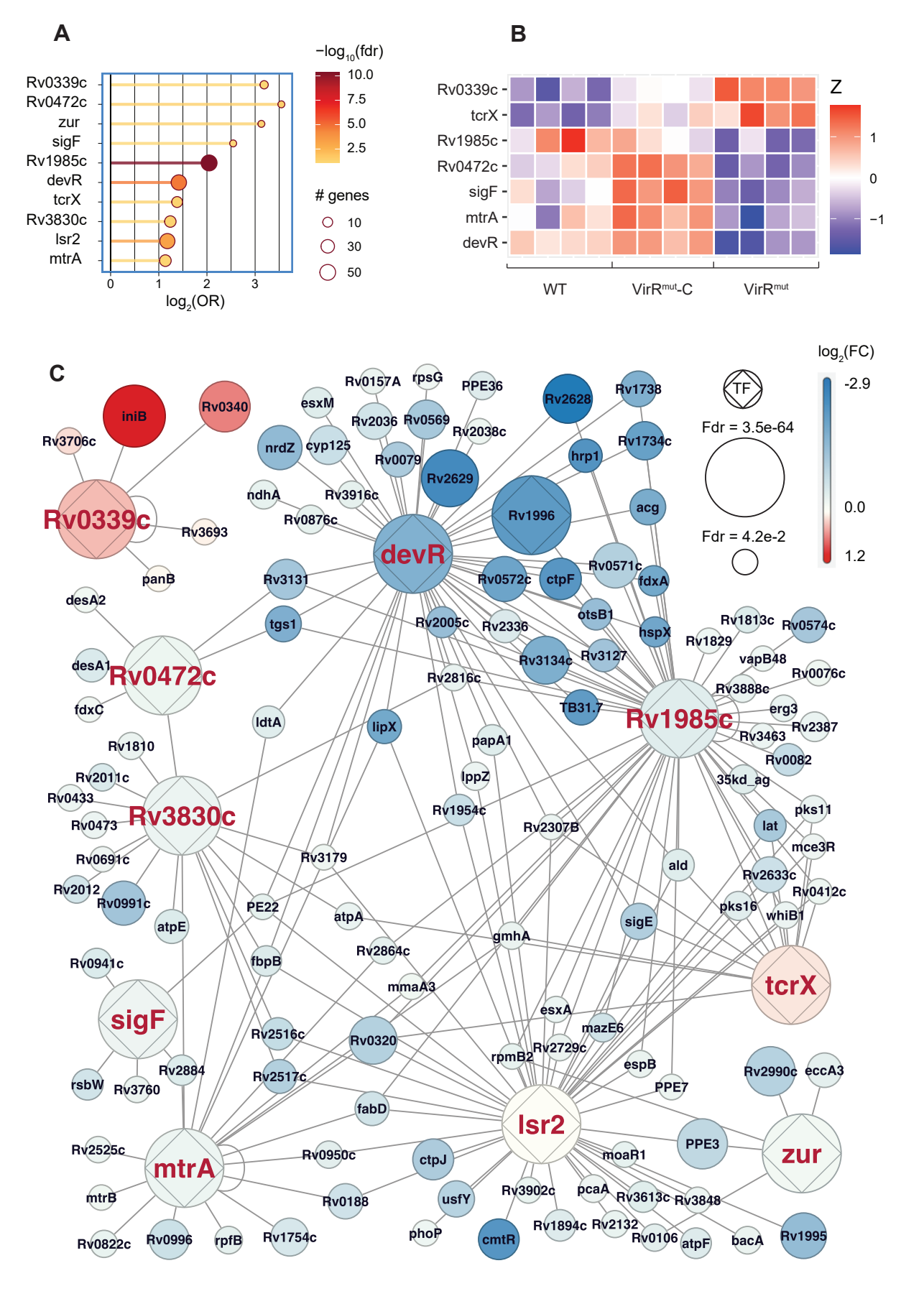
A
Rv0339c
Rv0472c
zur
sigF
Rv1985c
devR
tcrX
Rv3830c
lsr2
mtrA
0
1
2
3
log2(OR)
−log10(fdr)
10.0
7.5
5.0
2.5
genes
10
30
50
B
Rv0339c
tcrX
Rv1985c
Rv0472c
sigF
mtrA
devR
WT
VirRmut-C
VirRmut
Z
1
0
−1
C
log2(FC)
-2.9
0.0
1.2
TF
Fdr = 3.5e-64
Fdr = 4.2e-2
iniB
Rv0340
Rv3706c
Rv0339c
Rv3693
panB
desA2
desA1
Rv0472c
fdxC
Rv1810
Rv2011c
Rv0433
Rv3830c
Rv0473
Rv0691c
Rv2012
Rv0991c
atpE
Rv0941c
sigF
Rv2884
rsbW
Rv3760
mtrA
Rv2525c
mtrB
Rv0822c
Rv0996
rpfB
Rv1754c
Rv0157A
rpsG
PPE36
esxM
Rv2036
Rv0569
Rv2038c
nrdZ
cyp125
Rv0079
Rv2629
ndhA
Rv3916c
Rv0876c
devR
Rv3131
tgs1
Rv2005c
Rv2336
Rv3134c
Rv3127
Rv2816c
TB31.7
ldtA
lipX
papA1
lppZ
Rv1954c
Rv2307B
Rv3179
PE22
atpA
Rv2864c
fbpB
mmaA3
Rv2516c
Rv0320
Rv2517c
fabD
Rv0950c
ctpJ
usfY
Rv0188
phoP
cmtR
Rv2628
Rv1738
Rv1734c
hrp1
Rv1996
acg
Rv0571c
fdxA
Rv0572c
ctpF
otsB1
hspX
Rv1829
Rv1813c
Rv0574c
vapB48
Rv0076c
Rv3888c
erg3
Rv2387
Rv3463
Rv0082
35kd_ag
pks11
lat
mce3R
Rv2633c
Rv0412c
pks16
whiB1
ald
sigE
gmhA
tcrX
esxA
mazE6
Rv2729c
rpmB2
espB
PPE7
Rv2990c
eccA3
lsr2
PPE3
zur
moaR1
Rv3902c
pcaA
Rv3613c
Rv3848
Rv1894c
Rv2132
Rv0106
atpF
bacA
Rv1995

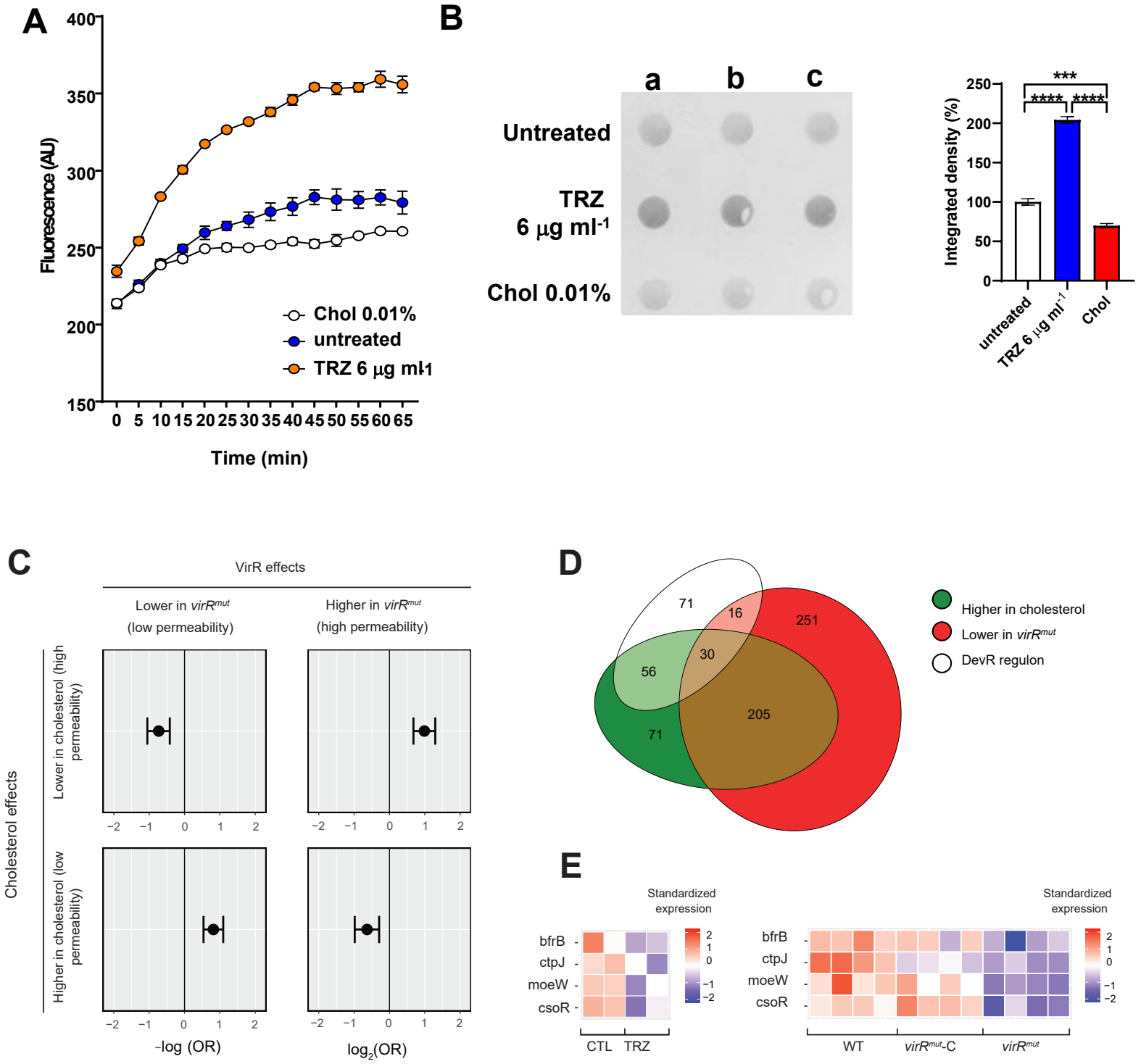
A
Fluorescence (AU)
Time (min)
Chol 0.01%
untreated
TRZ 6 μg ml-1
B
a
b
c
Untreated
TRZ
6 μg ml-1
Chol 0.01%
Integrated density (%)
untreated
TRZ 6 μg ml-1
Chol
C
VirR effects
Lower in virRmut
(low permeability)
Higher in virRmut
(high permeability)
Cholesterol effects
Lower in cholesterol (high permeability)
Higher in cholesterol (low permeability)
-log (OR)
log2(OR)
D
Higher in cholesterol
Lower in virRmut
DevR regulon
E
Standardized expression
bfrB
ctpJ
moeW
csoR
CTL
TRZ
WT
virRmut-C
virRmut

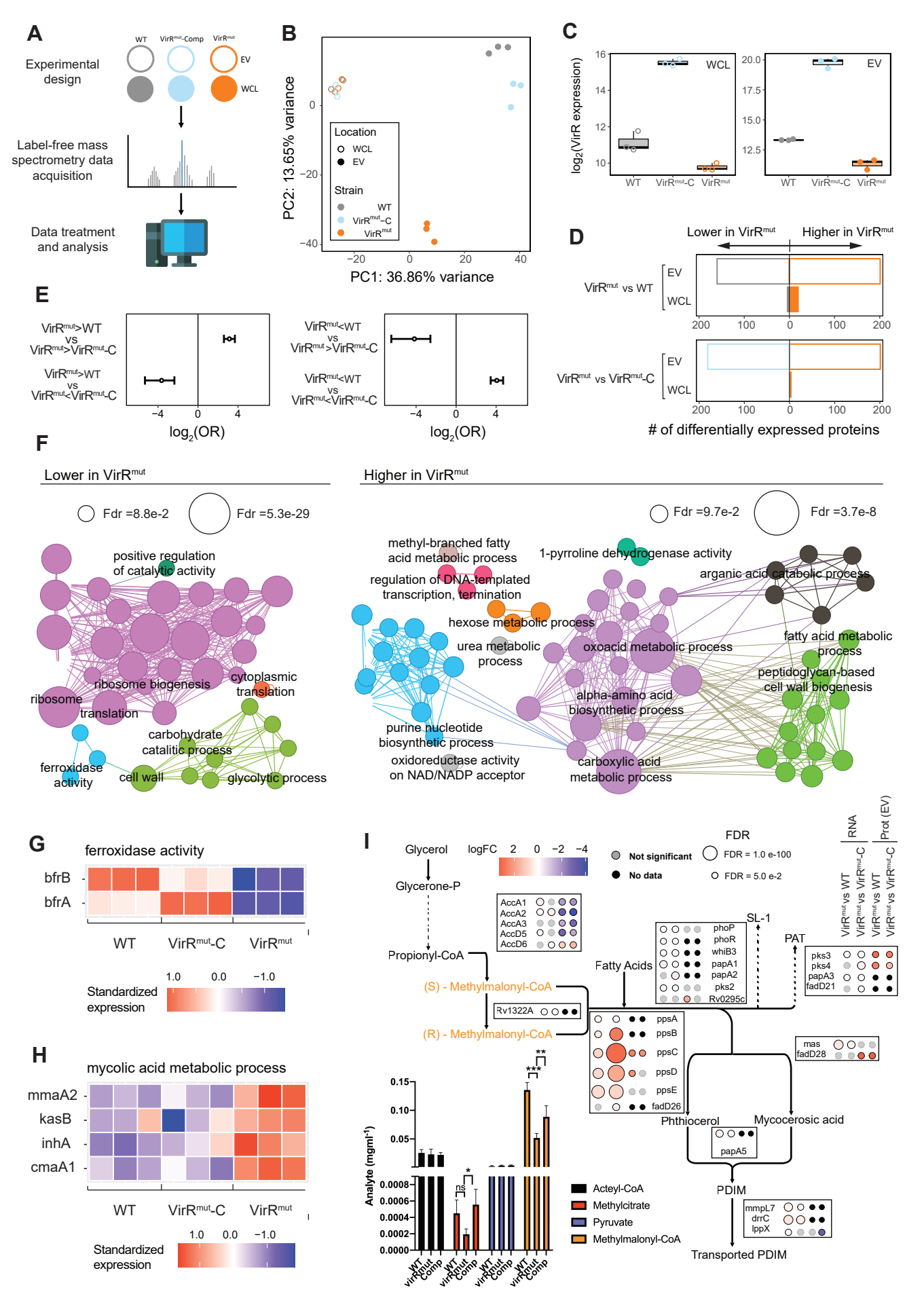
A
Experimental design
WT
VirRmut-Comp
VirRmut
EV
WCL
Label-free mass spectrometry data acquisition
Data treatment and analysis
B
PC2: 13.65% variance
PC1: 36.86% variance
Location
WCL
EV
Strain
WT
VirRmut-C
VirRmut
C
log2(VirR expression)
WCL
EV
WT
VirRmut-C
VirRmut
D
Lower in VirRmut
Higher in VirRmut
VirRmut vs WT
VirRmut vs VirRmut-C
EV
WCL
# of differentially expressed proteins
E
VirRmut>WT vs VirRmut>VirRmut-C
VirRmut>WT vs VirRmut<VirRmut-C
VirRmut<WT vs VirRmut>VirRmut-C
VirRmut<WT vs VirRmut<VirRmut-C
log2(OR)
F
Lower in VirRmut
Fdr =8.8e-2
Fdr =5.3e-29
positive regulation of catalytic activity
ribosome biogenesis
cytoplasmic translation
ribosome
translation
carbohydrate catalitic process
ferroxidase activity
cell wall
glycolytic process
Higher in VirRmut
Fdr =9.7e-2
Fdr =3.7e-8
methyl-branched fatty acid metabolic process
1-pyrroline dehydrogenase activity
arganic acid catabolic process
regulation of DNA-templated transcription, termination
hexose metabolic process
urea metabolic process
oxoacid metabolic process
fatty acid metabolic process
peptidoglycan-based cell wall biogenesis
alpha-amino acid biosynthetic process
purine nucleotide biosynthetic process
oxidoreductase activity on NAD/NADP acceptor
carboxylic acid metabolic process
G
ferroxidase activity
bfrB
bfrA
WT
VirRmut-C
VirRmut
Standardized expression
1.0
0.0
−1.0
H
mycolic acid metabolic process
mmaA2
kasB
inhA
cmaA1
WT
VirRmut-C
VirRmut
Standardized expression
1.0
0.0
−1.0
I
Glycerol
Glycerone-P
Propionyl-CoA
(S) - Methylmalonyl-CoA
(R) - Methylmalonyl-CoA
logFC
2
0
−2
−4
Not significant
No data
FDR
FDR = 1.0 e-100
FDR = 5.0 e-2
RNA
Prot (EV)
VirRmut vs WT
VirRmut vs VirRmut-C
AccA1
AccA2
AccA3
AccD5
AccD6
Rv1322A
Fatty Acids
phoP
phoR
whiB3
papA1
papA2
pks2
Rv0295c
SL-1
PAT
pks3
pks4
papA3
fadD21
ppsA
ppsB
ppsC
ppsD
ppsE
fadD26
mas
fadD28
Phthiocerol
Mycocerosic acid
papA5
PDIM
mmpL7
drrC
lppX
Transported PDIM
Analyte (mgml-1)
Acteyl-CoA
Methylcitrate
Pyruvate
Methylmalonyl-CoA
WT
virRmut
Comp
ns
*
**
***

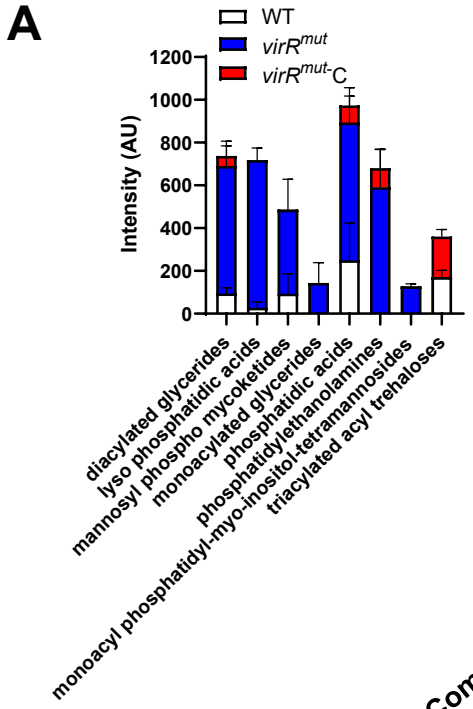
A
WT
virR^mut
virR^mut-C
Intensity (AU)
1200
1000
800
600
400
200
0
diacylated glycerides
lyso phosphatidic acids
mannosyl phospho mycoketides
monoacylated glycerides
phosphatidic acids
phosphatidylethanolamines
monoacyl phosphatidyl-myo-inositol-tetramannosides
triacylated acyl trehaloses

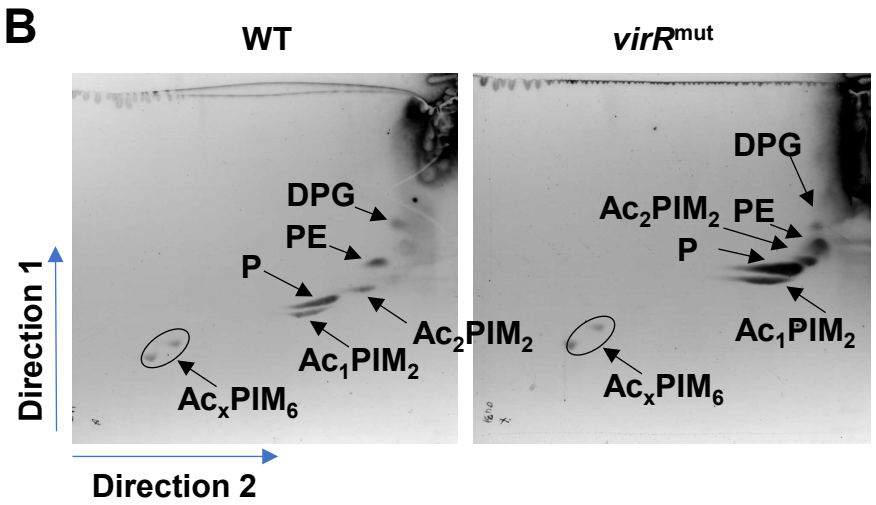
B
WT
virR^mut
DPG
PE
P
Ac2PIM2
Ac1PIM2
AcxPIM6
Direction 1
Direction 2

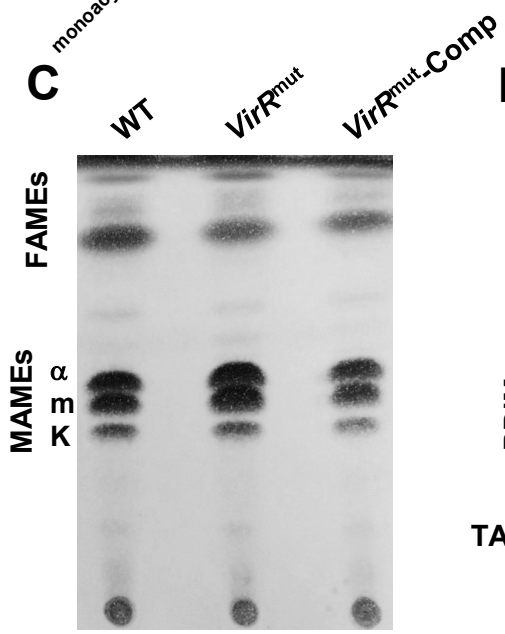
C
WT
VirR^mut
VirR^mut-Comp
FAMEs
MAMEs
α
m
K

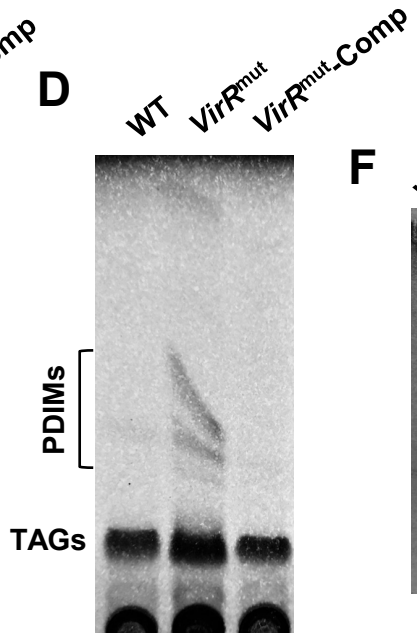
D
WT
VirR^mut
VirR^mut-Comp
PDIMs
TAGs

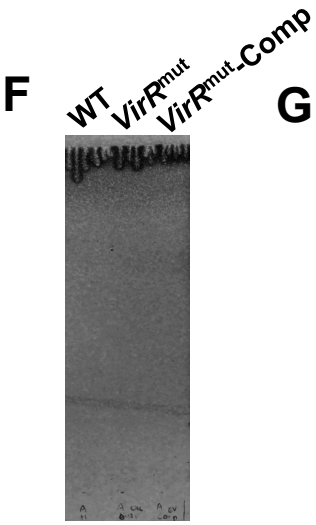
F
WT
VirR^mut
VirR^mut-Comp

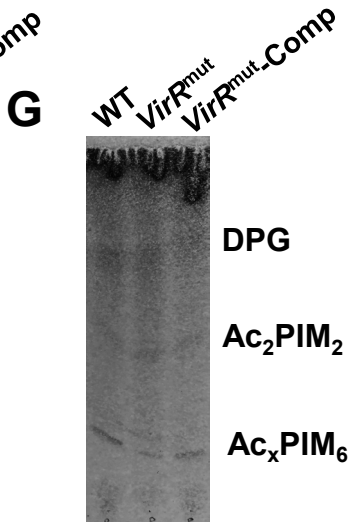
G
WT
VirR^mut
VirR^mut-Comp
DPG
Ac2PIM2
AcxPIM6

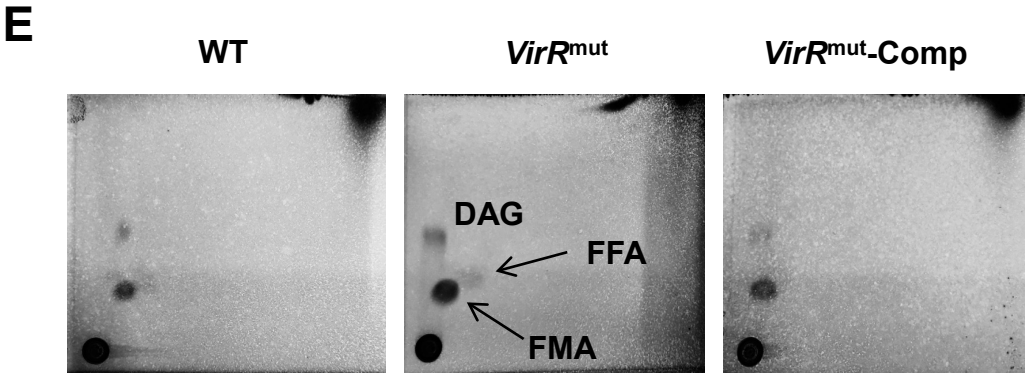
E
WT
VirR^mut
VirR^mut-Comp
DAG
FFA
FMA

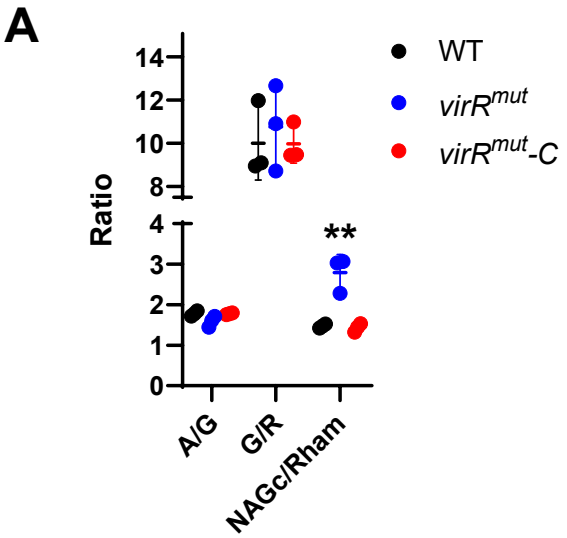

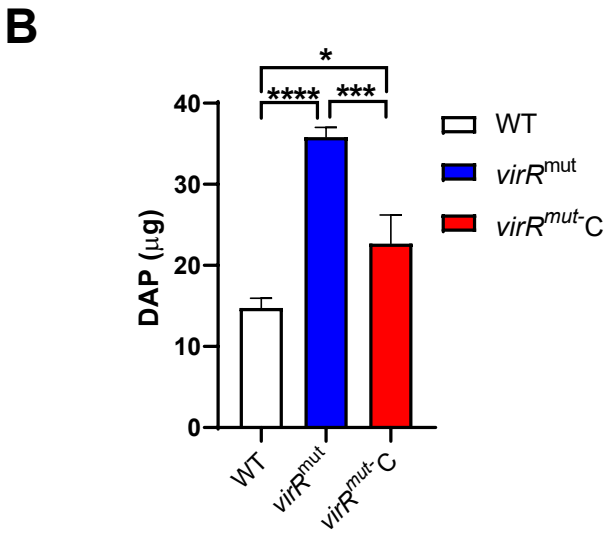

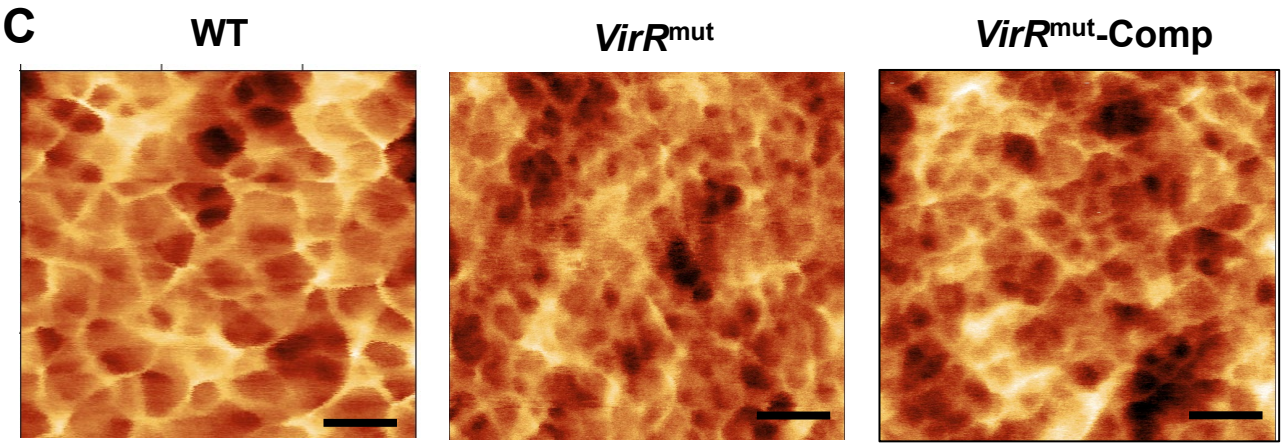

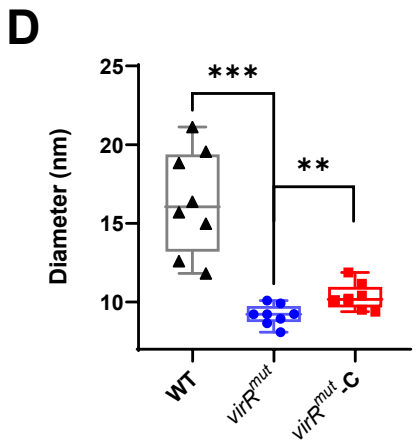

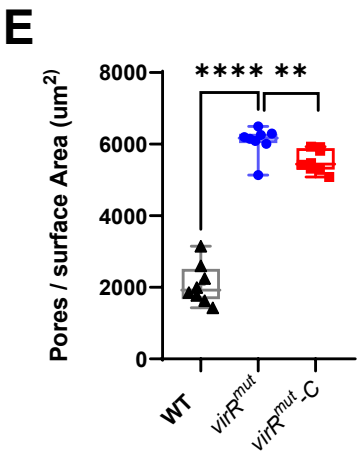

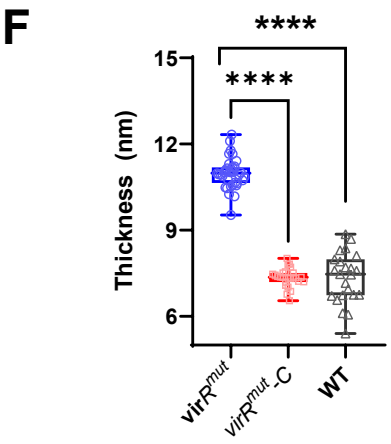

G

Peak	R.T	Observed	Expected	Best Match
1	4.3	942.432	942.4155	M4
2	6.12	1752.80	1752.7379	D43 (-N-Ac)
3	6.59	1823.856	1823.7750	D44(-N-Ac)
4	6.62	1,823.862	1823.7750	D44 (-N-Ac)
5	6.87	1794.8	1794.7755	D43
6	7.1	1794.8	1794.7755	D34
7	7.76	1865.854	1865.8126	D44
8	8.82	1831.86	1831.748	D45N(-NH2,-2N-Ac)
9	9.7	2789.26	2789.2098	T444
10	10.56	1845,806	1774.7493	D44N (Anh)

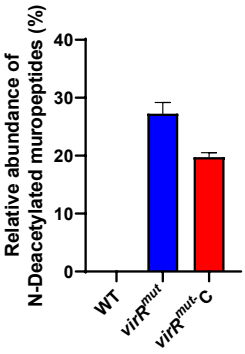

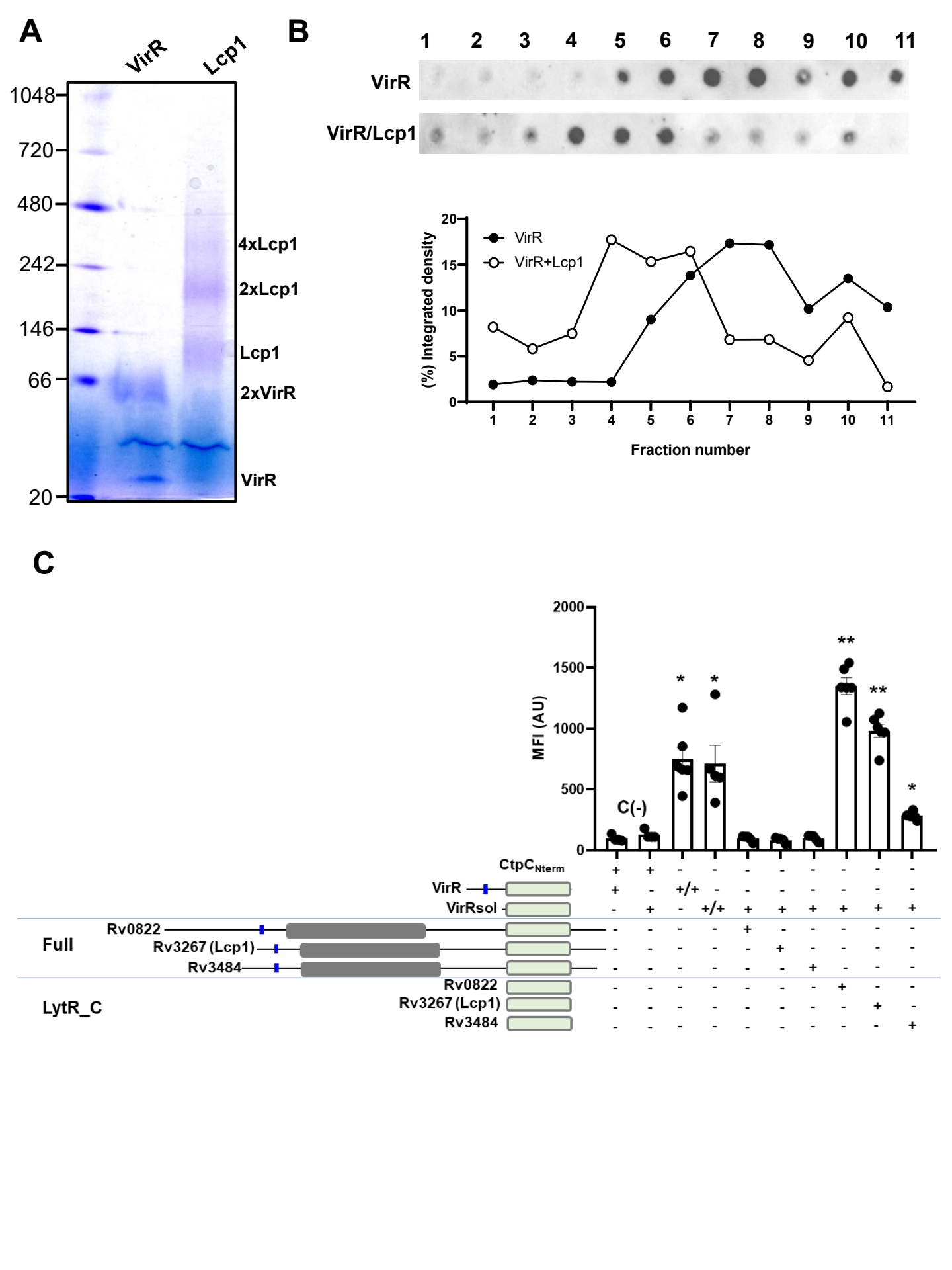
A
VirR
Lcp1
1048
720
480
242
146
66
20
4xLcp1
2xLcp1
Lcp1
2xVirR
VirR
B
1 2 3 4 5 6 7 8 9 10 11
VirR
VirR/Lcp1
(%) Integrated density
VirR
VirR+Lcp1
Fraction number
C
MFI (AU)
C(-)
CtpC$_{Nterm}$
VirR
VirRsol
Full
Rv0822
Rv3267 (Lcp1)
Rv3484
LytR_C
Rv0822
Rv3267 (Lcp1)
Rv3484

A

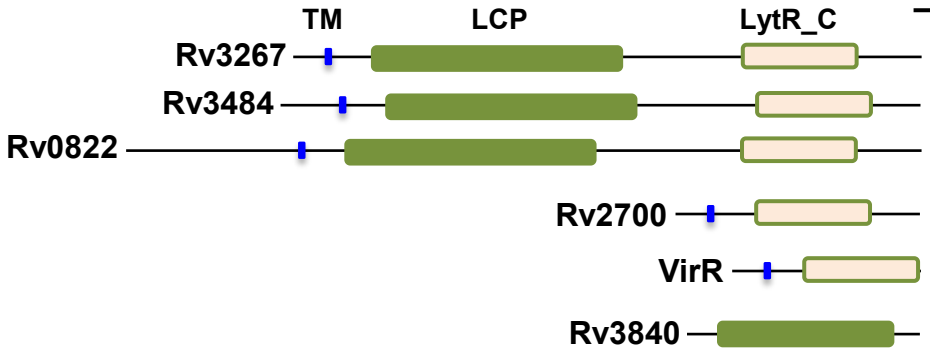

	Growth defect	Release material	Attenuated Virulence
Rv3267	Yes	No	No
Rv3484	No	No	Yes
Rv0822	No	No	No
Rv2700	Yes	?	Yes
VirR	-/+	+++	Yes
Rv3840	?	?	?

B

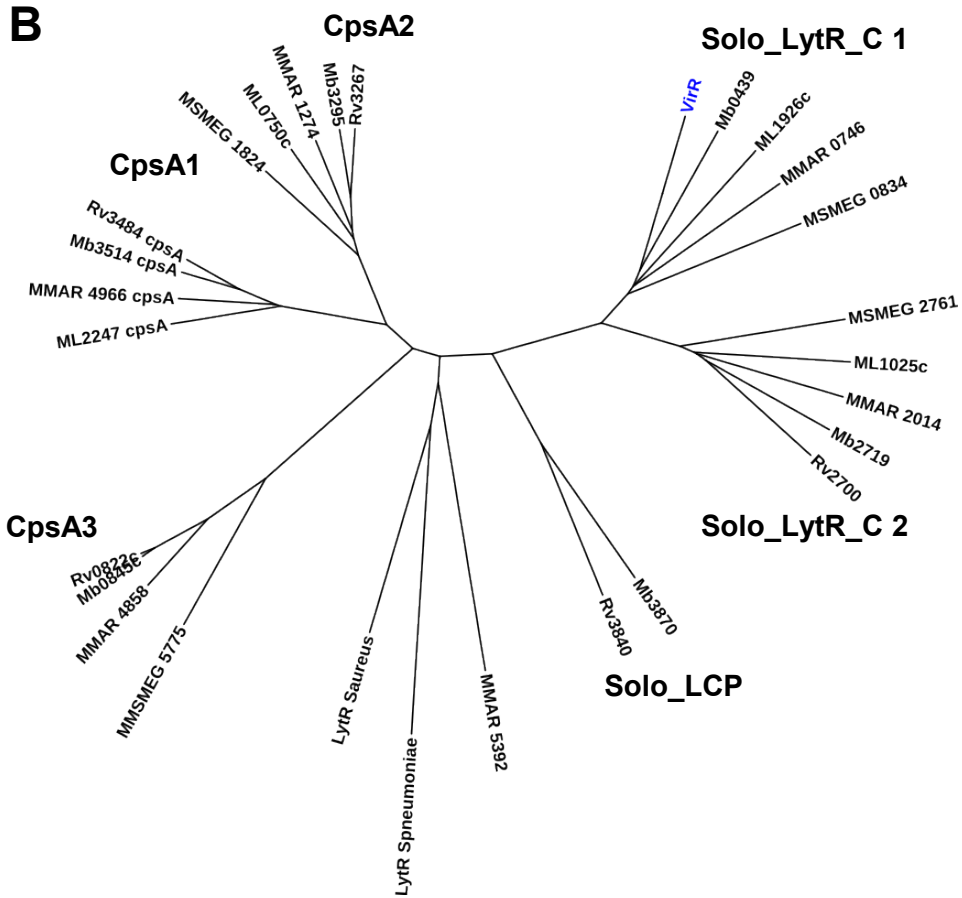

Fig S1

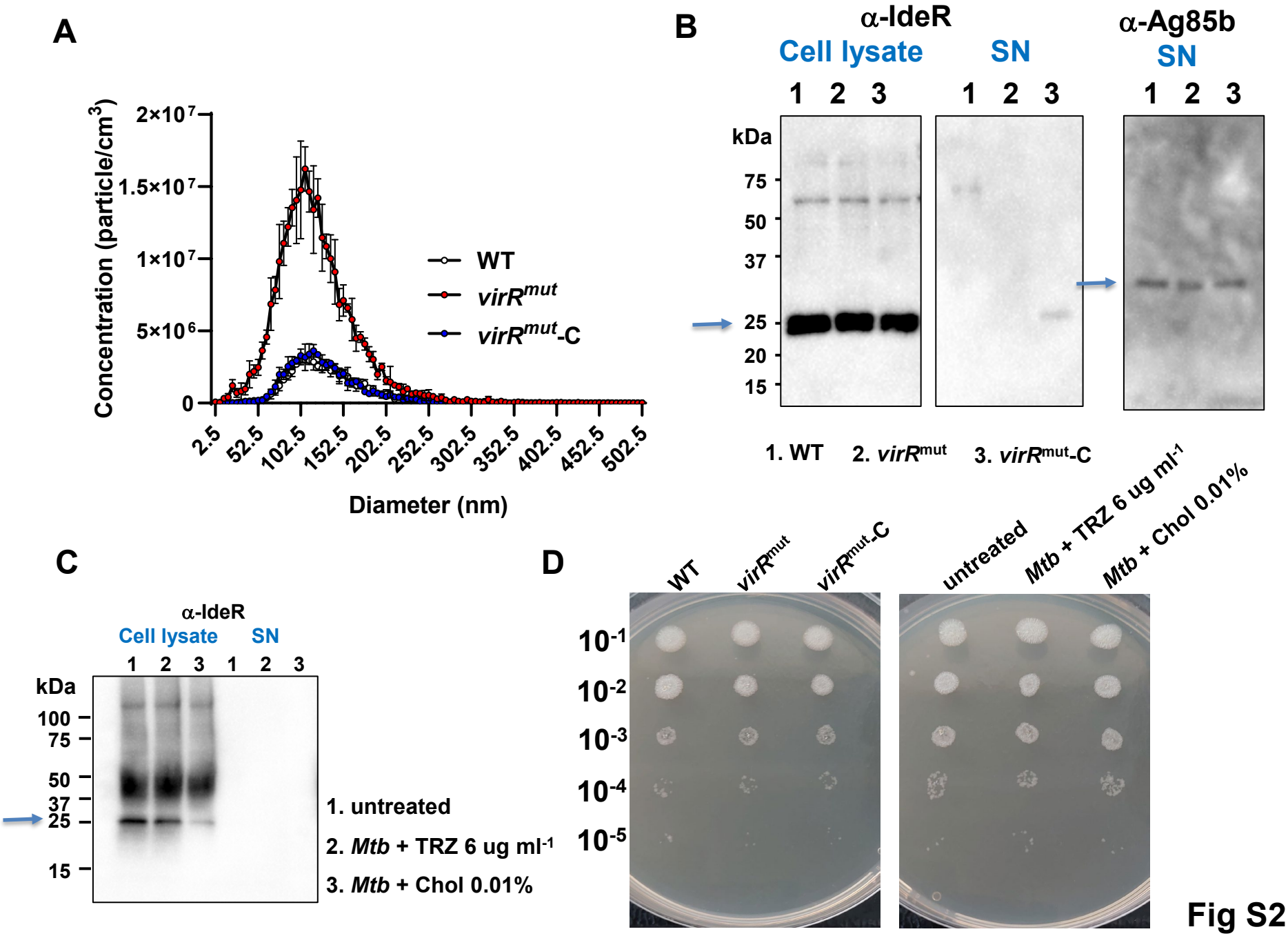
A
Concentration (particle/cm3)
2×10^7
1.5×10^7
1×10^7
5×10^6
0
WT
virRmut
virRmut-C
2.5
52.5
102.5
152.5
202.5
252.5
302.5
352.5
402.5
452.5
502.5
Diameter (nm)
B
α-IdeR
Cell lysate
SN
α-Ag85b
SN
1 2 3
1 2 3
1 2 3
kDa
75
50
37
25
20
15
1. WT
2. virRmut
3. virRmut-C
C
α-IdeR
Cell lysate
SN
1 2 3 1 2 3
kDa
100
75
50
37
25
15
1. untreated
2. Mtb + TRZ 6 ug ml-1
3. Mtb + Chol 0.01%
D
WT
virRmut
virRmut-C
untreated
Mtb + TRZ 6 ug ml-1
Mtb + Chol 0.01%
10-1
10-2
10-3
10-4
10-5

Fig S2

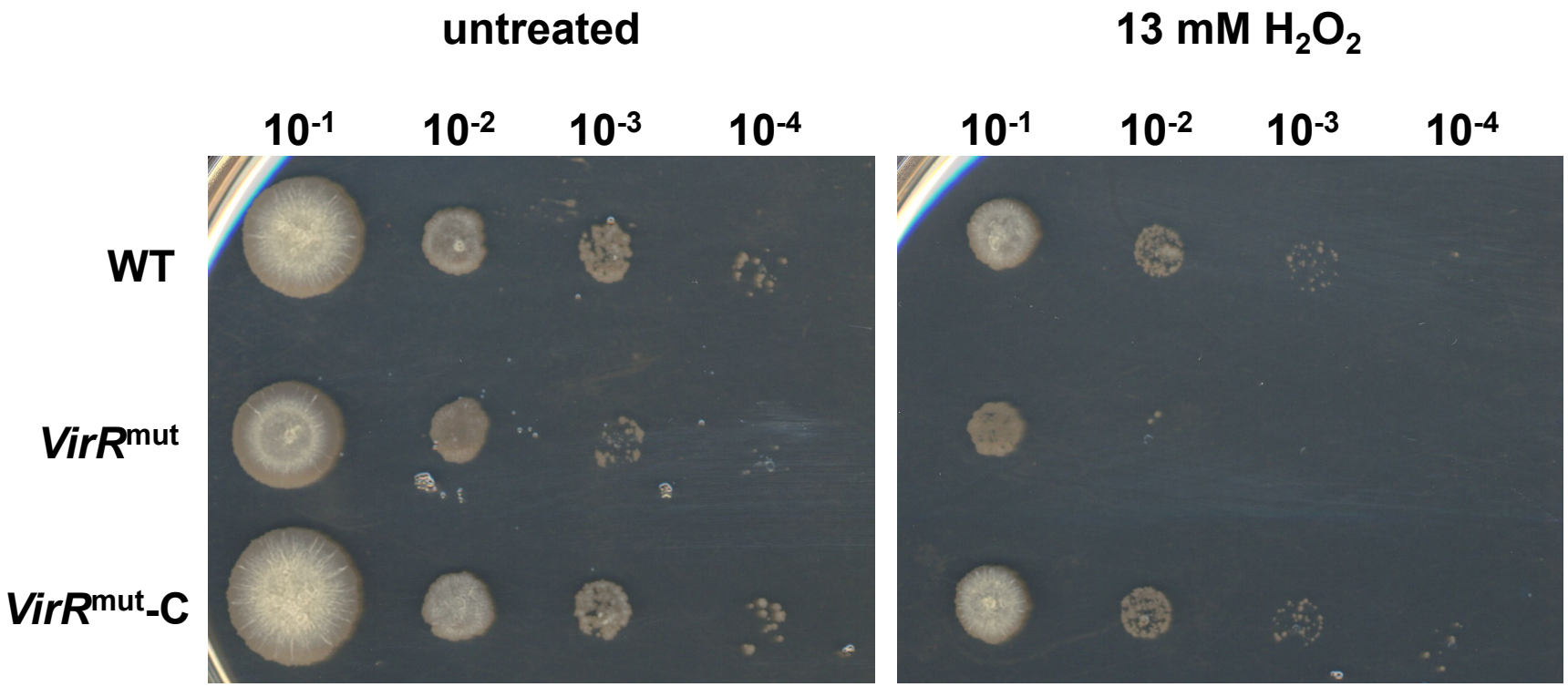
untreated
13 mM H_2O_2
10^{-1}
10^{-2}
10^{-3}
10^{-4}
10^{-1}
10^{-2}
10^{-3}
10^{-4}
WT
VirR^{mut}
VirR^{mut}-C

Fig S3

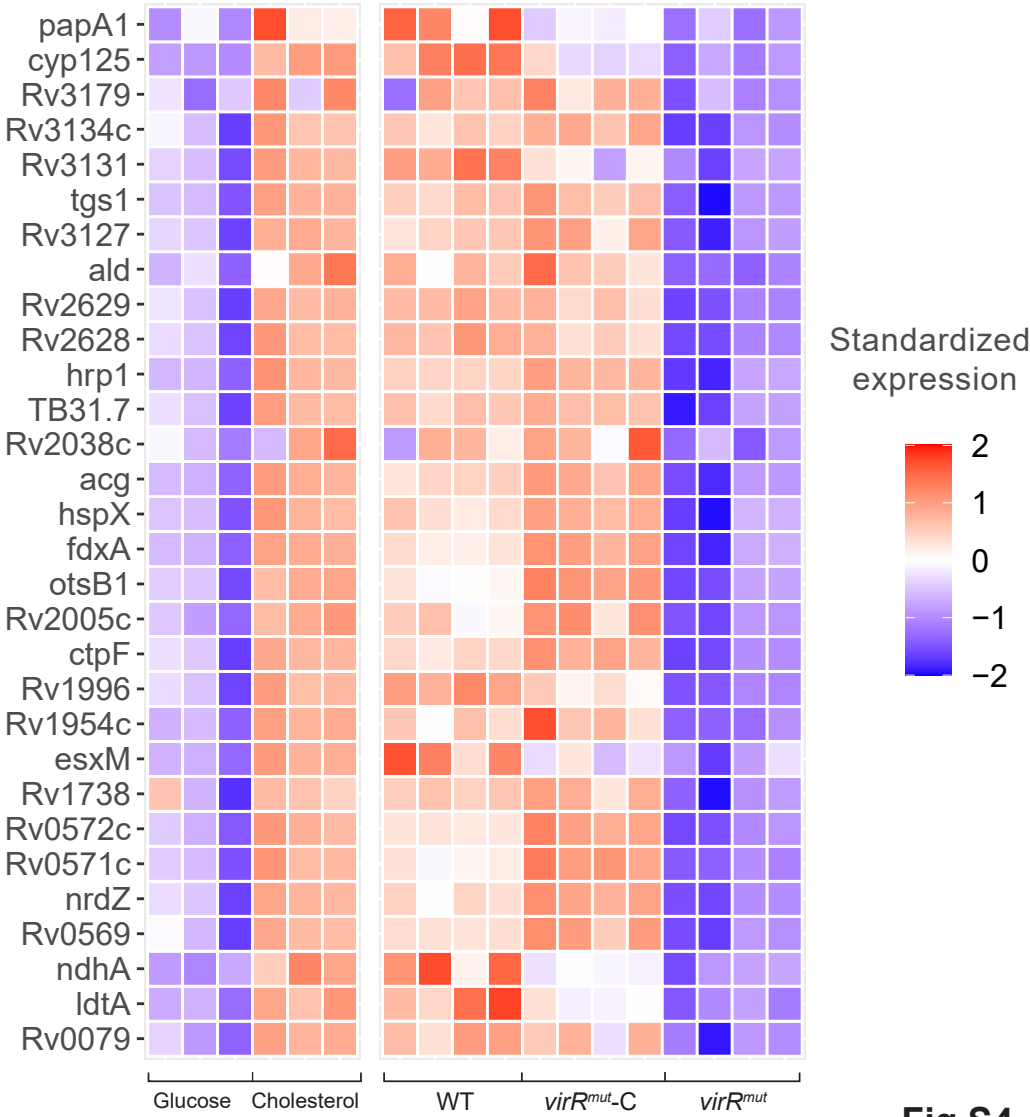
papA1
cyp125
Rv3179
Rv3134c
Rv3131
tgs1
Rv3127
ald
Rv2629
Rv2628
hrp1
TB31.7
Rv2038c
acg
hspX
fdxA
otsB1
Rv2005c
ctpF
Rv1996
Rv1954c
esxM
Rv1738
Rv0572c
Rv0571c
nrdZ
Rv0569
ndhA
ldtA
Rv0079
Glucose
Cholesterol
WT
virRmut-C
virRmut
Standardized expression
2
1
0
−1
−2

Fig S4

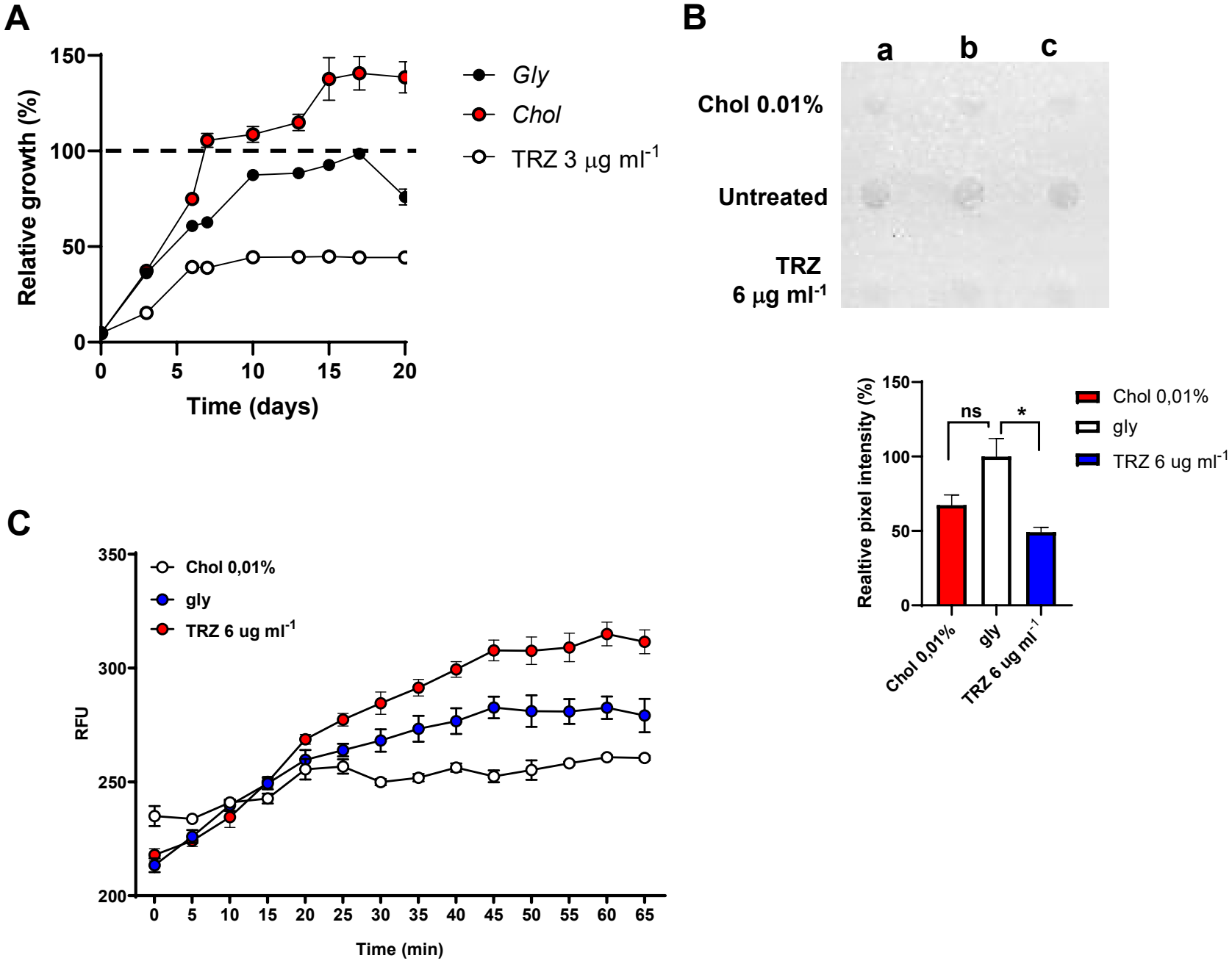
A
Relative growth (%)
150
100
50
0
0
5
10
15
20
Time (days)
Gly
Chol
TRZ 3 μg ml-1
B
a
b
c
Chol 0.01%
Untreated
TRZ
6 μg ml-1
Realtive pixel intensity (%)
150
100
50
0
ns
*
Chol 0,01%
gly
TRZ 6 ug ml-1
Chol 0,01%
gly
TRZ 6 ug ml-1
C
RFU
350
300
250
200
0
5
10
15
20
25
30
35
40
45
50
55
60
65
Time (min)
Chol 0,01%
gly
TRZ 6 ug ml-1

Fig S5

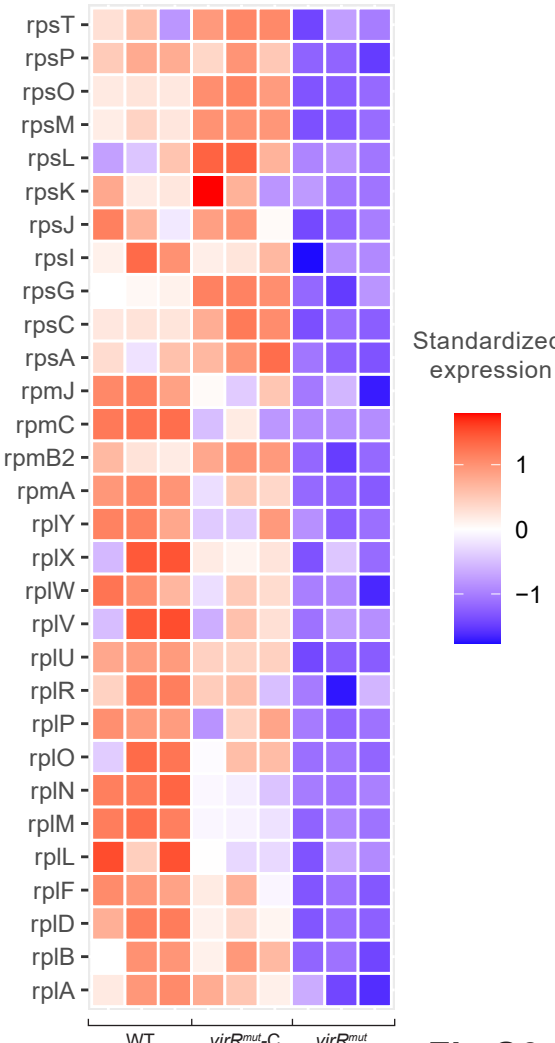
rpsT
rpsP
rpsO
rpsM
rpsL
rpsK
rpsJ
rpsI
rpsG
rpsC
rpsA
rpmJ
rpmC
rpmB2
rpmA
rplY
rplX
rplW
rplV
rplU
rplR
rplP
rplO
rplN
rplM
rplL
rplF
rplD
rplB
rplA
WT
virRmut-C
virRmut
Standardized expression
1
0
−1

Fig S6

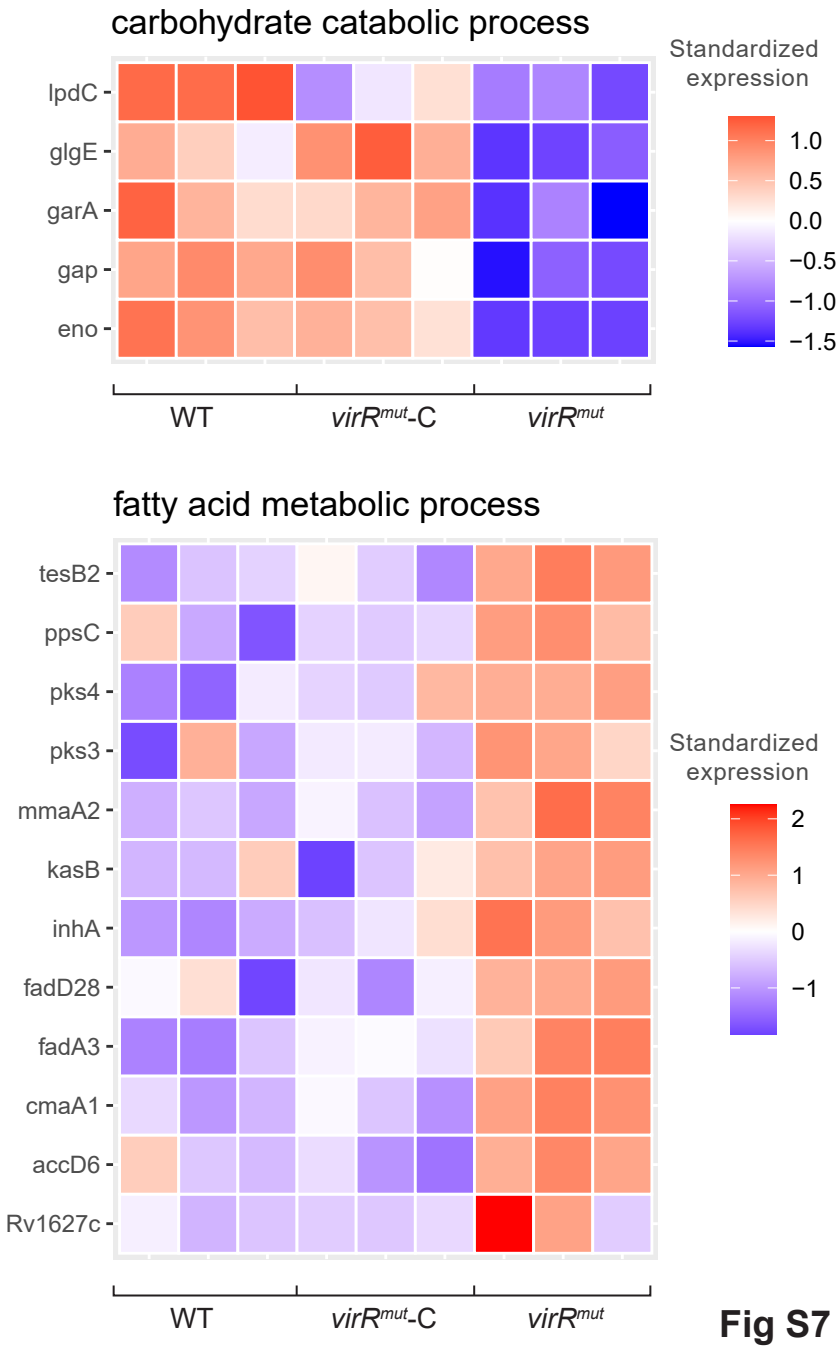
carbohydrate catabolic process
lpdC
glgE
garA
gap
eno
WT
virRmut-C
virRmut
Standardized expression
1.0
0.5
0.0
−0.5
−1.0
−1.5
fatty acid metabolic process
tesB2
ppsC
pks4
pks3
mmaA2
kasB
inhA
fadD28
fadA3
cmaA1
accD6
Rv1627c
WT
virRmut-C
virRmut
Standardized expression
2
1
0
−1

Fig S7

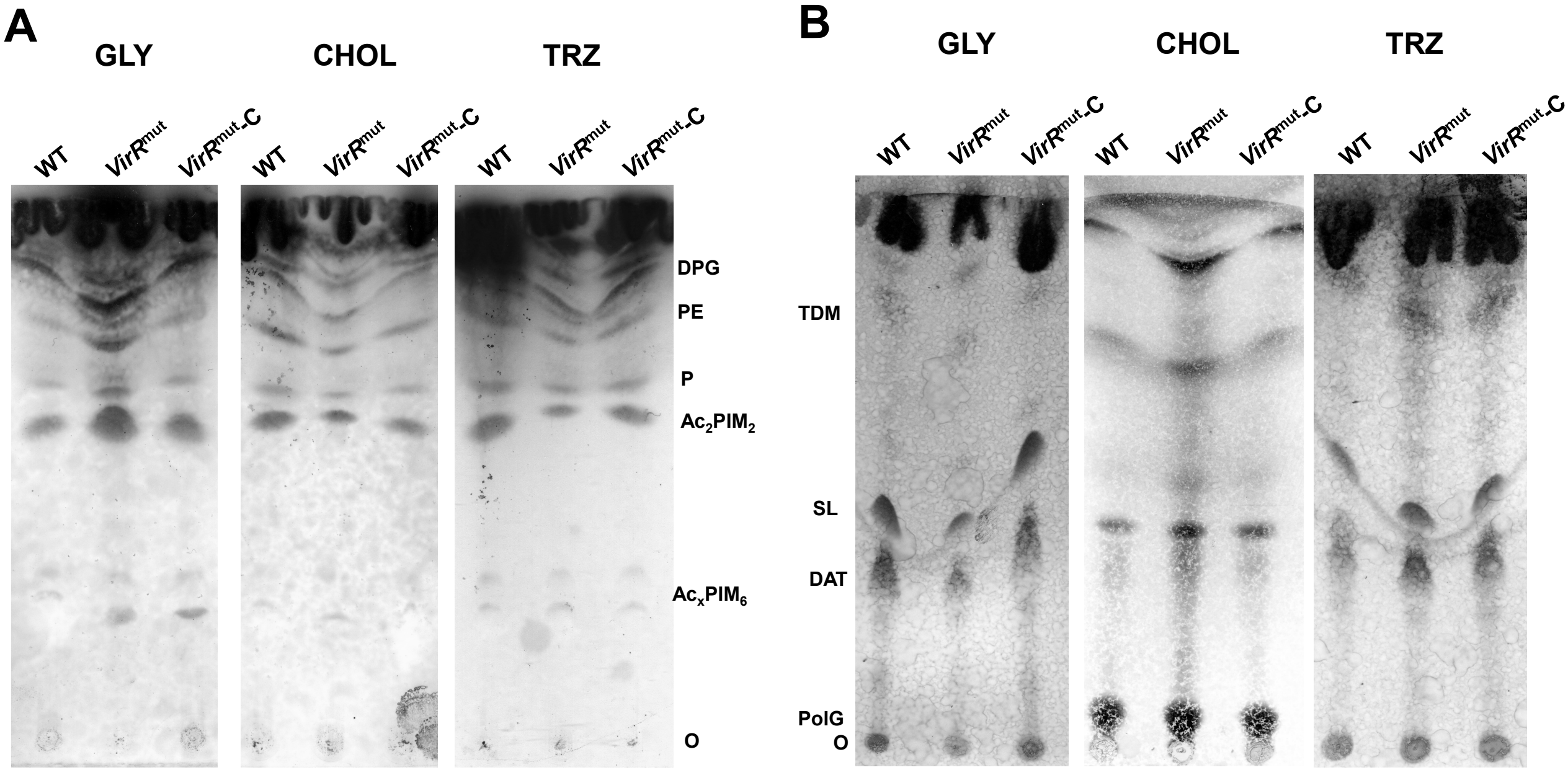
A
GLY
CHOL
TRZ
WT
VirRmut
VirRmut-C
DPG
PE
P
Ac2PIM2
AcxPIM6
O
B
GLY
CHOL
TRZ
WT
VirRmut
VirRmut-C
TDM
SL
DAT
PolG
O

FigS8

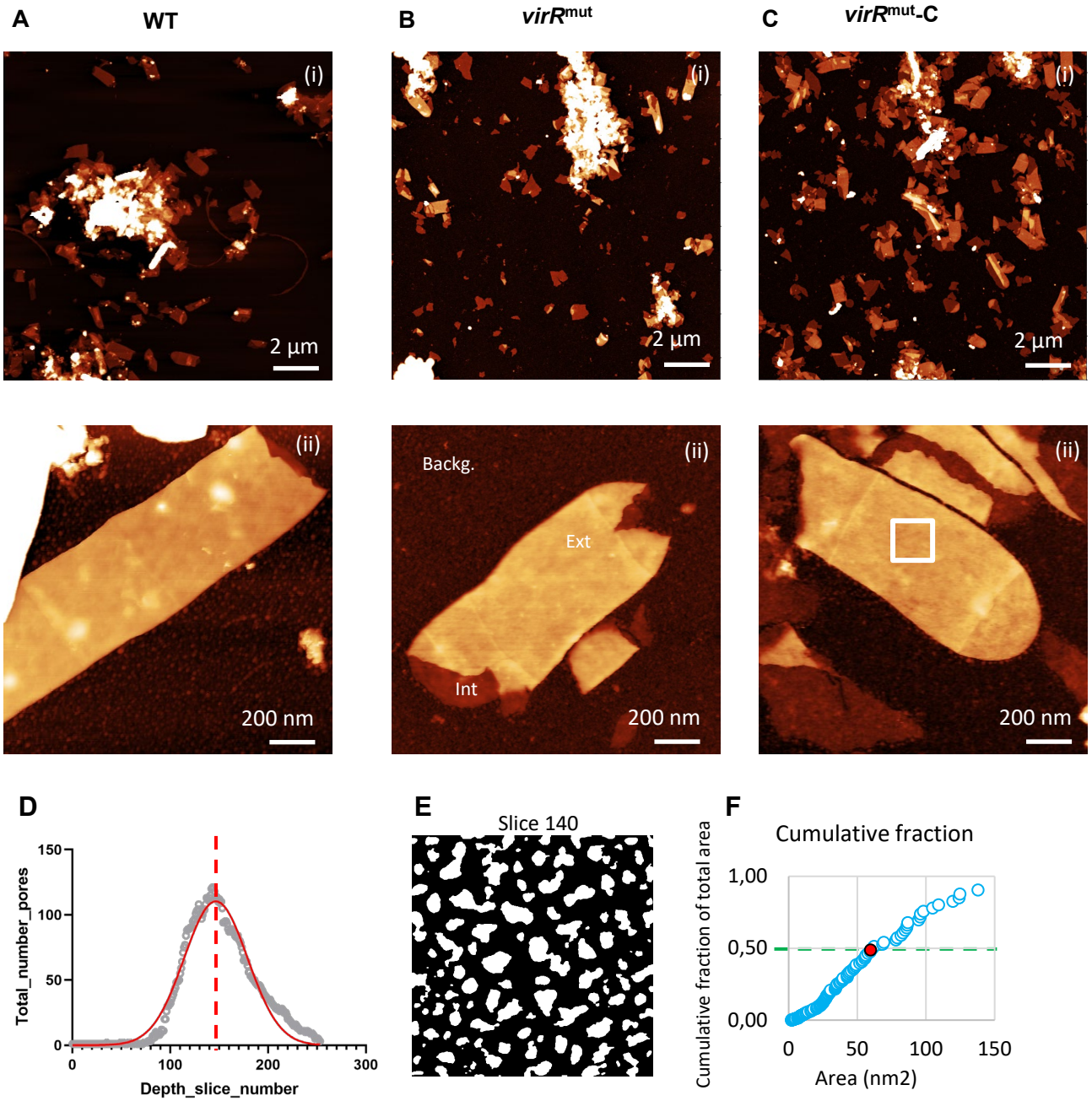
A
WT
B
virRmut
C
virRmut-C
(i)
2 µm
(ii)
200 nm
Backg.
Ext
Int
D
Total_number_pores
Depth_slice_number
E
Slice 140
F
Cumulative fraction
Cumulative fraction of total area
Area (nm2)

Fig S9

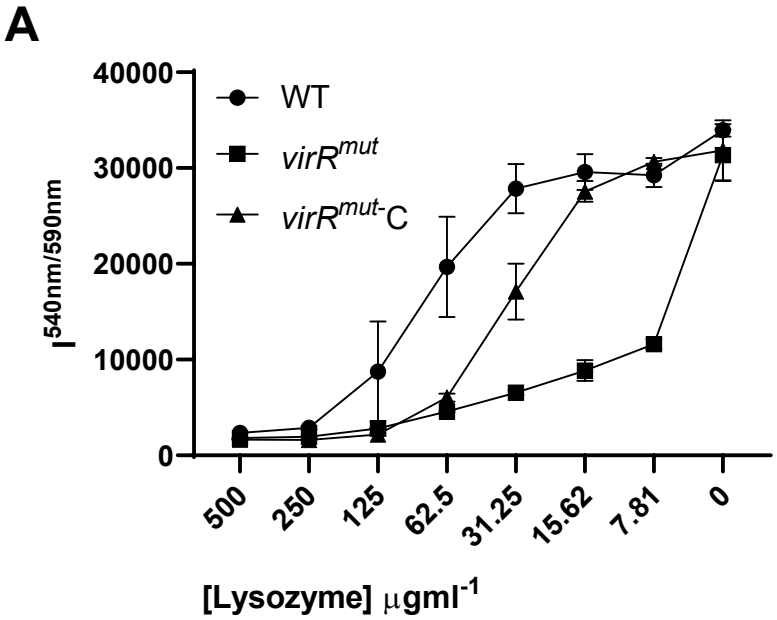
A
40000
30000
20000
10000
0
I540nm/590nm
WT
virRmut
virRmut-C
500
250
125
62.5
31.25
15.62
7.81
0
[Lysozyme] μgml-1

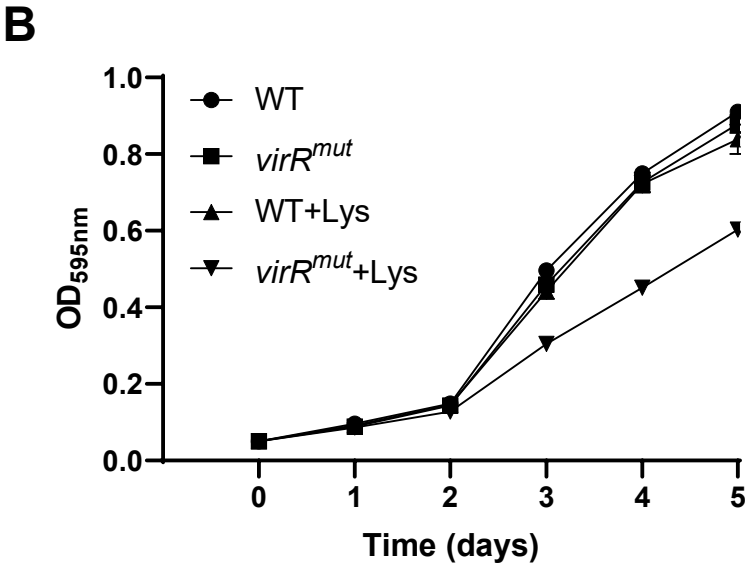
B
1.0
0.8
0.6
0.4
0.2
0.0
OD595nm
WT
virRmut
WT+Lys
virRmut+Lys
0
1
2
3
4
5
Time (days)

Fig S10

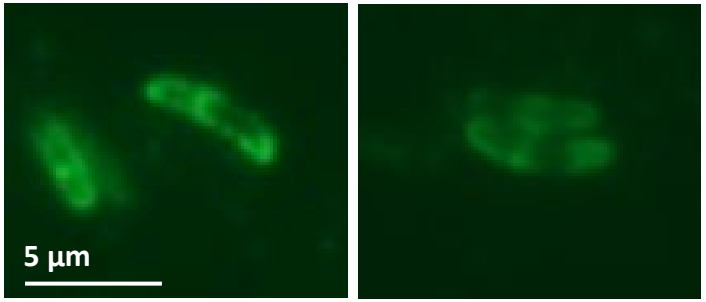

Fig S11

A

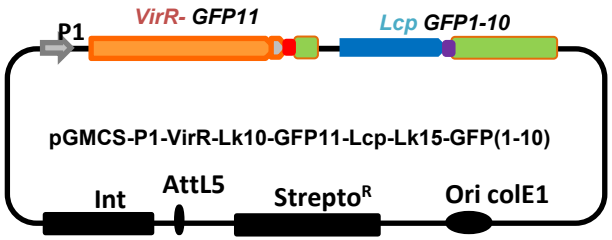
P1
VirR- GFP11
Lcp GFP1-10
pGMCS-P1-VirR-Lk10-GFP11-Lcp-Lk15-GFP(1-10)
Int
AttL5
Strepto^R
Ori colE1

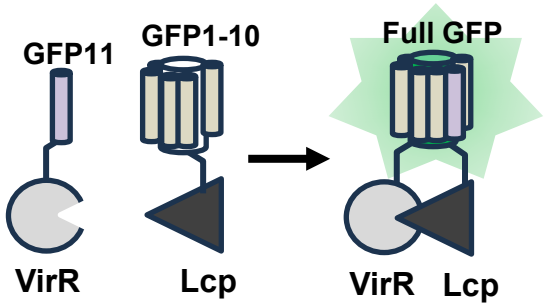
GFP11
GFP1-10
Full GFP
VirR
Lcp
VirR
Lcp

B

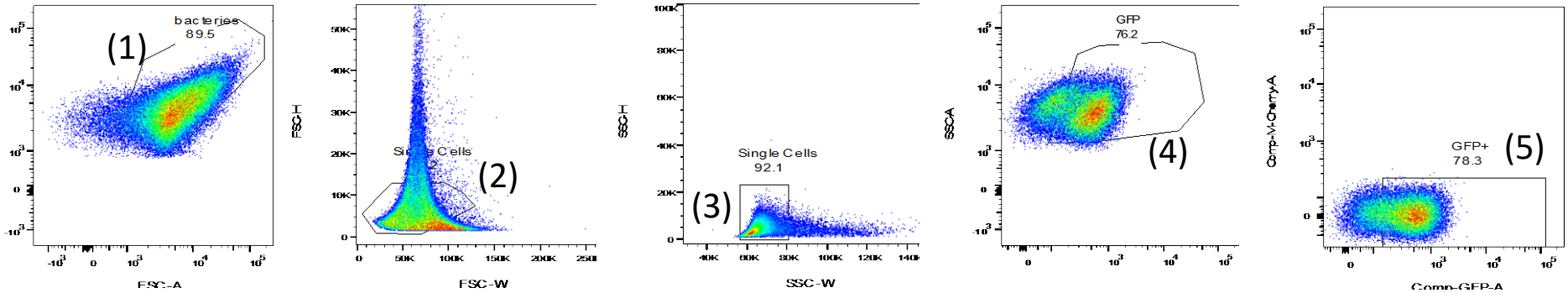
bacterias
89.5
(1)
FSC-A
FSC-H
Single Cells
(2)
FSC-W
SSC-H
Single Cells
92.1
(3)
SSC-W
SSC-A
GFP
76.2
(4)
Comp-V-CherryA
GFP+
78.3
(5)
Comp-GFP-A

Fig S12